



Technische Universität München
TUM School of Engineering and Design

Development of a Numerical Simulation Method for Large-scale Flame Propagation

Dario Živković

Vollständiger Abdruck der von der TUM School of Engineering and Design
der Technischen Universität München zur Erlangung eines
DOKTORS DER INGENIEURWISSENSCHAFTEN (DR.-ING.)
genehmigten Dissertation.

Vorsitz:

Prof. Rafael Macián-Juan, Ph.D.

Prüfer der Dissertation:

1. Prof. Dr.-Ing. Thomas Sattelmayer
2. Prof. Dr.-Ing. habil. Andreas Class

Die Dissertation wurde am 20.11.2023 bei der Technischen Universität München eingereicht
und durch die TUM School of Engineering and Design am 24.04.2024 angenommen.

Preface

The present work was funded by the German Federal Ministry for the Environment, Nature Conservation, Nuclear Safety and Consumer Protection (BMUV) on the basis of a decision by the German Bundestag, (project no. 1501573) which is gratefully acknowledged.

I express sincere gratitude to my Ph.D. advisor Prof. Dr.-Ing. Thomas Sattelmayer for scientifically supervising and supporting this work, all the while allowing me plenty of freedom in my research pursuits.

I extend my gratitude to Prof. Dr.-Ing. Andreas Class for accepting the important duty as a second examiner and Prof. Dr. Rafael Macián-Juan for chairing the examination board.

A big word of appreciation to all former colleagues and the staff of TUM Chair of Thermodynamics. Without the dedication you showed in your work, day in and day out, theses such as this one would never be possible. Special thanks goes to Mr. Utkarsh Pathak for his patient and detail-oriented proofreading, as well as the insightful suggestions, which have undoubtedly improved the text of this thesis.

I would like to thank Dr.-Ing. Stephan Kelm from FZ Jülich for friendly and inspiring collaboration. I learned a lot about the wider context of nuclear safety from it.

I thank my dear friend Dr.-Ing. Babak Gholami from BMW AG for motivating me to start my Ph.D. journey, as well as being an encouraging friend throughout it.

Lastly and most importantly, I thank my family for their unconditional love and support, especially my partner Mirela Radonjić for unlimited reserves of patience throughout these long years of my work at TUM and beyond.

Dario Živković

Munich, May 2024

Abstract

Potential for gas mixture explosions remains a critical safety concern in a number of technical fields. It is especially important for nuclear safety, where severe reactor accidents may produce flammable mixtures with the potential to compromise the reactor containment system. Given the practical difficulties of conducting experiments at the plant scale, numerical simulation methods that could enable detailed consequence analysis in a full-scale reactor containment have been in demand.

In the present work, a numerical method is designed with the aim of accurately representing the dynamics of the highly-transient process of flame propagation in whole – from ignition to possible detonation. This is achieved by adopting a density-based formulation of compressible Navier–Stokes equations with "all-speed" numerical fluxes and explicit time integration from the Strong Stability Preserving (SSP) Runge–Kutta family. The latter is shown well-suited for problems involving long intervals of simulated physical time, such as slow flame propagation in very large volumes.

Furthermore, a novel scale-adaptive Reynolds-averaged Navier–Stokes (RANS) model is derived, that introduces a sub-grid closure for the effects of the Darrieus–Landau instability. Said instability is relevant for flame acceleration in the early, quasi-laminar stages of gas explosions, where quiescent initial conditions are present. The model is validated with large-scale flame propagation experiments in corresponding conditions.

Lastly, a combined workflow for conducting reactor safety analysis is demonstrated by coupling the developed numerical method for flame propagation simulations with the prior results of gas mixing simulations with dedicated tools.

Kurzfassung

Die Gefahr von Gasgemischexplosionen ist ein kritisches Sicherheitsproblem in einer Reihe von technischen Bereichen. Besonders wichtig ist dies für die nukleare Sicherheit, wo bei schweren Reaktorunfällen entflammbare Gemische entstehen können, die das Reaktorsicherheitssystem gefährden können. Angesichts der praktischen Schwierigkeiten bei der Durchführung von Experimenten im Anlagenmaßstab sind numerische Simulationsmethoden gefragt, die eine detaillierte Analyse der Folgen in einem Reaktorsicherheitsbehälter ermöglichen.

In der vorliegenden Arbeit wird eine numerische Methode mit dem Ziel entwickelt, die Dynamik des hochtransienten Prozesses der Flammenausbreitung im Ganzen - von der Zündung bis zur möglichen Detonation - genau darzustellen. Dies wird durch die Annahme einer dichte-basierten Formulierung der kompressiblen Navier–Stokes-Gleichungen mit "all-speed" numerischen Flüssen und expliziter Zeitintegration aus der "Strong Stability Preserving" (SSP) Runge–Kutta-Familie erreicht. Letztere eignet sich gut für Probleme mit langen Intervallen simulierter physikalischer Zeit, wie z.B. langsame Flammenausbreitung in sehr großen Räumen.

Darüber hinaus wird ein neuartiges skalenadaptives RANS-Modell abgeleitet, das ein Feinstrukturmodell für die Auswirkungen der Darrieus-Landau-Instabilität einführt. Diese Instabilität ist für die Flammenbeschleunigung in den frühen, quasi-laminaren Stadien von Gasexplosionen relevant, in denen ruhende Anfangsbedingungen vorliegen. Das Modell wird mit großskaligen Flammenausbreitungsexperimenten unter entsprechenden Bedingungen validiert.

Schließlich wird ein kombinierter Arbeitsablauf für die Durchführung von Reaktorsicherheitsanalysen demonstriert, indem die entwickelte numerische Methode für Flammenausbreitungssimulationen mit den vorherigen Ergebnissen von Gasmischungssimulationen mit speziellen Tools gekoppelt wird.

Contents

Preface	iii
Abstract	iv
Contents	vi
List of Figures	x
List of Tables	xv
Nomenclature	xvii
Acronyms	xvii
Symbols	xx
Dimensionless numbers	xxi
Greek symbols	xxii
Superscripts	xxiii
Subscripts	xxiii
Chemical symbols	xxiv
1 Introduction	1
1.1 Motivation for combustion research in nuclear safety	1
1.2 Role of CFD in large-scale gas explosion modeling	3
1.2.1 Challenges	3
1.2.2 State of the art	5
1.2.3 Objectives of the present work	10
1.3 Outline of the thesis	11

I	Numerical Method for Large-scale Combustion Phenomena	12
2	Compressible reacting flow	13
2.1	Governing equations	13
2.2	Combustion modeling	17
2.2.1	Reaction rate closure	19
2.3	Turbulence modeling	20
2.3.1	SST model	21
2.3.2	SAS model	25
2.4	All-speed convective fluxes	27
2.4.1	Validation: plane-parallel Poiseuille flow	31
2.5	Efficient time integration	32
2.5.1	Validation: Sod shock tube	34
3	Validation in the deflagration regime	37
3.1	Turbulent flame propagation in a spherical vessel	37
3.2	Computational model and setup	38
3.3	Turbulent flame speed correlation	41
3.4	Pressure results	41
3.5	Flame position and speed results	44
3.6	Time integration performance comparison	47
II	Deflagration Modeling in Conditions of Low Turbulence	51
4	Introduction to the Darrieus–Landau instability	52
4.1	Outline and motivation	52
4.2	State of the art in Darrieus–Landau instability modeling	53
5	Model derivation	57
5.1	Scale-adaptive, fractal-based model for Darrieus–Landau instability effects	57
5.2	Small-scale effects on effective flame wrinkling	61
5.3	Total effective flame wrinkling	64
5.4	Model assumptions and validity limits	64

6 Model validation	71
6.1 Computational setup	71
6.2 Large-scale hemispherical near-stoichiometric hydrogen flame	72
6.3 Lean spherical hydrogen flames	80
6.4 Lean hydrogen flames in the THAI facility	82
7 Concluding remarks	91
III Application to Generic Containment Accident Analysis	92
8 Introduction to combustion CFD for reactor accident analysis	93
8.1 Full-scale containment combustion simulations	93
8.2 Motivation and objectives of the present work	96
9 Numerical simulation of combustion in the generic containment	100
9.1 "Generic Containment" definition	100
9.2 The analyzed accident scenario	102
9.3 Computational domain and grid	103
9.4 Initial conditions and ignition	105
9.4.1 Mixture formation phase	105
9.4.2 Ignition location	110
9.5 Computational setup	110
9.6 Results	112
9.6.1 Early phase ($t < 1.3$ s)	112
9.6.2 Late phase ($t > 1.3$ s)	120
10 Concluding remarks	124
IV Conclusion	126
11 Summary	127
12 Outlook	130
Bibliography	133

CONTENTS

Appendix	153
A Publications	153

List of Figures

1.1	Conceptual overview of nuclear reactor accident stages.	2
1.2	Schematic diagrams of the two European Pressurized Water Reactor (PWR) reactor types, the European Pressurized Reactor (EPR) and Konvoi. The reactor containment is contoured with a blue line.	4
2.1	Schematic depiction of wrinkled (A_{eff}) and smooth (A_1) flame surfaces.	19
2.2	Results of plane-parallel Poiseuille flow at $\text{Ma} = 0.05$	31
2.3	Sod (1978) shock tube case; 1D grid: 100 cells along the tube ($\Delta_x = 100$ mm).	36
3.1	A view of the two computational domains and grids used for simulations. In Domain A cell sizes range from 6 to 16 mm, with the central area consisting of uniformly spaced 12 mm cells. Domain B is uniformly discretized by 5 mm cells.	40
3.2	Pressure rise in the spherical vessel for $x_{\text{H}_2} = 16\%$	42
3.3	Pressure rise in the spherical vessel for $x_{\text{H}_2} = 20\%$	42
3.4	Pressure rise in the spherical vessel for $x_{\text{H}_2} = 28\%$	43
3.5	Pressure rise in the spherical vessel for $x_{\text{H}_2} = 16\%$ and $u'_i = 2.1$ m/s computed on a 7 mm and a 12 mm structured hexahedral grid.	43
3.6	Evolution of flame radius r over time in the spherical vessel validation case. The results are computed using Domain B.	45
3.7	Flame displacement speed over the radius r in the spherical vessel validation case. The results are computed using Domain B.	46

3.8	Pressure rise at $x_{\text{H}_2} = 28\%$ and high level of turbulence ($u'_i = 2.1$ m/s) computed using different time integration methods (Domain A). CPU time comparison is given in Table 3.3.	48
3.9	Results of turbulent flame speed at $x_{\text{H}_2} = 16\%$ and high level of turbulence ($u'_i = 2.1$ m/s) for different time integration methods. Each method is run at the maximum allowable Courant–Friedrich–Lewy (CFL) _{max} needed to achieve comparable level of accuracy. CPU time comparison is given in Table 3.4.	49
4.1	A schematic diagram of the Darrieus–Landau (DL) instability at the flame front. Orange arrows show the direction of cusp movement.	53
4.2	A planar, Darrieus–Landau (DL)-instability-perturbed flame can be understood as a vortex sheet forming due to differences in velocity components in the y direction (Matalon, 2018). The detail shows the velocity diagram at the flame front, corresponding to the location of the discontinuity in the streamline shape.	54
5.1	Fractal growth of the area of a self-similar surface. In an interval between an inner (ϵ_i) and an outer (ϵ_o) cut-off scale, the growth of surface area is described by a constant slope $2 - D_3$	58
5.2	Lean hydrogen–air flames are characterized by a negative Markstein length \mathcal{L}	63
5.3	Lean hydrogen–air flames are characterized by low critical radii for the onset of cellular instabilities. ($R_{\text{crit}} \approx 10\text{--}50$ mm)	65
5.4	Qualitative depiction of the flame instability limits derived from the linear stability theory (Lieberman, 2021; Matalon, 2018).	69
5.5	DL instability region in the Borghi diagram lies for $\text{Le} \geq 1$ below the red line (Chaudhuri et al., 2011) (large scales and low turbulence intensities). Chomiak and Lipatnikov (2023) (blue line) suggest the area of instability effect (Thermal–diffusive (TD) and DL) to be below $\text{Ka} \approx \text{O}(10)$	70
6.1	Computational setup for the hemispherical flame propagation, near-stoichiometric H_2 –air mixture ($x_{\text{H}_2} = 29.7\%$).	73

6.2	Details of the computational grid used for the large scale hemispherical flame propagation.	74
6.3	Results for the hemispherical H ₂ -air flame with $x_{\text{H}_2} = 29.7\%$. . .	75
6.4	Comparison of results calculated on the base grid (Δ_x) and a refined grid ($\Delta_x/2$).	77
6.5	Flame shape comparison for hemispherical flame propagation and the near-stoichiometric H ₂ -air mixture ($x_{\text{H}_2} = 29.7\%$). The image shows flame position isochrones.	78
6.6	A wrinkling factor Ξ field on the isosurface of reaction regress variable $b \approx 0.5$ at $t = 0.3$ s.	79
6.7	A temperature field on the isosurface of reaction regress variable $b \approx 0.5$ at $t = 0.3$ s.	79
6.8	Spherical flame propagation for lean hydrogen-air mixtures. Experimental data from Bauwens et al. (2017).	81
6.9	Computational domain representing the Thermal Hydraulics, Hydrogen, Aerosols and Iodine (THAI) vessel and a cut through the unstructured polyhedral grid.	84
6.10	Upward hydrogen deflagration in the THAI vessel, cases HD12 & HD2R ($x_{\text{H}_2} = 8\%$, Tab. 6.3)	85
6.11	Pressure rise for the THAI hydrogen deflagration case HD12 ($x_{\text{H}_2} = 8\%$).	86
6.12	Flame shape comparison for the upward hydrogen deflagration in the THAI vessel, case HD12 ($x_{\text{H}_2} = 8\%$).	87
6.13	Isosurfaces of the flame front in the THAI vessel, defined as reaction regress variable $b \approx 0.5$ show an elongated flame shape.	89
6.14	A cut through the flame surface is shown by the $b \approx 0.5$ isoline (orange). Streamlines (black) show a recirculation zone near the THAI vessel wall where fresh gas is pushed downward.	90
8.1	A simplified schematic diagram of the Konvoi-type reactor containment.	97
9.1	Schematic diagram of containment sections (zones) relevant to the present work: Dome, SG left & right, Sump and RR.	101

LIST OF FIGURES

9.2	A Three-dimensional (3D) view of the unstructured polyhedral computational grid.	103
9.3	Cut-plane view of the unstructured polyhedral computational grid.	104
9.4	Schematic diagram of the reactor accident analysis chain used in the present work. In the mixture formation phase, the Lumped Parameter (LP) code used is Containment Code System (CO-COSYS), results of which were mapped to a Computational Fluid Dynamics (CFD) solver <i>containmentFoam</i> . The combustion CFD was performed using <i>explosionDynamicsFoam</i> , derived in Part I and Part II of the present work.	106
9.5	Gas composition in % vol. at $t = 47$ h of the accident.	107
9.6	Cut-view of the mixture composition and thermodynamic state initial conditions for flame propagation analysis of the Generic Containment case.	108
9.7	Cut-view of the velocity and turbulence initial conditions for flame propagation analysis of the Generic Containment case.	109
9.8	Schematic diagram of the Konvoi-type reactor containment showing convective loops in different accident scenarios: a single loop in case of Small Break (SB)–Loss of Coolant Accident (LOCA) or Station Black-out (SBO) and two loops in case of Medium Break (MB)- or Large Break (LB)-LOCA.	109
9.9	Computational domain for the Generic Containment simulations included the entire volume of the simplified containment geometry. Figure shows a Two-dimensional (2D) and an isometric view of ignition location and pressure probes.	111
9.10	Pressure rise results in the containment during the flame propagation. Pressure probe locations are defined in Table 9.3.	113

9.11 2D cut planes showing the time evolution of the flame position represented by the reaction regress variable (b) fields for the <i>early phase</i> of flame propagation ($t < 1.3$ s). The isoline where $b \approx 0.5$ is highlighted in bright orange. The cut planes pass between steam generators and cut through the centerline of the two ducts connecting the Reactor Room (RR) and Steam Generator (SG) sections.	114
9.12 Gas jet from the reactor room (RR), right after the peak pressure is reached in that compartment. The flame is elongated by the strong advection. Additionally, turbulence generation is shown by the k field.	115
9.13 Pressure field p on the location of gas jet impingement on the wall behind the steam generators shows a moderate overpressure on the impacted side of approx. 2000 Pa.	117
9.14 Time evolution of the flame position represented by the isosurface of the flame regress variable $b \approx 0.5$. The field Ξ shows the flame wrinkling factor.	119
9.15 Overall combustion progress tracked as total combusted volume in the domain.	120
9.16 Time evolution of the b fields for the <i>late phase</i> of flame propagation ($t > 1.3$ s). The $b \approx 0.5$ isoline is highlighted in bright orange. The cut planes pass between steam generators and cut through the centerline of the two ducts connecting the RR and SG sections.	121
9.17 Time evolution of the flame position represented by the isosurface of the flame regress variable $b \approx 0.5$. The field Ξ shows the flame wrinkling factor.	123

List of Tables

2.1	Shear Stress Stransport (SST) model coefficients.	25
2.2	Scale Adaptive Simulation (SAS) model coefficients.	26
2.3	Initial left and right states of the Sod shock tube.	35
2.4	Performance comparison of time integration methods for the Sod shock tube case.	36
3.1	Turbulence intensity levels in the spherical vessel.	38
3.2	Properties of the investigated hydrogen–air mixtures: unstretched laminar flame speed S_1 , laminar flame thickness δ_1 and Lewis number Le	39
3.3	Time integration performance for pressure rise simulations (Domain A).	48
3.4	Time integration performance for flame propagation simulations (Domain B).	49
6.1	Characteristic properties of the near-stoichiometric H_2 –air case: volumetric hydrogen concentration x_{H_2} , equivalence ratio Φ , initial temperature T_0 , initial pressure p_0 , unstretched laminar flame speed $S_{1,0}$, laminar flame thickness δ_1 , effective Lewis number Le_{eff} , Markstein length \mathcal{L}	72
6.2	Properties of spherical lean H_2 –air cases. Volumetric hydrogen concentration x_{H_2} , equivalence ratio Φ , initial temperature T_0 , initial pressure p_0 , unstretched laminar flame speed $S_{1,0}$, laminar flame thickness δ_1 , effective Lewis number Le_{eff} , Markstein length \mathcal{L}	80

6.3	Mixture characteristics for the THAI validation case. Volumetric hydrogen concentration x_{H_2} , equivalence ratio Φ , initial temperature T_0 , initial pressure p_0 , unstretched laminar flame speed $S_{\text{l},0}$, laminar flame thickness δ_{l} , effective Lewis number Le_{eff} , Markstein length \mathcal{L}	83
9.1	Breakdown of the SB-LOCA accident sequence prior to ignition.	102
9.2	Gas composition table at $t = 47$ h of the accident.	105
9.3	Coordinates of the ignition location and pressure probes (Figure 9.9).	110

Nomenclature

Acronyms

1D	One-dimensional
2D	Two-dimensional
3D	Three-dimensional
AUSM	Advection Upwind Splitting Method
BWR	Boiling Water Reactor
CFD	Computational Fluid Dynamics
CFL	Courant–Friedrich–Lewy
CJ	Chapman–Jouguet
COCOSYS	Containment Code System
DDT	Deflagration-to-detonation Transition
DL	Darrieus–Landau
DNS	Direct Numerical Simulation
DOM	Discrete Ordinate Method
EBU	Eddy Break-up
EPR	European Pressurized Reactor
FA	Flame Acceleration
FDS	Flux Difference Splitting

FLACS	Flame Acceleration Simulator
FVM	Finite Volume Method
FVS	Flux Vector Splitting
GRS	Gesellschaft für Anlagen- und Reaktorsicherheit gGmbH
JRC	Joint Research Centre
LB	Large Break
LES	Large Eddy Simulation
LOCA	Loss of Coolant Accident
LP	Lumped Parameter
MAAP	Modular Accident Analysis Program
MB	Medium Break
MCCI	Molten Corium Concrete Interaction
MUSCL	Monotonic Upstream-centered Scheme for Conservation Laws
NS	Navier–Stokes
ODE	Ordinary Differential Equation
OpenFOAM	Open Field Operation and Manipulation
PAR	Passive Autocatalytic Recombiner
PaSR	Partially Stirred Reactor
PDE	Partial Differential Equation
PIV	Particle Image Velocimetry
PWR	Pressurized Water Reactor
RANS	Reynolds-averaged Navier–Stokes
RK	Runge–Kutta
RPV	Reactor Pressure Vessel

Acronyms

RR	Reactor Room
SAS	Scale Adaptive Simulation
SB	Small Break
SBO	Station Black-out
SG	Steam Generator
SGS	Subgrid-scale
SMART	Sharp and Monotonic Algorithm for Realistic Transport
SSP	Strong Stability Preserving
SST	Shear Stress Stransport
TD	Thermal–difussive
THAI	Thermal Hydraulics, Hydrogen, Aerosols and Iodine
TUM	Technical University Munich
TVD	Total Variation Diminishing
URANS	Unsteady Reynolds-averaged Navier–Stokes

Symbols

Symbol	Unit	Description
A	m^2	surface area
C_p	$\text{kJ}/(\text{kgK})$	specific isobaric heat capacity
C_v	$\text{kJ}/(\text{kgK})$	specific isochoric heat capacity
D_3	m	fractal dimension of a 3D surface
E	m^2/s^2	specific total energy $E = e + \frac{u_i^2}{2}$
$L_{\text{vK},f}$	m	flame von Kármán length scale
L	m	length scale
R	$\text{J}/(\text{kgK})$	specific gas constant
S_l	m/s	laminar flame speed
T	K	temperature
\dot{m}	kg/s	mass flux
\mathcal{L}	m	Markstein length
a	m^2/s	thermal diffusivity
b	-	reaction regress variable
c	m/s	speed of sound
d	m	diameter
e	m^2/s^2	specific internal energy
f_i	m/s	velocity vector in flame normal direction n_i
g_i	m/s	gravitational acceleration in direction x_i
h_c	m^2/s^2	specific chemical enthalpy
h_f	m^2/s^2	specific heat of formation
h_s	m^2/s^2	specific sensible enthalpy
h	m^2/s^2	specific enthalpy
k	m^2/s^2	specific turbulent kinetic energy
m	-	SSP Runge–Kutta scheme parameter (number of stages)

Dimensionless numbers

Symbol	Unit	Description
---------------	-------------	--------------------

n_i	-	unit normal vector
p	Pa	pressure
r	m	radius
t	s	time
u'_i	m/s	velocity fluctuation (Reynolds decomposition)
u''_i	m/s	velocity fluctuation (Favre decomposition)
u_i	m/s	velocity vector in direction x_i
x	-	volume fraction

Dimensionless numbers

Symbol	Description
---------------	--------------------

Da	Damköhler number
Ka	Karlovitz number
Le	Lewis number
Ma	Mach number
Pr	Prandtl number
Re	Reynolds number
Sc	Schmidt number
Ze	Zeldovich number

Greek symbols

Symbol	Unit	Description
Δ_x	m	cell size
Γ	m^2/s	passive scalar diffusivity
Φ	-	equivalence ratio
Ξ	-	flame wrinkling factor
α	-	growth exponent
β	-	fractal excess
δ_l	m	laminar flame thickness
δ_{ij}	-	Kronecker delta
$\dot{\Omega}$	$\text{kg}/(\text{m}^3 \text{s})$	volumetric consumption rate of the unburned mixture
ϵ_i	m	inner cut-off scale
ϵ_o	m	outer cut-off scale
ϵ	-	emissivity
γ	-	expansion ratio
κ_c	1/m	curvature
κ_{vK}	-	von Kármán constant
κ	-	heat capacity ratio C_p/C_v (isentropic expansion factor)
λ	$\text{W}/(\text{Km})$	thermal conductivity
μ	$\text{kg}/(\text{ms})$	dynamic viscosity
ν	m^2/s	kinematic viscosity
ω	1/s	turbulence eddy frequency
ρ	kg/m^3	density
σ_{ij}	N/m^2	viscous stress tensor
τ_{ij}	N/m^2	turbulent stress tensor

Superscripts

Symbol	Description
--------	-------------

$*$ $''$	fluctuation (Favre decomposition)
$*$ $'$	fluctuation (Reynolds decomposition)
$*$ l	l^{th} species
$*$ n	n^{th} time step or iteration
$*$	time derivative
$\overline{}$	Reynolds average
$\tilde{}$	Favre average

Subscripts

Symbol	Description
--------	-------------

0	initial
DL	Darrieus–Landau
D	Deficient species
E	Excessive species
L	left
R	right
TD	thermal–diffusive
aicc	adiabatic isochoric complete combustion
a	adiabatic
b	burned
eff	effective
i	inner cut-off scale

Symbol Description

lim	limit
l	laminar
o	outer cut-off scale
ref	reference
t	turbulent
u	unburned

Chemical symbols**Symbol Description**

CO ₂	Carbon dioxide
CO	Carbon monoxide
H ₂ O	Water
H ₂	Hydrogen
N ₂	Nitrogen
O ₂	Oxygen

1 Introduction

1.1 Motivation for combustion research in nuclear safety

Analysis of combustion phenomena plays an important role in safety considerations of nuclear power plants. In severe reactor accidents such as Station Black-out (SBO) or Loss of Coolant Accident (LOCA), a large quantity of hydrogen can be produced as a result of a reaction between steam and zirconium fuel-rod cladding. Furthermore, carbon monoxide can be released as well in case of a Molten Corium Concrete Interaction (MCCI). Release of these gases into the reactor containment and mixing with the available air can lead to formation of flammable gas mixtures with a high probability of ignition due to a wide flammability limit of hydrogen and availability of ignition sources such as hot surfaces or particles. Pressure loads resulting from combustion of such gas clouds have already been proven sufficient to cause severe damage to the reactor safety systems or, in some cases, the structural integrity of the containment itself. In the latter case, the damage would lead to radioactive material escaping into the environment. Figure 1.1 shows a conceptual overview of different stages in the reactor accident event chain.

Overall risk of gas explosions as a result of a severe nuclear reactor accident remains a concern for the existing and future water-cooled reactors. Such accidents involve numerous stages and can last for multiple days. During that time, combustion risk varies locally depending on the dynamics of flammable gas production, steam inertization, thermodynamic state, installed safety measures, internal structural damage, etc. (Bentaïb et al., 2015).

Risk of fast flames leading to Deflagration-to-detonation Transition (DDT) is mainly a concern for the early "in-vessel" phase of a reactor accident, when rapid hydrogen production results in locally high concentrations of that gas,

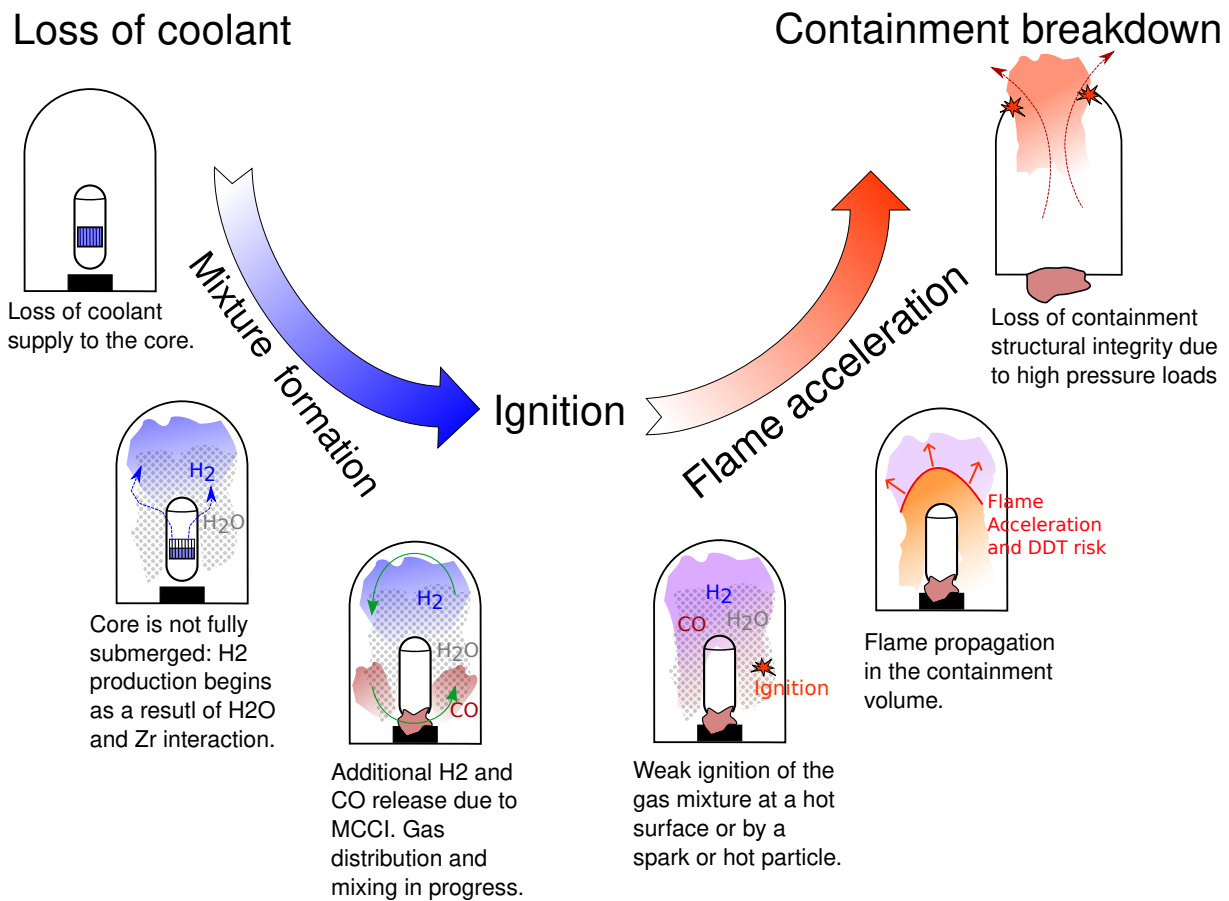


Figure 1.1: Conceptual overview of nuclear reactor accident stages.

while steam concentration is still too low (Fischer et al., 2014). At that stage, the key for safety is avoiding the possibility of flame acceleration, since a transition to detonation (DDT) would lead to severe consequences due to damage caused by extreme pressure loads. Slow flames are a safety concern as well, since they can lead to locally high temperature loads on various safety systems and structures, while also leading to a gradual build-up of pressure in the closed volume of the reactor containment. Such quasi-static pressure loads may compromise the containment integrity as well, especially since they may persist for long periods of time in a closed vessel such as the reactor containment that has an unfavorable surface-to-volume ratio for cooling because of its massive size (Gupta and Langer, 2019).

Given that geometric scale and internal complexity of a reactor containment make experimental investigation largely unfeasible, numerical methods have

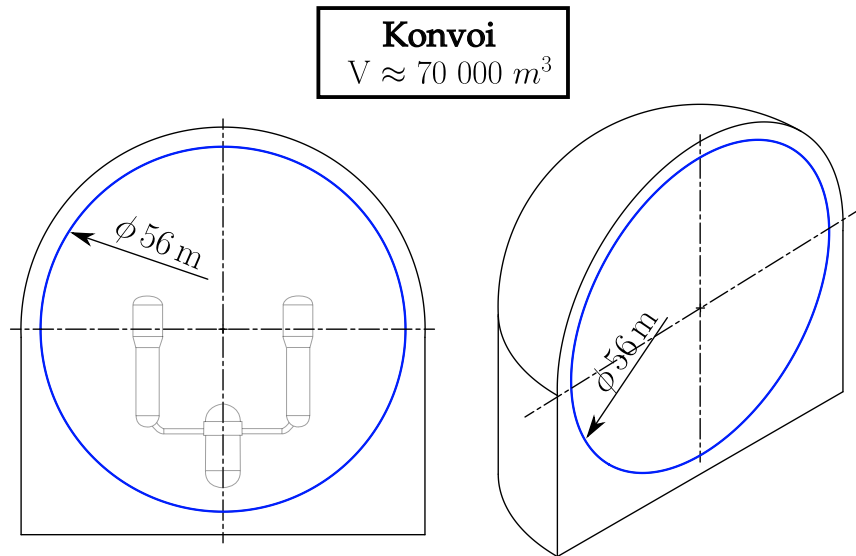
been in strong demand in the nuclear safety domain. For illustration, Figure 1.2 shows a schematic diagram of internal volumes of two Pressurized Water Reactor (PWR) containments: European Pressurized Reactor (EPR) and Konvoi. Development of numerical methods that would enable efficient analysis of safety-critical scenarios, which would otherwise be unattainable, is the goal of ongoing work in the field (Fiorina et al., 2022).

1.2 Role of CFD in large-scale gas explosion modeling

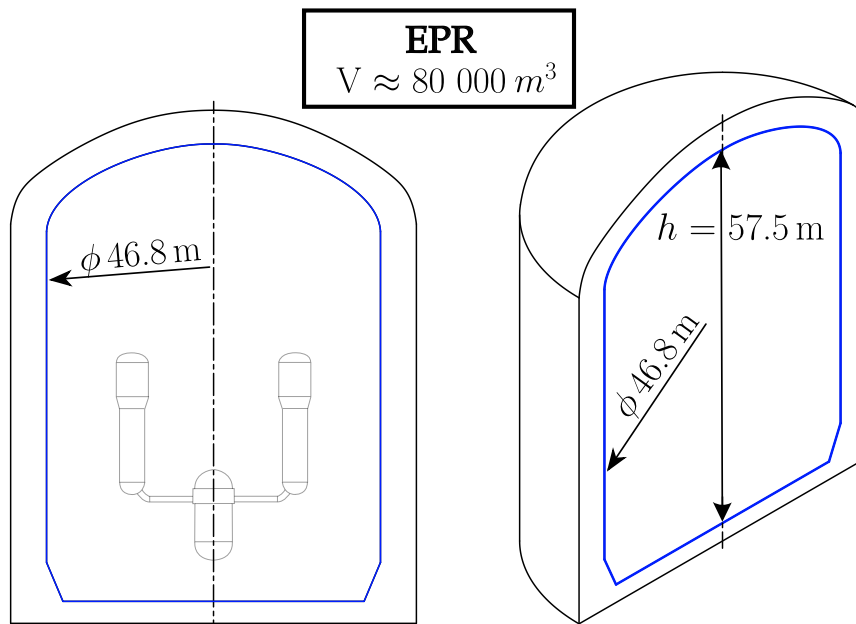
1.2.1 Challenges

There is a large number of physical and chemical processes involved in thermal hydraulic and flame propagation phenomena inside a reactor containment undergoing a severe accident. Turbulence, convective heat transfer, buoyancy, thermal radiation, multiphase flow (water spray) and steam condensation can all interact with the inherently complex phenomenon of combustion. In analysis of nuclear safety, combustion involves chemistry with mixtures of two flammable gases: H_2 and CO , that are often highly diluted by steam (H_2O), and – in some scenarios – with reduced oxygen (O_2) concentration. All of this is further complicated by non-standard conditions of elevated pressure and temperature. Furthermore, hydrogen-dominated flame fronts are unstable in lean conditions, requiring a careful consideration of the effect of intrinsic flame instabilities.

Perhaps the greatest challenge of all comes from the multi-scale nature of the involved phenomena. Geometric scale of a typical reactor containment is many orders of magnitude larger in comparison to the physical and chemical scales of a flame front (Figure 1.2). This makes numerical modeling by applying straightforward methods relying on resolving the internal flame structure in order to predict the flame speed unattainable for the computational resources available today. Hence, the development of Computational Fluid Dynamics (CFD) methods is focused at deriving efficient models for all relevant underlying phenomena.



(a) Konvoi containment volume $\approx 70\,000\text{ m}^3$



(b) EPR containment volume $\approx 80\,000\text{ m}^3$

Figure 1.2: Schematic diagrams of the two European PWR reactor types, the EPR and Konvoi. The reactor containment is contoured with a blue line.

1.2.2 State of the art

In the last several decades, the use of numerical methods – and CFD in particular – has seen a steady rise in adoption across many engineering fields. Due to motivations outlined in Section 1.1, nuclear safety had an especially strong interest in driving the development of numerical methods. Several tailor-made CFD tools emerged in the realm of reactor safety.

One such CFD analysis tool is GASFLOW (Travis et al., 1998), developed at Los Alamos National Laboratory (LANL) and Karlsruhe Institute of Technology (KIT) for simulating gas distribution and mixing in large volumes. In parallel to the GASFLOW development, a family of CFD tools for combustion modeling was introduced, V3D and COM3D for deflagrations and DET3D for detonations. While V3D solved a semi-implicit incompressible formulation of the Navier–Stokes (NS) equations, aimed at slow flames in the early stage of an explosion, COM3D used a transient, explicit compressible formulation of the NS equations for fast deflagrations (Breitung and Royl, 2000). DET3D was built specifically for stable detonation propagation, relying on an explicit formulation of Euler equations (Redlinger, 2008). A variety of closure models were implemented, e.g. COM3D used the Eddy Break-up (EBU) combustion model and a widely-adopted $k-\epsilon$ two-equation turbulence model (Bielert et al., 2001). Tools from the GASFLOW family implement the Finite Volume Method (FVM) on structured grids which is simple to program and brings performance benefits in some cases, but generally makes resolving complex industry-scale geometries difficult (Kim and Hong, 2015).

Meanwhile, at the Commissariat à l’Energie Atomique (CEA, eng. "French Atomic Energy Commission") and the Institute for Radiological Protection and Nuclear Safety (IRSN) the computational tool TONUS (Kudriakov et al., 2008) was developed to incorporate the Lumped Parameter (LP) and CFD methods for applications to both the gas distribution and combustion. Two solvers were implemented for combustion CFD: a pressure-based Finite Element Method (FEM) for slow flames and a density-based compressible FVM for detonations, both on unstructured grids. The EBU model was implemented for combustion modeling and a $k-\epsilon$ model for turbulence modeling,

the latter being modified to incorporate buoyancy effects on turbulence generation (Kudriakov et al., 2008).

Reactor safety is one of the research interests of the European Commission's Joint Research Centre (JRC) where the in-house code REACFLOW was developed by Wilkening and Huld (1999). It too implements the at-the-time industry standard $k-\epsilon$ model for turbulence, while the combustion model used was the Eddy-Dissipation Combustion (EDC) model in which chemical reaction rates are determined solely by the extent of turbulent mixing. REACFLOW implements a compressible Navier-Stokes FVM method on unstructured grids with automatic refinement and Roe's approximate Riemann solver (Wilkening and Huld, 1999).

A publication by Bielert et al. from 2001 brought an overview of the CFD software for analysis of nuclear-safety-relevant combustion available at the time, together with a benchmark study of their capabilities. The participating codes were COM3D, GASFLOW, REACFLOW, TONUS and CFX. All codes in the study approached the question of deflagration flame speed closure using combustion models developed for general-purpose CFD (Bielert et al., 2001). Another way was pursued by Efimenko and Dorofeev (2001) where the combustion model "CREBCOM" was developed specifically for safety-relevant combustion, focused on conservative modeling. This simple model imposes a constant value of an experimentally estimated maximum flame speed for a given flame regime: slow deflagration, fast deflagration or detonation. Such-defined constant combustion source term is applied on a given grid cell once its neighboring cells reach a predetermined level of combustion completeness. Such a model, although simple to implement, produces spurious oscillations in the fluid flow. The CREBCOM model was later implemented in several other codes, including TONUS and COM3D.

All the codes in cited publications (Bielert et al., 2001; Efimenko and Dorofeev, 2001) covered a distinct regime of flame propagation, while the workflow for a complete accident analysis consisted of applying these separate tools, each in its respective area of validity and requiring manual transfer of results between them (Breitung and Royl, 2000). The limits of the distinct flame regimes were determined using empirical transition criteria, derivation of which is outlined

in more detail by Breitung et al. (2000). Such a divide-and-conquer approach is partly understandable in the context of efficient CFD tool development, since the most optimal numerical method and models are selected for different physical regimes of each stage. For example, in contrast to deflagrations, modeling of detonation waves is more straightforward, since their speed is fully determined by the two states of the gas in front (unburned) and behind (burned) the coupled shock–flame front. Furthermore, detonations are so fast that any influence of slower physical processes, e.g. diffusion, turbulence or heat transfer can be neglected and inviscid Euler equations can typically be used. In case of deflagrations, apart from requiring consideration of multiple physical processes, the speed of the flame front is indeterminate in reacting Navier–Stokes equations at scales of interest. A flame-speed closure is required taking into account all the influencing factors such as chemistry, diffusion, local fluid flow and turbulence. However, the approach consisting of distinct tools and depending on manual switching between them demonstrates fundamental limitations. Such a procedure does not allow for time-accurate modeling of the entire course of flame propagation, which may be locally influenced by many interdependencies between involved physical phenomena. These can be particularly significant if the onset of DDT is to be predicted (Breitung et al., 2000).

More recently, Beccantini and Studer (2010) proposed a method based on a Riemann solver for reacting flow equations, implemented in the framework of the Discrete Equation Method (DEM), first derived for multiphase flow by Saurel and Lemetayer (2001). The method theoretically allows for continuous transition from deflagration to detonation regimes by explicitly accounting for the wave speed of the propagating reactive discontinuity in the Riemann solver formulation. The flame speed in the deflagration regime still requires closure by an appropriate empirical flame speed correlation, as discussed above. While other cited approaches used various operator splitting schemes for addition of combustion terms to Euler or Navier–Stokes equations, the Riemann solver method by Beccantini and Studer (2010) calculates the reacting flow fluxes directly. Later work by Tang et al. (2014a; 2014b) improved the accuracy of the method around sharp discontinuities using upwind-downwind controlled discretization. The numerical method was implemented in the

CFD tool for large-scale explosions EUROPLEXUS, jointly developed by a consortium of CEA, EDF (Electricity of France), ONERA (The French Aerospace Lab). EUROPLEXUS validation by Velikorodny et al. (2015) and Studer et al. (2014) included simulations at reactor-safety-relevant conditions in both deflagration and detonation regimes. The drawback of the solver is that only Euler equations are solved, while numerical dissipation originating from discretization schemes is modified in an attempt to model physical viscosity.

Meanwhile, the GASFLOW family of solvers received an overhaul with their functionalities recently having been combined in a single package: GASFLOW-MPI (Multi-Physics-Integration) by Xiao et al. (2017a). The tool has been extended with a pressure-based solution algorithm for calculation of flows at all speeds using a combined Implicit Continuous-Fluid Eulerian and the Arbitrary-Lagrangian-Eulerian method (ICED-ALE). Furthermore, extensive heat transfer modeling capability has been added (Xiao et al., 2017a).

The Flame Acceleration Simulator (FLACS) (Arntzen, 1998; Middha and Hansen, 2008) is another example of a commercial code, tailor-made for explosion safety. Unlike the other codes cited above, FLACS was first developed for the oil and gas industry, but later also applied to nuclear safety. Apart from hydrogen, it can work with a wide range of hydrocarbon fuels. A number of models useful for large-scale industrial geometries has been implemented, such as a distributed porosity model for sub-grid modeling of various smaller structures. It implements its own empirical criterion for estimating the DDT probability based on a pressure gradient across the flame front (Middha and Hansen, 2008).

Apart from in-house or commercial tools developed specifically for explosion safety, a number of efforts in the field used general-purpose commercial CFD software for the task. JRC published a series of validation studies for a Reynolds-averaged Navier–Stokes (RANS) modeling approach using a flame speed closure based on the progress variable gradient source term. The commercial CFD package Fluent was used in these studies. Validations ranged from hydrogen deflagration experiments with homogeneous (Sathiah et al., 2012a,b, 2016a) and stratified hydrogen–air mixtures (Sathiah et al., 2016b), as well as in presence of diluents (Sathiah et al., 2015; Cutrono Rakhimov et al.,

2017). An extension of the approach to quasi-laminar combustion in weak turbulence was attempted by Holler et al. (2022) using a modified EBU model. The same commercial package and the gradient-based closure were used by Molkov et al. (2004; 2006a; 2006b; 2008) for large-scale hydrogen deflagrations. Furthermore, the model was extended to include a fractal-based term for self-induced wrinkling occurring in large-scale hydrogen flames at quiescent initial conditions. The Large Eddy Simulation (LES) formulation was used, which generally requires spatial resolution in the inertial range of the turbulence spectrum to correctly predict the sub-grid turbulent eddy viscosity. However, in this case, the use of LES on coarse grids was justified by the authors with the presence of negligible initial turbulence levels, i.e. quasi-laminar conditions. Validations for industrial applications were demonstrated in (Molkov et al., 2007, 2008).

The general-purpose commercial CFD code CFX was initially used at Technical University Munich (TUM), e.g. by Poruba (2003) who used the probability density function (PDF) combustion model in the benchmark study by Bielert et al. (2001), or by Katzy et al. (2017a,b) to implement a newly-derived empirical model for small-scale intrinsic instabilities of lean hydrogen flames. However, a lack of detailed understanding and control over the closed-source implementations in commercial software can create numerous limitations for the model development by the experts in the field. Additionally, benefits of free code exchange and community-driven contributions that are inherent to open-source software have been recognized by a growing number of researchers as important for further development of the explosion safety research. Within the framework of the open-source library Open Field Operation and Manipulation (OpenFOAM) (Weller et al., 1998), Ettner et al. (2014) introduced a method for safety-relevant combustion simulation with the focus on DDT prediction. The solver named *ddtFoam* developed at TUM was successfully validated with laboratory-scale DDT experiments in the GraVent explosion channel (Ettner et al., 2014). The CFD solution was based on the density-based formulation of Navier–Stokes equations allowing for efficient resolution of gas dynamics effects that are relevant to fast flames. OpenFOAM’s handling of unstructured grids allows representation of complex geometries which can be encountered in the nuclear safety context. A numerical

modeling approach aimed at large scales was proposed by Hasslberger (2017) in which the reacting discontinuity was tracked by a volume-of-fluid method that assumes an infinitesimally thin flame front. Work by Hasslberger et al. (2017b) introduced the models for combustion under the influence of steam dilution. Further development of the CFD methodology by means of extension to mixtures containing both hydrogen and carbon monoxide as fuels, which can be produced in the ex-vessel phase of the reactor accident (MCCI), was achieved by Barfuss et al. (2019). The CFD methodology based on *ddt-Foam* was later applied to chemical and process plant safety by Wieland et al. (2021) for the hydrocarbon ethylene.

1.2.3 Objectives of the present work

The present work continues the efforts toward development of an open-source tool for safety-relevant combustion phenomena based on OpenFOAM, in spirit of the lineage starting with the work by Ettner et al. (2014), described in the previous Section (Section 1.2.2).

Starting anew with an implementation of a density-based FVM method with robust and efficient explicit time integration scheme for transient simulations, and together with an all-speed numerical flux formulation, the aim of the present work was to enable end-to-end capturing of the entire range of phenomena from ignition, slow and fast deflagrations to DDT, recognizing the importance of developing simulation frameworks free from reliance on empirical transition criteria. The numerical method developed in the present work is implemented in an OpenFOAM extension library named *explosionDynamics-Foam*.

Furthermore, the present work aims to further the development of efficient modeling approaches for hydrogen flame propagation by introducing and validating a model for Darrieus–Landau instability effects on the flame speed, valid in conditions of low turbulence, which are common in the safety domain.

Finally, an application of the developed numerical simulation method to a full-scale Konvoi reactor containment is another goal, which demonstrates an example of integration of combustion CFD into the reactor accident analysis chain.

1.3 Outline of the thesis

The motivation and the goals of the present thesis are outlined in the introductory Chapter 1. Further chapters of the thesis are conceptually divided into four parts as follows.

Part I presents the numerical simulation method, where in Chapter 2 the theoretical background and in Chapter 3 the first validation in the deflagration flame regime are given.

Part II presents the scale-adaptive model for the effects of the Darrieus–Landau (DL) hydrodynamic instability on quasi-laminar flames. Chapter 4 provides an introduction to the DL instability modeling, particularly from the perspective of large-scale applications. Chapters 5 and 6 detail the derivation and the validation of the model for the DL instability effects developed in the present work. Concluding remarks of Part II are given in Chapter 7.

Part III deals with the application of the CFD modeling to combustion in a full-scale nuclear reactor containment. Chapter 8 gives an overview of previous full-scale CFD studies in the literature, followed by the outline and the goals of the analysis in the present work. Chapter 9 details the computational setup and the results of the flame propagation simulation in the Konvoi reactor containment using the methods from Parts I and II. Chapter 10 concludes the Part III.

Finally, Part IV summarizes the main findings of the thesis in Chapter 11 and gives an outlook for future research in Chapter 12.

Part I

Numerical Method for Large-scale Combustion Phenomena

2 Compressible reacting flow

A theoretical foundation of the numerical method implemented in the Open-FOAM extension library *explosionDynamicsFoam*, developed and applied in the present work will be provided in the following. At first, by presenting the set of equations for reacting flow, followed by thermodynamic, turbulence and combustion models. In the end, time integration methods used for achieving efficient transient solution will be presented.

2.1 Governing equations

Dynamics of compressible reacting flows are described by the Navier–Stokes equations. These consist of a set of nonlinear Partial Differential Equations (PDEs) expressing the conservation laws of mass, linear momentum, energy, and chemical species. These can be expressed as a single coupled equation in integral form

$$\frac{\partial}{\partial t} \int_V U_i dV + \oint_S (F_i - G_i) n_j dS = \int_V Q_i dV \quad (2.1)$$

where U_i is the conservative variable vector, F_i the inviscid flux vector, G_i the viscous flux vector, and Q_i the volumetric source vector.

A differential form of these conservation laws can be derived by applying Gauss divergence theorem to the surface integrals, assuming that fluxes and surface sources are continuous. The differential form is more restrictive, requiring the fluxes to be differentiable, which is not the case in presence of shock waves, for instance. Moreover, the integral form corresponds with how the FVM approximates the system of PDEs that express the conservation laws, which is by evaluating the fluxes at the surfaces of finite volumes, resulting is a set of algebraic equations that are solved by a chosen numerical solution

algorithm. The average value of the solution over a finite volume is a result of balance of fluxes and sources. One important strength of the FVM is that such explicit treatment of fluxes helps in producing a conservative method. In the present work, a cell-centered formulation of the FVM is used by means of explicit spatial discretization operators implemented in OpenFOAM (Weller et al., 1998).

Components of U_i are given by

$$U_i = \begin{bmatrix} \rho \\ \rho u_i \\ \rho E \\ \rho b \end{bmatrix} \quad (2.2)$$

where ρ is the density, u_i the velocity vector, E the total energy, and b the reaction regress variable defined such that $b = 1$ for the reactants and $b = 0$ for products. The total energy E is a sum of the kinetic energy and the internal energy

$$E = e + \frac{u_i u_i}{2}. \quad (2.3)$$

The relation between internal energy e and enthalpy h is given by

$$h = e + \frac{p}{\rho}, \quad (2.4)$$

which is defined as the sum of sensible enthalpy h_s and chemical enthalpies h_c of individual species in the gas mixture

$$h = h_s + h_c \quad (2.5)$$

$$h = h_s + \sum_l x_l \Delta h_f^l, \quad (2.6)$$

where x^l is the molar fraction and h_f^l heat of formation of specie l . The enthalpy defined in this way is sometimes called absolute enthalpy.

The definitions of F_i , G_i , and Q_i read

$$F_i = \begin{bmatrix} \rho u_j \\ \rho u_i u_j + p \delta_{ij} \\ (\rho E + p) u_j \\ \rho b u_j \end{bmatrix}, \quad G_i = \begin{bmatrix} 0 \\ \sigma_{ij} + \tau_{ij} \\ u_i (\sigma_{ij} + \tau_{ij}) + \lambda_{\text{eff}} \left(\frac{\partial T}{\partial x_j} \right) \\ \rho \Gamma_{\text{eff}} \left(\frac{\partial b}{\partial x_j} \right) \end{bmatrix}, \quad Q_i = \begin{bmatrix} 0 \\ \rho g_i \\ \rho g_i u_i \\ \dot{\Omega} \end{bmatrix} \quad (2.7)$$

2.1 Governing equations

where p is the pressure, T is the temperature, λ_{eff} is the effective thermal conductivity of the gas mixture, σ_{ij} is the viscous stress tensor, τ_{ij} is the turbulent stress tensor, Γ_{eff} is the effective diffusivity, g_i is the gravitational acceleration and $\dot{\Omega}$ is the volumetric consumption rate of the unburned mixture. The presented set of equations is completed using the equation of state for a thermally perfect gas:

$$p = \rho RT, \quad (2.8)$$

$$T = \frac{h_s}{C_p(T)}, \quad (2.9)$$

where R is the specific gas constant, and $C_p(T)$ the temperature-dependent specific heat at constant pressure defined as

$$C_p(T) = \sum_l \int_{T_{\text{ref}}}^T c_{p,l}(T) dT, \quad (2.10)$$

where the temperature dependency of $c_{p,l}$ is obtained from NIST-JANAF thermo-chemical tables (Chase, 1998). The specific sensible enthalpy can be calculated from the conserved energy

$$h_s = E - \frac{u_i u_i}{2} - h_c + \frac{p}{\rho}. \quad (2.11)$$

The use of absolute energies in the conservation equation leads to a convenient formulation in which there is no source term in the energy equation coming from chemical heat release. The only combustion source appears in the reaction regress variable conservation equation. In this way, the heat release due to chemical reaction gets explicitly accounted for in the mixture property update step at the end of each simulation time step.

Components of the viscous stress tensor σ_{ij} are given by

$$\sigma_{ij} = \mu \left(\frac{\partial u_i}{\partial x_j} + \frac{\partial u_j}{\partial x_i} \right) + -\frac{2}{3} \mu \frac{\partial u_k}{\partial x_k} \delta_{ij} \quad (2.12)$$

for a Newtonian fluid, using the Stokes' hypothesis, with μ being the viscosity coefficient. In a perfect gas, the dynamic viscosity μ depends on the temperature T , with the dependence empirically derived by Sutherland as

$$\mu = A_s \frac{T^{\frac{3}{2}}}{T + T_s} \quad (2.13)$$

where A_s is the Sutherland constant and T_s the Sutherland temperature of a given gas mixture (Sutherland, 1893).

The momentum diffusion models used in the present work are based on the eddy viscosity hypothesis which assumes that turbulent eddies cause additional mixing which enhances the diffusion in a way that is analogous to the molecular viscosity. Following that, the effects of turbulence can be modeled by the simple addition of turbulent viscosity to the molecular viscosity. The objective of turbulence modeling then becomes to correctly quantify the turbulent viscosity. An additional simplification is introduced by the Boussinesq hypothesis which assumes a linear dependence of the turbulent shear stress on the mean strain rate (which is proportional to the eddy viscosity). After Favre-averaging the Navier–Stokes equations and applying the eddy viscosity and Boussinesq hypotheses the turbulent stress tensor τ_{ij} becomes

$$\tau_{ij} = -\bar{\rho} \widetilde{u_i'' u_j''} = \mu_t \left(\frac{\partial \widetilde{u}_i}{\partial x_j} + \frac{\partial \widetilde{u}_j}{\partial x_i} \right) - \frac{2}{3} \mu_t \frac{\partial \widetilde{u}_k}{\partial x_k} \delta_{ij} - \frac{2}{3} \bar{\rho} \widetilde{k} \delta_{ij} \quad (2.14)$$

where the Favre-averaged specific turbulent kinetic energy

$$\widetilde{k} = \frac{u_i'' u_i''}{2} \quad (2.15)$$

is defined with respect to the fluctuating velocity u_i'' .

In cases where density changes are significant, mass-weighted averaging – known as Favre Averaging – is used to simplify the derivation of the governing equations that would otherwise become much more complex by accounting for all density fluctuation terms. For compressible (and reacting) flows, a particularly convenient formulation results from applying Reynolds averaging to density and pressure and Favre averaging to the rest of the variables.

A generic Favre-averaged quantity $\widetilde{\Phi}$ is related to its Reynolds average by

$$\widetilde{\Phi} = \frac{\overline{\rho \Phi}}{\bar{\rho}}. \quad (2.16)$$

where the Reynolds average $\bar{\Phi}$ is obtained by ensemble averaging

$$\bar{\Phi} = \lim_{N \rightarrow \infty} \frac{1}{N} \sum_{n=i}^N \Phi. \quad (2.17)$$

Furthermore, the turbulent thermal and scalar diffusion need to be defined. The effective thermal conductivity in Equation 2.7 is defined as a sum of the thermal conductivity of the fluid λ and an additional conductivity due to turbulence:

$$\lambda_{\text{eff}} = \lambda + \lambda_t \quad (2.18)$$

and

$$\lambda_t = C_p \frac{\mu_t}{\text{Pr}_t}, \quad (2.19)$$

where C_p is the specific heat of the mixture at constant pressure, μ_t the turbulent eddy viscosity and Pr_t the turbulent Prandtl number.

A passive scalar approach is taken for the diffusion modeling of the regress variable (Equation 2.7), where the effective diffusivity is defined as

$$\Gamma_{\text{eff}} = \Gamma + \Gamma_t \quad (2.20)$$

and

$$\Gamma_t = \frac{\mu_t}{\text{Sc}_t \bar{\rho}} \quad (2.21)$$

where Γ is the molecular diffusivity of the mixture, μ_t the turbulent eddy viscosity and Sc_t the turbulent Schmidt number.

Taking into account that Pr_t and Sc_t are constants in a RANS framework, Equations 2.19 and 2.21 show that turbulent transport phenomena are a function of turbulent eddy viscosity. In Section 2.3 ways of obtaining μ_t will be discussed.

2.2 Combustion modeling

Explosion dynamics are driven by the release of thermal energy resulting from chemical reactions. The media involved are gaseous, while the reactants can be considered premixed. In the efficient modeling framework used in the present work, complexity that exists in the chemistry of premixed combustion is largely simplified with the assumption of a single, global, one-step, irreversible chemical reaction from reactants to products.

A typical deflagration occurs in conditions of a high Damköhler number ($Da \gg 1$) (Poinsot and Veynante, 2005; Lipatnikov, 2012), where the flame front thickness can be considered small – its size being negligible compared to the scale of the whole combustion system. However, the position of the flame front is locally unsteady, with flame-flapping taking place at a relatively high frequency compared to the time scale of the flame front propagation. A mean flame brush is thus defined as an ensemble average of the thin flame surface. The position, thickness and displacement speed of the mean flame brush is analyzed in the RANS framework.

The Favre-averaged reaction regress variable b indicates the average state of the global reaction at a certain position in the computational domain, its transport equation given by

$$\frac{\partial \bar{\rho} \tilde{b}}{\partial t} + \frac{\partial (\bar{\rho} \tilde{u}_j \tilde{b})}{\partial x_j} = \frac{\partial}{\partial x_j} \left(\bar{\rho} \Gamma_{\text{eff}} \frac{\partial \tilde{b}}{\partial x_j} \right) + \dot{\Omega}. \quad (2.22)$$

The value of the regress variable is unity ($b = 1$) in the unburned mixture, decreases through the flame brush, and assumes the value of zero ($b = 0$) in the fully burnt mixture. Such a definition is different from the more common progress variable c which is zero in the unburnt and unity in the burned gas. However, the two are conceptually equivalent since $c = 1 - b$. The b is named "regress" variable for purpose of easier differentiation (Nwagwe et al., 2000). The reason why b is used in combustion models developed by Weller (1993) and Weller et al. (1998b) in the framework of OpenFOAM is that it allows for easier numerical handling in certain situations, e.g. when an ignition source term of the progress variable is introduced in the numerical model and the b equation is solved for using implicit solvers.

The statistical background of the definition of the progress variable was given by Bray and Moss (1977) and Bray and Libby (1986). Local, Favre-averaged temperature in present work is calculated by extending the Equation (2.8):

$$\tilde{T} = \frac{h_s}{C_{p,u}} \tilde{b} + \frac{h_s}{C_{p,b}} (1 - \tilde{b}) \quad (2.23)$$

where subscript u denotes the unburnt state and subscript b the burnt state, h_s is the specific sensible enthalpy calculated by the conservation law (Equa-

tion 2.1), and $C_{p,u}$ and $C_{p,b}$ are the specific heat coefficients for the unburned and the burned mixture calculated using Equation 2.10. It is the temperature obtained by Equation 2.23 that is used in the Equation 2.8. The importance of strict implementation of Equation 2.23 for obtaining accurate reacting flow simulations was reported by Yasari (2013).

2.2.1 Reaction rate closure

The main goal of premixed combustion modeling consists in predicting the reaction rate, which is in Equation 2.22 approximated by the rate of change in the regress variable ($\dot{\Omega}$). Using the regress variable gradient to close the burning rate, the source term reads

$$\dot{\Omega} = \rho_u \Xi S_l \left| \frac{\partial b}{\partial x_j} \right| \quad (2.24)$$

where ρ_u is the unburned gas density, S_l the laminar flame speed and Ξ the flame wrinkling factor. The effective flame speed $S_{\text{eff}} = \Xi S_l$ is applied in the

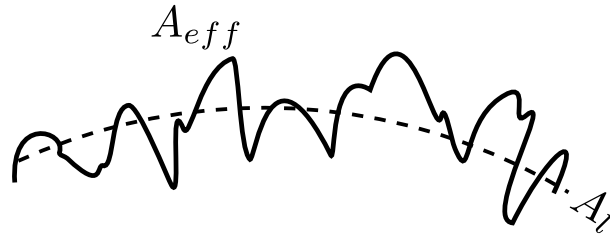


Figure 2.1: Schematic depiction of wrinkled (A_{eff}) and smooth (A_l) flame surfaces.

reaction rate closure in Equation 2.24. According to the thin flame front assumption ($Da \gg 1$), the ratio between laminar flame speed S_l – which depends only on the unburned mixture properties and thermodynamic state – and the effective flame speed S_{eff} is equal to the wrinkling of the flame front Ξ . Wrinkling is defined as the ratio of the flame front area in a wrinkled (A_{eff}) and an unwrinkled flame (A_l). The increase in the flame front area is proportional to the increase in the burning rate.

$$\Xi = \frac{S_{\text{eff}}}{S_l} = \frac{A_{\text{eff}}}{A_l}. \quad (2.25)$$

The laminar flame speed S_l is provided as an input to the CFD solution method. In case of hydrogen fuel, experimentally derived values by Konnov (2008), corrected for the thermodynamic state according to highly-resolved One-dimensional (1D) flame simulations with detailed chemical kinetics by Katzy (2021) were used, while the influence of steam dilution on the laminar flame speed was corrected according to Marshall (1986).

For hydrogen – carbon monoxide – air and hydrogen – carbon monoxide – air – steam mixtures the input data for the laminar flame speed was derived by Barfuss et al. (2019) using detailed chemical reaction mechanism by Li et al. (2015) including the corrections for the thermodynamic state and steam dilution influence.

The unburned density in Equation 2.24 is defined as $\rho_u = p/(R_u T_u)$, where R_u is the specific gas constant of the unburned mixture, and the unburned temperature T_u is calculated using the isentropic relation

$$T_u = T_0 \left(\frac{p}{p_0} \right)^{\frac{\kappa_u - 1}{\kappa_u}} \quad (2.26)$$

with κ_u being the ratio of specific heats $C_{p,u}/C_{v,u}$ in the unburned mixture, and T_0 and p_0 initial state of temperature and pressure prior to combustion. The approximation of T_u using an isentropic relation (2.26) is justifiable for the deflagration regime since pressure gradients in the vicinity of the slow flame front are generally weak (Hasslberger, 2017).

2.3 Turbulence modeling

Turbulent flow consists of fluctuations of different scales ranging from the largest – the integral length scale – to the smallest – the Kolmogorov length scale. Transient Navier–Stokes equations are able to fully describe the turbulent flow of all scales. However, a straightforward numerical modeling – known as Direct Numerical Simulation (DNS) – represents a task that is computationally overly expensive at scales of technical applicability. The number of grid cells required for DNS scales with $Re^{\frac{9}{4}}$ and the computational effort

with Re^3 . With current computational power, only problems in the range of $Re = 10^4 - 10^5$ are attainable. Another approach called LES is possible, where the direct solution of unsteady Navier–Stokes is used down to a certain scale of eddies, while a closure model is necessary to account for turbulence at smaller scales. The main difficulty with LES is ensuring a transition between resolved (directly simulated) and modeled scales occurs at a correct range of turbulent scales. For most industrial applications of CFD, RANS is used. In that approach, only mean variables are computed and all turbulent fluctuations are accounted for by closure modeling. When time-dependent change of the mean is captured, the term Unsteady Reynolds-averaged Navier–Stokes (URANS) is used.

In the present work – due to very large scales of nuclear plants – the grid resolution will generally only permit a RANS approach. Since flame propagation is a time-dependent problem – even when statistically averaged flame front is modeled – URANS will be used. The next few sections (2.3.1 and 2.3.2) will briefly present the background of the turbulence models used.

2.3.1 SST model

The k – ω Shear Stress Transport (SST) turbulence model is a two-equation model formulated using the variables of turbulent kinetic energy k and turbulence eddy frequency ω . It was derived by Menter (1994), combining Wilcox’s k – ω model in the near-wall region with the k – ϵ model, which is suitable for high-Reynolds flows – away from the walls. The aim was to make use of the positive aspects of both, in their respective areas. The naming "Shear Stress Transport" refers to the modification of turbulent eddy viscosity calculation, which accounts for the transport of turbulent shear stresses by applying the observation by Bradshaw et al. (1967) of shear stress being proportional to the turbulent kinetic energy, which results in better behavior of the model in adverse pressure gradients compared to earlier models. The main disadvantage of the SST model is the need to explicitly calculate the nearest-wall distance.

The implementation in OpenFOAM is based on later publications from Menter and Esch (2001) and Menter et al. (2003). Moreover, the optional F_3

term for rough walls by Hellsten (1998) was added to the implementation. The model formulation presented in the following corresponds to the OpenFOAM version 10.

The equation for the turbulent kinetic energy k reads

$$\frac{\partial k}{\partial t} + \frac{\partial(u_j k)}{\partial x_j} - \frac{\partial}{\partial x_j} \left(\Gamma_{k,\text{eff}} \frac{\partial k}{\partial x_j} \right) = P_k - \beta_{\text{SST}}^* k \omega, \quad (2.27)$$

where $\beta_{\text{SST}}^* = 0.09$ is a constant model coefficient, $\Gamma_{k,\text{eff}}$ is the effective diffusivity of k , which will be defined later and P_k is the limited k production term defined as

$$P_k = \min [G, (c_1 \beta_{\text{SST}}^* k \omega)] \quad (2.28)$$

where $c_1 = 10$ is a constant model coefficient and

$$G = \nu_t S_2 \quad (2.29)$$

can be understood as a turbulence generation term, with

$$S_2 = S^2 \quad (2.30)$$

being the square of the scalar invariant measure of the strain rate S , defined as

$$S = \sqrt{2s_{ij}s_{ij}}, \quad (2.31)$$

where the strain rate

$$s_{ij} = \frac{1}{2} \left(\frac{\partial u_i}{\partial x_j} + \frac{\partial u_j}{\partial x_i} \right) \quad (2.32)$$

is the symmetric part of the velocity gradient tensor $\frac{\partial u_i}{\partial x_j}$.

The equation for the turbulence eddy frequency ω – which can be understood as the specific turbulence dissipation rate – reads

$$\begin{aligned} \frac{\partial \omega}{\partial t} + \frac{\partial(u_j \omega)}{\partial x_j} - \frac{\partial}{\partial x_j} \left(\Gamma_{\omega,\text{eff}} \frac{\partial \omega}{\partial x_j} \right) = \\ \gamma_{\text{SST}} \min \left\{ \frac{G}{\nu}, \left[\frac{c_1}{a_1} \beta_{\text{SST}}^* \omega \cdot \max(a_1 \omega, b_1 F_{23} S) \right] \right\} \\ - \beta_{\text{SST}} \omega^2 + (1 - F_1) CD_{k\omega}, \end{aligned} \quad (2.33)$$

where $a_1 = 0.31$ and $b_1 = 1$ are constant model coefficients, γ_{SST} and β_{SST} are blended model coefficients, F_1 and F_{23} are blending functions, and

$$CD_{k\omega} = 2 \frac{\alpha_{\omega 2}}{\omega} \frac{\partial k}{\partial x_j} \frac{\partial \omega}{\partial x_j}, \quad (2.34)$$

is the cross diffusion term with $\alpha_{\omega 2} = 0.856$.

The diffusivity of k and ω are defined

$$\Gamma_{k,\text{eff}} = \alpha_k \nu_t + \nu \quad (2.35)$$

and

$$\Gamma_{\omega,\text{eff}} = \alpha_\omega \nu_t + \nu, \quad (2.36)$$

where α_k and α_ω are blended model coefficients explained as follows.

In the SST model, the blending is performed between the model coefficients of the k - ϵ model and the original k - ω in such a way that the best characteristics of both models are applied. In the free-stream flow, the use of k - ϵ avoids the issue with the original k - ω , which is sensitive to inlet turbulence conditions, while the use of k - ω in boundary layers (near no-slip walls) benefits from not requiring any damping functions (Menter, 1994). The blended model coefficients are

$$\begin{aligned} \alpha_k &= F_1(\alpha_{k_1} - \alpha_{k_2}) + \alpha_{k_2}, \\ \alpha_\omega &= F_1(\alpha_{\omega_1} - \alpha_{\omega_2}) + \alpha_{\omega_2}, \\ \beta_{\text{SST}} &= F_1(\beta_1 - \beta_2) + \beta_2 \quad \text{and} \\ \gamma_{\text{SST}} &= F_1(\gamma_1 - \gamma_2) + \gamma_2, \end{aligned} \quad (2.37)$$

where the constant coefficients $\alpha_{k_1} = 0.85$, $\alpha_{\omega_1} = 0.5$, $\beta_1 = 0.075$ and $\gamma_1 = 5/9$ come from the k - ω set of coefficients and $\alpha_{k_2} = 1$, $\alpha_{\omega_2} = 0.856$, $\beta_2 = 0.0825$ and $\gamma_2 = 0.44$ come from the k - ϵ set coefficients.

The blending function F_1 appearing in Equations 2.33 and 2.37 is equal to unity in the viscous sublayer and the logarithmic region of the boundary layer, which activates the near-wall k - ω formulation, while its value asymptotically approaches zero, thus activating the k - ϵ formulation, in the wake region of the

boundary layer. The definition of F_1 reads

$$F_1 = \tanh \left[(arg_1)^4 \right], \quad (2.38)$$

$$arg_1 = \min \left\{ \min \left[\max \left(\frac{\sqrt{k}}{\beta_{SST}^* \omega y}, \frac{500\nu}{y^2 \omega} \right), \frac{4\alpha_{\omega_2} k}{CD_{k\omega+} y^2} \right], 10 \right\}, \quad (2.39)$$

where y is the distance to the nearest wall and

$$CD_{k\omega+} = \max(CD_{k\omega}, 10^{-10}) \quad (2.40)$$

is the positive (clipped) part of the cross-diffusion term (Equation 2.34), introduced for numerical stability.

The blending function F_{23} in Equation 2.33 reads

$$F_{23} = \begin{cases} F_2 & \text{default smooth wall,} \\ F_2 \cdot F_3 & \text{optional term } F_3 \text{ for rough walls,} \end{cases} \quad (2.41)$$

where the blending function F_2 , defined as

$$F_2 = \tanh \left[(arg_2)^2 \right], \quad (2.42)$$

$$arg_2 = \min \left[\max \left(\frac{2\sqrt{k}}{\beta_{SST}^* \omega y}, \frac{500\nu}{y^2 \omega} \right), 100 \right], \quad (2.43)$$

is equal to unity in boundary layers and approaches zero in free-shear layers and the blending function F_3 applies a correction for walls with significant roughness (Hellsten, 1998). The definition of F_3 reads

$$F_3 = 1 - \tanh \left[(arg_3)^4 \right], \quad (2.44)$$

$$arg_3 = \min \left(\frac{2\sqrt{k}}{\beta_{SST}^* \omega y}, 10 \right). \quad (2.45)$$

The model equations for k and ω (Equations 2.27 and 2.33) are solved once per time step by implicit linear iterative solvers. After that, the turbulent eddy viscosity ν_t is corrected as follows

$$\nu_t = \frac{a_1 k}{\max(a_1 \omega, b_1 F_2 S)}. \quad (2.46)$$

Commonly-used turbulence models in CFD, including the SST model, were derived for inert incompressible flows, where the only modification applied in case of compressible flow simulations is to multiply the resulting turbulent eddy viscosity by the density

$$\mu_t = \rho \nu_t. \quad (2.47)$$

All constant coefficients of the SST model can be found in Table 2.1.

Table 2.1: SST model coefficients.

a_1	b_1	c_1	α_{k1}	α_{k2}	$\alpha_{\omega 1}$	$\alpha_{\omega 2}$	β_1	β_2	β_{SST}^*	γ_1	γ_2
0.31	1	10	0.85	1	0.5	0.85616	0.075	0.0828	0.09	0.5532	0.4403

2.3.2 SAS model

In a steady-state RANS simulation, the straightforward statistical treatment of turbulence can be used, in which turbulent fluctuations of all scales can be averaged on a time interval that tends to infinity. Furthermore, the time derivatives of flow variables can be left out of the Equations 2.1, 2.27, and 2.33, the solution which is carried out until convergence to the averaged steady-state. In an unsteady RANS (URANS) simulation, in contrast to that, the time derivatives are required for capturing the globally unsteady flow and the governing equations are integrated in a series of finite time steps limited by the requirement to temporally resolve the transient phenomena of interest. The temporal and spatial discretization in URANS usually resolves a portion of the turbulent scales as well, making the RANS approach of averaging across all of the said turbulent scales no longer valid. The straightforward RANS averaging leads to unphysical results for most unsteady flows as it typically results in overpredictions of eddy viscosity, i.e. overly dissipative behavior (Menter and Egorov, 2005). The Scale Adaptive Simulation (SAS) model introduced by Menter and Egorov (2005) and Egorov and Menter (2008) attempts to mitigate the problem by dynamically adjusting the dissipation with respect to the resolved flow structures which are estimated using the von Kármán length scale. The difference between SAS and LES is that it does not explicitly divide the flow in RANS

and LES regions. It is a model capable of simulating turbulent structures down to the grid limit, but without introducing an explicit grid size dependency as in traditional LES.

The SAS model is an extension of the standard k - ω SST model described in Section (2.3.1). The model equations are otherwise equal to those in the base SST, but with the added source term in the ω equation (Equation 2.33), which reads

$$Q_{SAS} = \min \left\{ \max \left[\zeta_2 \kappa_{vK} S_2 \left(\frac{L}{L_{vK, SAS}} \right)^2 - C \frac{2k}{\sigma_\Phi} \max \left(\frac{\left| \frac{\partial \omega}{\partial x_j} \right|^2}{\omega^2}, \frac{\left| \frac{\partial k}{\partial x_j} \right|^2}{k^2} \right), 0 \right], \frac{\omega}{0.1 \Delta t} \right\} \quad (2.48)$$

where $\zeta_2 = 3.51$, $\sigma_\Phi = 2/3$, $C = 2$, and $\kappa_{vK} = 0.41$ are the constant model parameters, Δt is the time step, S_2 is the square of the scalar invariant measure of the strain rate (Equations 2.30 and 2.31), L is the length scale of the modeled turbulence calculated by

$$L = \frac{\sqrt{k}}{\omega \beta_{SST}^{*0.25}}, \quad (2.49)$$

and $L_{vK, SAS}$ is the von Kármán length scale defined as

$$L_{vK, SAS} = \max \left(\frac{\kappa_{vK} S}{\left| \frac{\partial^2 u_j}{\partial x_i^2} \right|}, C_s \sqrt{\frac{\kappa_{vK} \zeta_2}{\frac{\beta_{SST}}{\beta_{SST}^*} - \gamma_{SST}}} \Delta_x \right), \quad (2.50)$$

where $C_s = 0.11$ is a constant parameter, Δ_x is the grid spacing calculated as the cube root of the cell volume $\Delta_x = \sqrt[3]{V_{cell}}$.

The constant model parameters β_{SST} , γ_{SST} and β_{SST}^* originate from the base SST model and can be found in Table 2.1, while the parameters added in the formulation of the SAS source term can be found in Table 2.2.

Table 2.2: SAS model coefficients.

C	C_s	κ_{vK}	ζ_2	σ_Φ
2	0.11	0.41	3.51	2/3

2.4 All-speed convective fluxes

For discretization of the convective fluxes given in F_i (Equation 2.7), a large variety of approaches exist for inert gas flows within the framework of the Finite Volume Method (FVM). Schemes that are derived by considering the physical properties of hyperbolic terms are most widely used. Since they distinguish the propagation direction at a particular control volume face, they have been named *upwind* schemes.

There are two classes of methods among upwind schemes that are most common in density-based numerics. First, Flux Difference Splitting (FDS) methods are based on calculating the inter-cell flux by first evaluating the local discontinuous states (Riemann problem) at a cell interface according to the solutions of one-dimensional hyperbolic equations, an idea that was first introduced by Godunov, hence they are often called Godunov-type numerical methods (Toro, 2009).

The second approach, called Flux Vector Splitting (FVS) works by decomposing the vector of fluxes F_i into two parts, the convective and the pressure (acoustic) part. Characteristic variables are constructed so that they are similar to the eigenvalues of the convective flux Jacobian. The two decomposed parts are then discretized by upwind-biased difference schemes. The underlying approaches of the two classes of methods are sometimes called the *Riemann approach* and the *Boltzmann approach*. The formulation of FVS methods often allows for simpler implementation, which generally tends to be more efficient. A wide overview of discretization methods can be found in the textbook by Toro (2009). Schemes derived from the Liou's original Advection Upwind Splitting Method (AUSM) scheme are the most-widely used among the FVS-type schemes.

When accelerating flames are analyzed – starting from ignition – a wide range of flow conditions is encountered. However, upwind schemes of both FDS and FVS types were traditionally formulated for compressible gas dynamics, more precisely, high speed aerodynamics (Liou, 2010). They would often prove unsuitable outside the intended Mach number range – lacking stabil-

ity or accuracy (Ettner, 2013). Special formulations of all-speed numerical flux schemes were later developed in an attempt to address this shortcoming. The improved, all-speed formulation of the AUSM scheme, named AUSM⁺up was introduced by Liou (2006).

The AUSM⁺up scheme is adopted in the present work with the aim of enabling a wide range of flow and flame regimes. Although, it was originally derived for inert gas dynamics, the extension for the reaction progress b variable was straightforward.

In the FVS approach, the fluxes from Equation 2.7 are split into convective Ψ_i and pressure P_i parts:

$$F_i = u_j \Psi_i + P_i \quad (2.51)$$

where

$$\Psi_i = \begin{bmatrix} \rho \\ \rho u_i \\ \rho E + p \\ \rho b \end{bmatrix}, \quad P_i = \begin{bmatrix} 0 \\ p \delta_{ij} \\ 0 \\ 0 \end{bmatrix}.$$

Imagining an interface between two control volumes, we can denote the control volume to the left of the interface with a subscript L and the one to the right with a subscript R. Next, the mass flux at the control-volume interface, marked by index 1/2 is defined as

$$\dot{m}_{1/2} = u_{1/2} \rho_{L/R} = c_{1/2} \text{Ma}_{1/2} \rho_{L/R} \quad (2.52)$$

where $\rho_{L/R}$ is the density convected by velocity $u_{1/2}$ through the interface and

$$\text{Ma}_{L/R} = \frac{u_{L/R}}{c_{1/2}} \quad (2.53)$$

is the Mach number at the interface with $c_{1/2}$ being the speed of sound at that location.

Taking advantage of the physical meaning of velocity, components of $\Psi_{i,L/R}$ from Equation 2.51 (including density $\rho_{L/R}$) are determined by

$$\Psi_{i,L/R} = \begin{cases} \Psi_{i,L} & \text{if } \dot{m}_{1/2} > 0 \\ \Psi_{i,R} & \text{otherwise} \end{cases} \quad (2.54)$$

Left L and right R states of Ψ_i are interpolated from cell centers to the control-volume interfaces using the second-order Monotonic Upstream-centered Scheme for Conservation Laws (MUSCL) reconstruction scheme by (van Leer, 1979).

Furthermore, the mass flux $\dot{m}_{1/2}$ needs to be approximated. For that, $c_{1/2}$ and $\text{Ma}_{1/2}$ are needed according to the Equation 2.52. Using left and right states, $\text{Ma}_{1/2}$ is given by

$$\text{Ma}_{1/2} = \mathcal{M}_{(n)}^+ (\text{Ma}_L) + \mathcal{M}_{(n)}^- (\text{Ma}_R) + M_p \quad (2.55)$$

The pressure diffusion term M_p is defined by Equation 2.60, and split Mach numbers $\mathcal{M}_{(n)}^\pm$ are polynomial functions of degree $n = 1, 2, 4$, given by

$$\begin{aligned} \mathcal{M}_{(1)}^\pm (\text{Ma}) &= \frac{1}{2} (\text{Ma} \pm |\text{Ma}|), \\ \mathcal{M}_{(2)}^\pm (\text{Ma}) &= \pm \frac{1}{4} (\text{Ma} \pm 1)^2 \quad \text{and} \\ \mathcal{M}_{(4)}^\pm (\text{Ma}) &= \begin{cases} \mathcal{M}_{(1)}^\pm (\text{Ma}) & \text{if } |\text{Ma}| \geq 1, \\ \mathcal{M}_{(2)}^\pm \left(1 \mp 16\beta_{\text{Ma}} \mathcal{M}_{(2)}^\pm (\text{Ma})\right) & \text{otherwise,} \end{cases} \end{aligned} \quad (2.56)$$

where parameter $\beta_{\text{Ma}} = 1/8$. The speed of sound at the interface $c_{1/2}$ is defined as

$$c_{1/2} = \min(\hat{c}_L, \hat{c}_R) \quad (2.57)$$

$$\hat{c} = \frac{c^{*2}}{\max(c^*, |u|)}, \quad (2.58)$$

where, for a perfect gas, the following relation is valid

$$c^{*2} = \frac{2(\kappa - 1)}{\kappa + 1} H. \quad (2.59)$$

Here, c^* is the critical speed of sound, κ is the ratio of specific heats C_p/C_v and H is the total enthalpy.

The pressure diffusion term, introduced by Liou (2006) in the AUSM⁺up scheme for coupling between pressure and velocity at low Mach numbers, is given by

$$M_p = -\frac{K_p}{f_a} \max\left(1 - \overline{\text{Ma}}^2, 0\right) \frac{p_R - p_L}{\rho_{1/2} c_{1/2}^2} \quad (2.60)$$

where

$$\rho_{1/2} = \frac{(\rho_L + \rho_R)}{2} \quad (2.61)$$

and

$$\overline{\text{Ma}}^2 = \frac{u_L^2 + u_R^2}{2c_{1/2}^2}. \quad (2.62)$$

The pressure flux at the interface reads

$$p_{1/2} = \mathcal{P}_{(n)}^+ (\text{Ma}_L) p_L + \mathcal{P}_{(n)}^- (\text{Ma}_R) p_R - p_u \quad (2.63)$$

with split Mach number polynomials with degree of $n = 1, 3, 5$ being

$$\mathcal{P}_{(5)}^\pm = \begin{cases} \frac{1}{\text{Ma}} \mathcal{M}_{(1)}^\pm (\text{Ma}) & \text{if } |\text{Ma}| \geq 1, \\ \mathcal{M}_{(2)}^\pm (\text{Ma}) \left[(\pm 2 - M) \mp 16\alpha_p \text{Ma} \mathcal{M}_{(2)}^\mp (\text{Ma}) \right] & \text{otherwise,} \end{cases} \quad (2.64)$$

where the parameter α_p is defined as

$$\alpha_p = \frac{3}{16} (-4 + 5f_a^2) \in \left[-\frac{3}{4}, \frac{3}{16} \right]. \quad (2.65)$$

Analogous to the pressure diffusion term (Equation 2.60), the momentum diffusion term is defined by

$$P_u = -K_u f_a c_{1/2} \mathcal{P}_{(5)}^+ \mathcal{P}_{(5)}^- (\rho_L + \rho_R) (u_R - u_L). \quad (2.66)$$

For low Mach number flows it is important to scale the numerical dissipation of the scheme proportionally to the local flow speed using a scaling function for the numerical speed of sound:

$$f_a = \text{Ma}_{\text{ref}} (2 - \text{Ma}_{\text{ref}}) \in [0, 1]. \quad (2.67)$$

Here, the reference Mach number Ma_{ref}^2 is

$$\text{Ma}_{\text{ref}}^2 = \min \left(1, \max \left(\overline{\text{Ma}}^2, \text{Ma}_{\text{lim}}^2 \right) \right) \in [0, 1] \quad (2.68)$$

where $\overline{\text{Ma}}^2 = 0.5 (\text{Ma}_L^2 + \text{Ma}_R^2)$ is the mean local Mach number, and $\text{Ma}_{\text{lim}} = \text{Ma}_\infty$ is the case-specific limiting Mach number.

Finally, the flux at the interface is calculated as follows

$$F_{i,1/2} = \dot{m}_{1/2} \begin{cases} \Psi_{i,L} & \text{if } \dot{m}_{1/2} > 0 \\ \Psi_{i,R} & \text{otherwise} \end{cases} + p_{1/2}. \quad (2.69)$$

2.4.1 Validation: plane-parallel Poiseuille flow

A Two-dimensional (2D) simulation of laminar flow in a gap between two parallel plates with height $h = 0.1$ m is used as a simple demonstration of the all-speed numerical method consisting of the density-based numerical method from Section 2.1, the AUSM⁺up spatial discretization and an Strong Stability Preserving (SSP)-Runge–Kutta (RK) time integration schemes (Section 2.5). The flow Mach number is $Ma = 0.05$, while the fluid is air at $p = 101325$ Pa and $T = 293$ K. The simulation was initialized with zero velocity in the domain, and run until the flow fully developed, i.e. the velocity profile reached its steady state. The flow was generated by the imposed constant pressure gradient. The result in Figure 2.2 shows agreement with the analytical solution. The result of the simulation shows no excess dissipation in the viscous, low-Ma flow case. Furthermore, no stability issues were encountered for Courant–Friedrich–Lewy (CFL) = 1 and the SSP parameter $m = 10$. Finally, the result was achieved without using low-Mach preconditioning techniques such as the one developed by Weiss and Smith (1995).

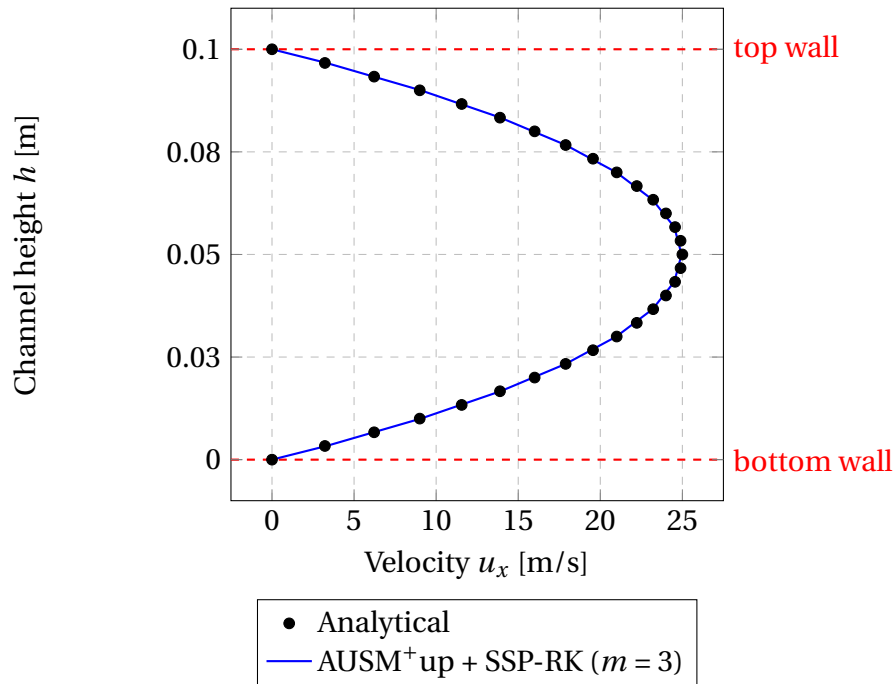


Figure 2.2: Results of plane-parallel Poiseuille flow at $Ma = 0.05$.

2.5 Efficient time integration

Flame propagation simulations in explosion safety, where large volumes and low initial flame speeds are present, are typically concerned with intervals of physical time on the order of $t \approx 1\text{--}10$ s. Given that a time-accurate transient simulation is limited by the CFL condition, a typical flame propagation study takes a large number of time steps to complete. In such conditions, the time integration method plays a large role in the overall efficiency. Given a low per-time-step computational cost of explicit methods, they are most competitive in the described situation. The explicit SSP RK time integration used for time integration in the present work will be explained in the following.

The system of governing equations (Equation 2.1), after discretization and approximation by the Finite Volume Method (FVM) leads to a system of coupled nonlinear ordinary differential equations

$$\frac{\Delta U_i V}{\Delta t} + R_i = 0 \quad (2.70)$$

where U_i is the vector of unknowns – conservative variables, V is the cell volume and R_i is the combined approximation of volume integrals of flux- (F_i and G_i in Equation 2.7) and source terms (Q_i in Equation 2.7). It represents the complete spatial discretization, and it is a non-linear function of time and the conservative variables $R_i(t, U_i)$. The system in Equation 2.70 is solved in each cell of the discretized computational domain.

There are several options for integrating Equation 2.70. Generally, explicit methods need the lowest computational effort per single time step, which makes them attractive for long-running transient simulations. A class of explicit time discretization techniques characterized as Strong Stability Preserving (SSP) have been designed specifically for solving systems of Ordinary Differential Equations (ODEs) resulting from spatial discretization of the hyperbolic partial differential equations that contain discontinuities (Gottlieb et al., 2011). It has been shown that traditional (non-SSP) methods can produce oscillatory solutions, even when the spatial discretization of the PDE system is Total Variation Diminishing (TVD) (Shu and Osher, 1988) and the linear stabil-

ity criterion is satisfied. SSP methods are of a similar form and generally have a comparable cost as traditional ODE solvers.

An approximate solution of the Equation 2.70 at the time level $n + 1$ denoted U_i^{n+1} is obtained using the RK method:

$$y_i = U_i^n + \Delta t \sum_{j=1}^{i-1} a_{ij} R(t^n + c_j \Delta t, y_j) \quad 1 \leq i \leq m, \quad (2.71)$$

$$U_i^{n+1} = U_i^n + \Delta t \sum_j^m b_j R(t^n + c_j \Delta t, y_j)$$

where a_{ij} , b_j , and c_j are the Butcher coefficients of the method and vector y_i contains intermediate values of individual stages; U_i^n is the approximation at the old time level and the time step is $\Delta t = t^{n+1} - t^n$. A straightforward implementation would require $m + 1$ memory registers for intermediate values of y_i .

In the present work, a low storage – refers to computer's Random Access Memory (RAM) – implementation of an optimal second order SSP Runge–Kutta (RK) method by Ketcheson (2010) is used. Low storage methods leverage the fact that it is possible to express the RK method using linear combinations of intermediate steps in such a way that storage of every stage can be avoided.

Low storage methods are best analyzed when written in the Shu-Osher form (Shu and Osher, 1988). That way, the linear dependencies among RK stages become apparent. The Shu–Osher form of a generic RK method (2.71) is given by

$$y_1 = U_i^n,$$

$$y_i = \sum_{j=1}^{i-1} (\alpha_{ij} y_j + \beta_{ij} \Delta t R(y_j)) \quad 2 \leq i \leq m + 1, \quad (2.72)$$

$$U_i^{n+1} = y_{m+1}.$$

More specifically, in the particular method used here, the second order Ketcheson (Ketcheson, 2010), y_i is defined as

$$y_i = \alpha_{i,1} U_i^n + \alpha_{i,i-1} y_{i-1} + \beta_{i,i-1} \Delta t R(y_{i-1}). \quad (2.73)$$

For an m -stage method, α_{ij} and β_{ij} are

$$\begin{aligned}\alpha_{i,i-1} &= \begin{cases} 1 & \text{if } 1 \leq i \leq m-1, \\ \frac{m-1}{m} & \text{if } i = m, \end{cases} \\ \beta_{i,i-1} &= \begin{cases} \frac{1}{m-1} & \text{if } 1 \leq i \leq m-1, \\ \frac{1}{m} & \text{if } i = m, \end{cases} \\ \alpha_{m,0} &= \frac{1}{m}.\end{aligned}\tag{2.74}$$

The number of stages of the scheme m can be increased to provide a greater level of stability which generally allows a greater time step size and, in turn, increased computational efficiency. The m is chosen prior to the computation.

The improvement in efficiency of the above-defined method is twofold. First, since memory bandwidth is usually the performance bottleneck for computing large problems on contemporary computers, the number of memory registers used by the method can have a direct impact on the performance. The main performance improvement, however, comes from an increase in the time step size, that – for a given level of accuracy – is attainable with SSP schemes, reducing the overall computational cost to solution.

The time step Δt in Equation 2.70 is determined from the CFL condition, defined as

$$CFL = \frac{(|u_i| + c) \Delta t}{\Delta_x}\tag{2.75}$$

where u_i is the convective velocity,

$$c = \sqrt{\kappa \frac{p}{\rho}}\tag{2.76}$$

the speed of sound in perfect gas and Δ_x the cell size, which can for unstructured polyhedral grids be calculated from the cell volume $\Delta_x = \sqrt[3]{V_{\text{cell}}}$.

2.5.1 Validation: Sod shock tube

A canonical case of shock propagation introduced by Sod (1978) is used here to validate the overall numerical approach and compare the relative perfor-

mance of different time integration methods in presence of sharp discontinuities. In Sod's configuration, the gas initially resides at rest in a long tube separated in half by a thin foil, with the states of the left and the right side defined as in Table 2.3. An analytical solution for the 1D shock propagation problem exists for a calorically perfect gas and will be used for numerical result validation in Figure 2.3.

Table 2.3: Initial left and right states of the Sod shock tube.

	left	right
ρ	1 kg/m ³	0.125 kg/m ³
p	10 ⁵ Pa	10 ⁴ Pa
T	348.4 K	278.7 K

The one-dimensional solution domain was chosen to match the shock tube tutorial case in the base OpenFOAM library (Greenshields et al., 2010) for easier result comparison. It is 10 m long in the x direction, with the $x = 0$ m located at the thin foil location in the middle. A coarse discretization using only 100 uniformly-spaced cells ($\Delta_x = 100$ mm) was used in order to clearly show the relative capabilities of different numerical methods.

The results in Figure 2.3 show the density at $t = 7$ ms from the beginning of the shock propagation, i.e. breaking of the thin foil separating the two states (Tab. 2.3).

The case was computed using a simple forward Euler time scheme and the SSP-RK for different CFL conditions to highlight the influence of the SSP method. All cases used the TVD high-resolution upwind scheme AUSM⁺up. For the Euler scheme at CFL = 0.6, the linear stability criterion (Equation 2.75) is satisfied, however, oscillations occur in the results, despite the spatial discretization of the PDE system using a TVD scheme. For the SSP-RK scheme at CFL = 2 and number of stages $m = 3$ no oscillations appear. A comparable accuracy can only be achieved at a much lower CFL = 0.27 with the forward Euler scheme.

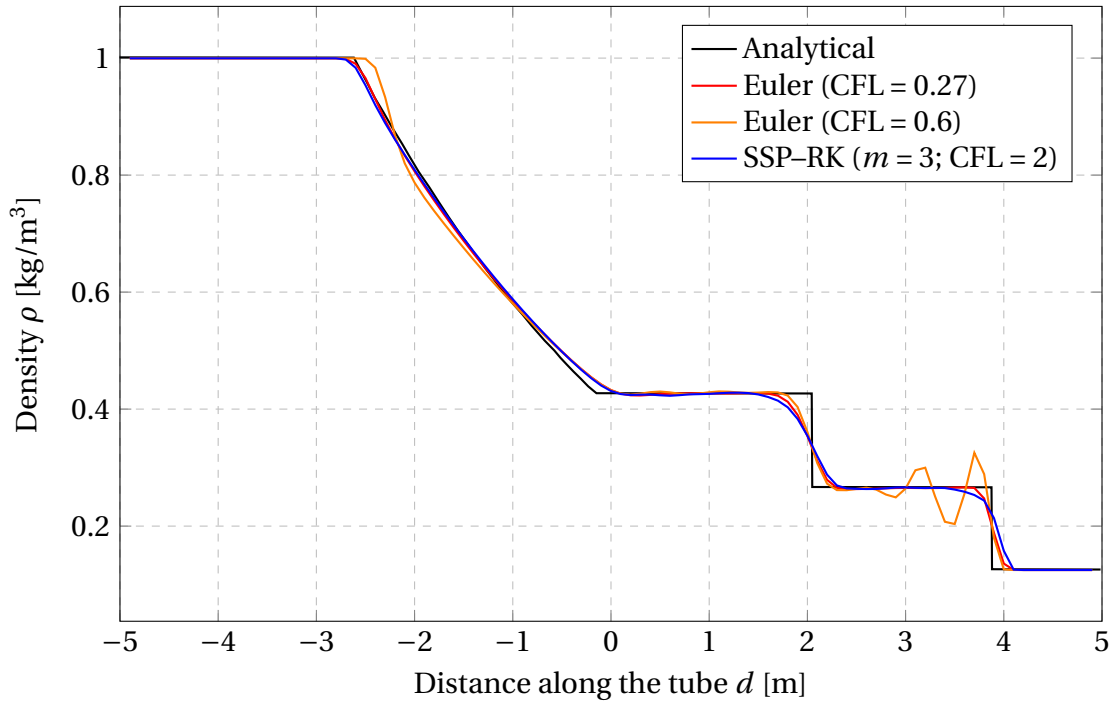


Figure 2.3: Sod (1978) shock tube case; 1D grid: 100 cells along the tube ($\Delta_x = 100$ mm).

Given that SSP-RK scheme with $m = 3$ is a three-stage method, while forward Euler is single-stage, a comparison of the end-to-end simulation time ($t = 0$ – 7 ms) is given in Table 2.4 to assess the performance. It can be seen that the SSP method results in a speedup of approximately a factor of three for the comparable level of accuracy. The computational performance of the SSP-RK

Table 2.4: Performance comparison of time integration methods for the Sod shock tube case.

Scheme	CFL_{\max}	CPU time	relative time
Euler	0.27	0.85 s	3.27
SSP-RK ($m = 3$)	2	0.26 s	1.0

relative to other schemes will be further analyzed for reacting flow on a case of turbulent hydrogen deflagration in Chapter 3.

3 Validation in the deflagration regime

This chapter presents validation of the numerical method described in Chapter 2 for the slow flame regime. Experimental results of pressure, flame position, and displacement speed are used for that purpose. The experiments were conducted in a spherical combustion vessel with turbulence generation. In the first part of the Chapter 3 the experimental setup will be shown, followed by the computational setup, simulation results and discussion.

3.1 Turbulent flame propagation in a spherical vessel

Experiments by Goulier et al. (2017a,b) were conducted in a spherical vessel with an internal diameter of 563 mm (total volume of 93.43 dm³). Turbulence inside the vessel was controlled by built-in fans.

The experimental work was motivated by nuclear reactor safety. The choice of mixtures and turbulence intensity was made such that they represent possible conditions within a reactor containment during an accident. The aim of the research was to study the flame propagation dynamics for lean hydrogen-air flames, and to generate validation data that can help in the improvement of CFD methods. Previously published CFD benchmarks showed a lack of available experimental validation data with measured initial turbulence conditions Bentaïb et al. (2014). Since the fresh gas turbulence strongly influences the flame propagation speed, this aspect of the code validation is seen as important for the development of the numerical safety analysis.

A set of eight fans was used for turbulence generation. The aim was creating a flow with a high velocity fluctuation, but a zero mean velocity (statistically stationary). Particle Image Velocimetry (PIV) technique was used to measure the instantaneous velocity fields within the vessel. The fans managed to gen-

erate homogeneous and isotropic turbulence within a diameter of 100 mm in the center of the vessel. Each intensity level of turbulence is characterized by the fan speed and its corresponding root-mean-square (rms) velocity u'_i . Turbulence length scale depends solely on fan blade geometry and varies from 43.9 mm to 52.4 mm. The three turbulence levels used in the validation of the present work are shown in Table 3.1.

Table 3.1: Turbulence intensity levels in the spherical vessel.

Turbulence level	u'_i [m/s]	Fan rpm [-]	k [m ² /s ²]	ω [1/s]
low	0.57	1000	0.48	26.05
medium	1.28	2000	2.44	58.78
high	2.1	3000	6.65	97.05

Four different hydrogen–air mixtures were experimentally investigated. Those are characterized by molar concentrations of hydrogen, that were 16%, 20%, 24% and 28%. These values correspond to the equivalence ratios of $\Phi = 0.45$, 0.6, 0.65 and 0.97, respectively. The maximum relative error of the equivalence ratio is reported to be 1.8%. An electric spark from two electrodes was used for ignition. Schlieren photography using a high speed camera was used for flame position while piezoelectric transducers – flush mounted in the wall – were used for pressure measurements. All experiments were performed at $p_0 = 100$ kPa and $T_0 = 293$ K. For each combination of mixture and turbulence, ten identical trials were performed. Cases with higher turbulence show a higher scatter in experimental results of the flame position. Furthermore, mixtures with lower hydrogen content show higher scatter as well. Pressure measurements, on the other hand, showed a very low standard deviation Goulier et al. (2017a,b).

3.2 Computational model and setup

The computational domain representing the whole combustion vessel (Domain A) consists of an one-eighth of a sphere. This domain was used for obtaining pressure rise results. The wall was modeled by no-slip boundary con-

ditions, while the rest of the domain boundaries are set to symmetry. The grid was block structured. It is shown in Figure 3.1. Cells size varied from 6 to 16 mm, while within the central area, the grid spacing is consistently 12 mm.

Flame position and displacement speed calculation was done on a reduced computational domain (Domain B) since the measured data for flame position is only available within the first 80 mm of the vessel radius – corresponding to the zone where isotropic homogeneous turbulence was maintained. For these simulations, a cubic domain with side length $a = 120$ mm and non-reflective open boundary conditions on far ends was used, with uniformly spaced grid ($\Delta_x = 5$ mm).

Ignition was performed in the first time step of the simulation, by switching the progress variable to burned state (from $b = 1$ to $b = 0$). Ignition was initiated in a single control volume at the center of the vessel (Figure 3.1).

The turbulence model $k-\omega$ SST-SAS described in Section 2.3.2 was used in all simulations. The turbulent Prandtl number Pr_t (Equation 2.18), and the turbulent Schmidt number Sc_t (Equation 2.20) were both set to one. No tuning of the two parameters was attempted. Pressure and momentum diffusion coefficients of the AUSM⁺ up flux scheme were $K_p = 0.25$, and $K_u = 0.75$ respectively, while the limiting Mach number was set to $M_{lim} = 0.6$. Case-specific parameters such as the CFL condition used or the number of Runge–Kutta stages (m) will be mentioned together with the results discussion in Sections 3.4 and 3.5.

Table 3.2: Properties of the investigated hydrogen–air mixtures: unstretched laminar flame speed S_l , laminar flame thickness δ_l and Lewis number Le .

x_{H_2} [%]	S_l [m/s]	$\delta_l = a_u / S_l$ [mm]	Le [-]
16	0.46	0.057	0.51
20	0.85	0.032	0.63
24	1.34	0.022	0.79
28	1.87	0.016	1.02

Simulations were conducted for all four experimentally investigated H₂ mixtures ($x_{H_2} = 16\%$, 20% , 24% , 28% vol.), at three levels of turbulence intensity.

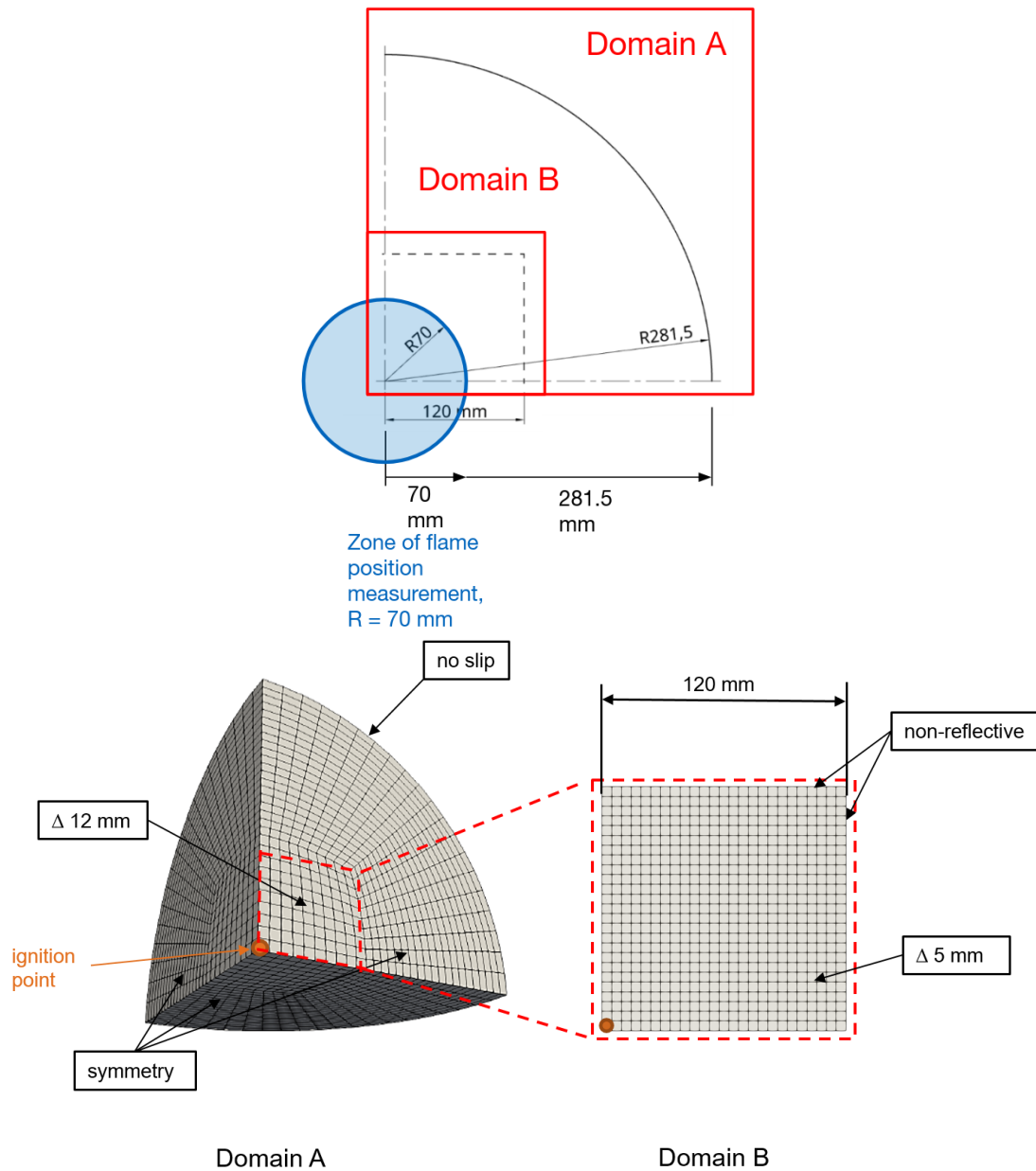


Figure 3.1: A view of the two computational domains and grids used for simulations. In Domain A cell sizes range from 6 to 16 mm, with the central area consisting of uniformly spaced 12 mm cells. Domain B is uniformly discretized by 5 mm cells.

The mixture-specific quantities are given in Table 3.2, while the turbulence quantities and root-mean-square (RMS) velocities u'_i are given in Table 3.1.

3.3 Turbulent flame speed correlation

Closure for the reaction rate in Equation 2.24 requires a model for turbulent wrinkling. In conditions where turbulence dominates the flame topology, the effective flame speed S_{eff} in Equation 2.25 becomes the turbulent flame speed:

$$\Xi = \frac{S_{\text{eff}}}{S_l}, \quad (3.1)$$
$$S_{\text{eff}} = S_t.$$

Turbulent flame speed is commonly calculated based on experimental correlations, with a large number of derived correlations available in the literature (Lipatnikov and Chomiak, 2002). In this work, a correlation by Dinkelacker et al. (2011) is used, which reads

$$S_t = 1 + \frac{0.46}{Le} \text{Re}_t^{0.25} \left(\frac{u'}{S_l} \right)^{0.3} \left(\frac{p}{p_{\text{ref}}} \right)^{0.2}. \quad (3.2)$$

Here, Re_t is the local Reynolds number, u'_i is the fluctuating component of velocity, in RANS framework estimated as

$$u' = \sqrt{\frac{2}{3}k}, \quad (3.3)$$

and Le is the mixture Lewis number.

3.4 Pressure results

The domain representing the whole combustion vessel (Domain A in Figure 3.1) was used for calculating the pressure transients. The CFL criterion (Equation 2.75) was set to one. The number of stages of the SSP Runge–Kutta method was set to $m = 8$, which was chosen to ensure stability during the steep pressure rise that happens in the confined volume of the vessel at a later stage of the experiment. Several trials with a lower CFL, i.e. CFL = 0.1, 0.3 and 0.5, were conducted to confirm the time step independence of the solution.

Figures 3.2, 3.3 and 3.4 show the pressure evolution in comparison with the experiments for $x_{\text{H}_2} = 16\%$, 20%, 28% vol. hydrogen–air mixtures.

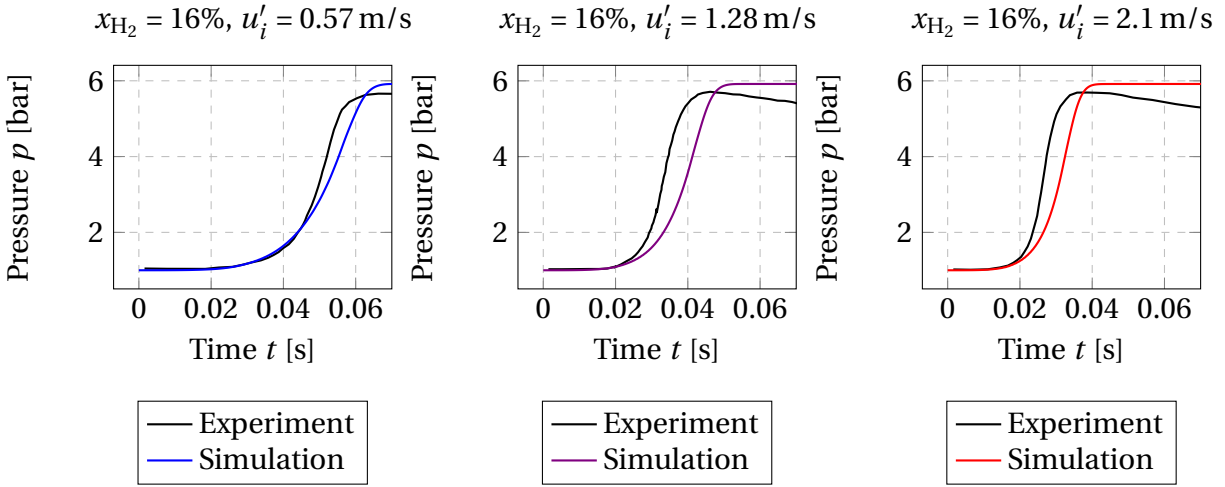


Figure 3.2: Pressure rise in the spherical vessel for $x_{\text{H}_2} = 16\%$.

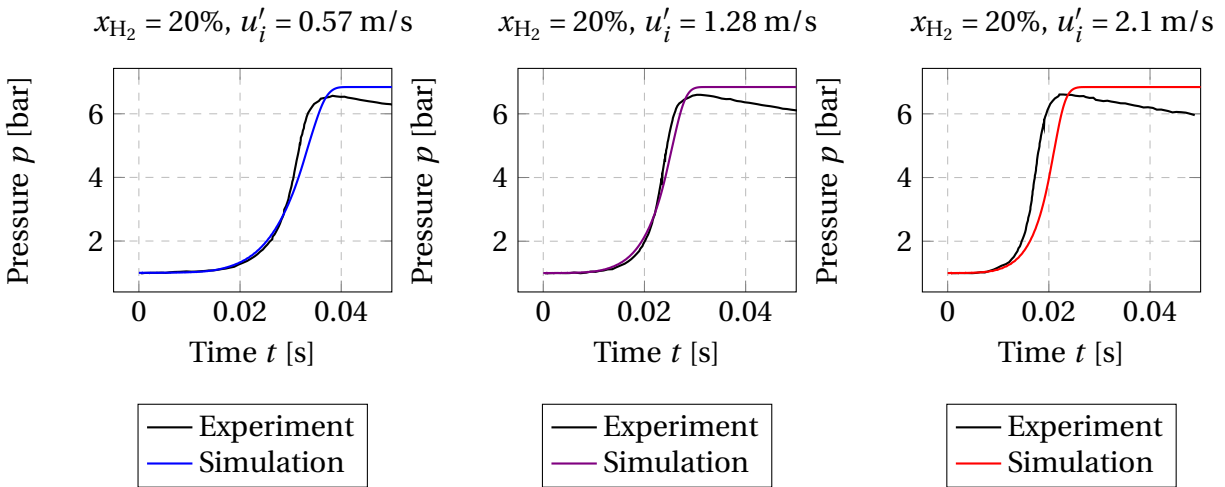


Figure 3.3: Pressure rise in the spherical vessel for $x_{\text{H}_2} = 20\%$.

As expected, the turbulence intensity does not influence the peak value of pressure and the maximum pressure reached in the simulations is the adiabatic isochoric complete combustion pressure (p_{aicc}) for a given mixture. It can be observed, however, that the total volume of gases is combusted in a shorter time due to higher flame speeds reached in conditions of higher turbulence intensity. The pressure peak in the experiments was close to p_{aicc} , but due to heat loss it remained slightly below it. Heat transfer was not modeled in the simulations, which explains the pressure curve remaining at the peak value after complete combustion – in contrast to the experiment where

3.4 Pressure results

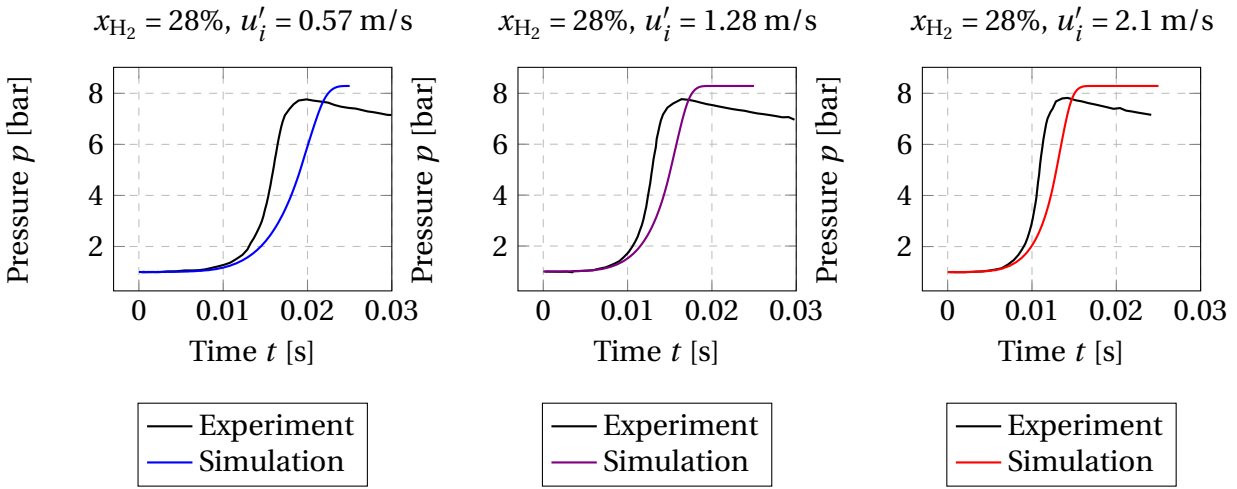


Figure 3.4: Pressure rise in the spherical vessel for $x_{\text{H}_2} = 28\%$.

it starts to drop off at that moment. Mesh sensitivity of the result was tested

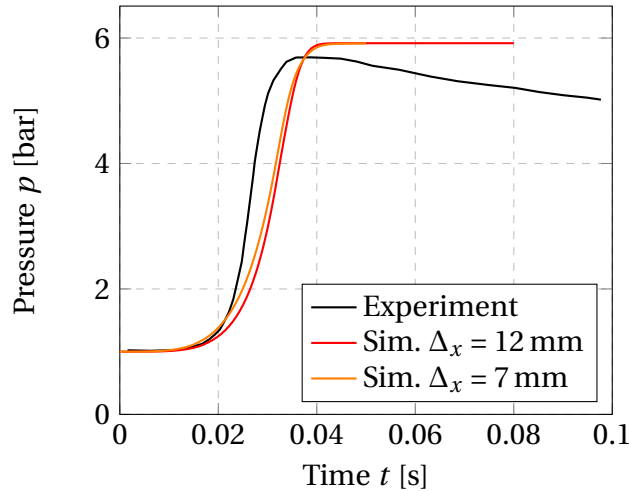


Figure 3.5: Pressure rise in the spherical vessel for $x_{\text{H}_2} = 16\%$ and $u'_i = 2.1 \text{ m/s}$ computed on a 7 mm and a 12 mm structured hexahedral grid.

on a finer grid with 7 mm spacing in the central area – in contrast to 12 mm for the coarser grid. Figure 3.5 shows that the finer grid did not significantly affect the result.

The results of the validation simulations show that the numerical method reproduces the pressure behavior well in the confined volume of the laboratory-scale combustion vessel. The moment when the steep pressure rise begins

corresponds with flame's arrival to the near proximity of the vessel wall. The prediction of its timing depends on accurate modeling of the turbulent flame speed, which will be discussed in the next section.

3.5 Flame position and speed results

The results of flame position and speed were obtained on a reduced domain (Domain B) as described in Section 3.2 where the details of the computational setup can be found. The CFL limit (Equation 2.75) was set to one. The number of stages of the SSP Runge–Kutta method was set to $m = 3$. The flame position is defined in the results as the location at the center of the turbulent flame brush – represented by the value of the progress variable of $b = 0.5$.

The plot of flame radius over time for all four hydrogen–air mixtures ($x_{\text{H}_2} = 16\%$, 20% , 28% vol.) from the experiment can be seen in Figure 3.6. No adjustments of the results in time was made. Numerical results fall mostly within the standard deviation interval of the experimental measurements by Goulier et al. (2017b), with the highest correspondence of the numerical simulation results with the experiments is for the leanest case, $x_{\text{H}_2} = 16\%$ vol.

The turbulent flame displacement speed was obtained by differentiating the simulation results of flame position over time – the same procedure that was used with the experimental data by Goulier et al. (2017b,a). Figure 3.7 shows the flame speed along the radius of the spherical vessel.

Simulation results at all investigated turbulence levels follow the experimental trend more closely for radii between 30 and 50 millimeters (r), while closer to the ignition point ($r \leq 30$ mm) the simulations show lower flame speeds than those in experiments. This observation is more pronounced for mixtures with a higher chemical reactivity characterized by a higher laminar flame speed S_1 and lower laminar flame thickness δ_1 . In cases with $x_{\text{H}_2} = 20\%$ and $x_{\text{H}_2} = 24\%$ a slight overprediction of the flame speed is observed as the flame radius grows. In case of the near-stoichiometric mixture with $x_{\text{H}_2} = 28\%$ and the lean-

3.5 Flame position and speed results

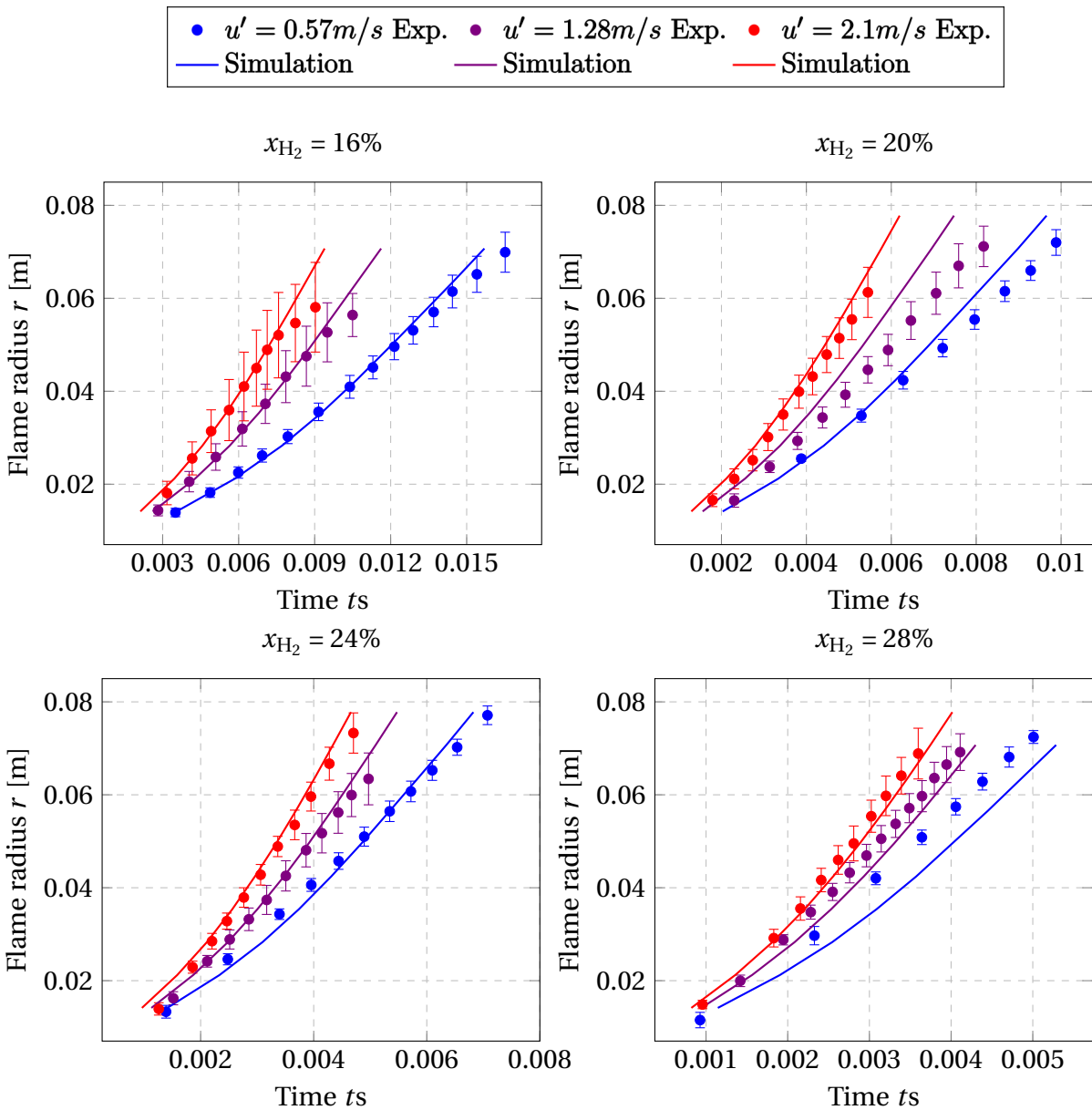


Figure 3.6: Evolution of flame radius r over time in the spherical vessel validation case. The results are computed using Domain B.

est mixture with $x_{\text{H}_2} = 16\%$ the flame speed corresponds more closely to the experimental results and the overprediction is small.

The initial deficit of the flame speed in the simulation results (Figure 3.7) could be explained by the observation that the gradient of the progress variable requires several cells to fully develop in the solution field after ignition. The in-

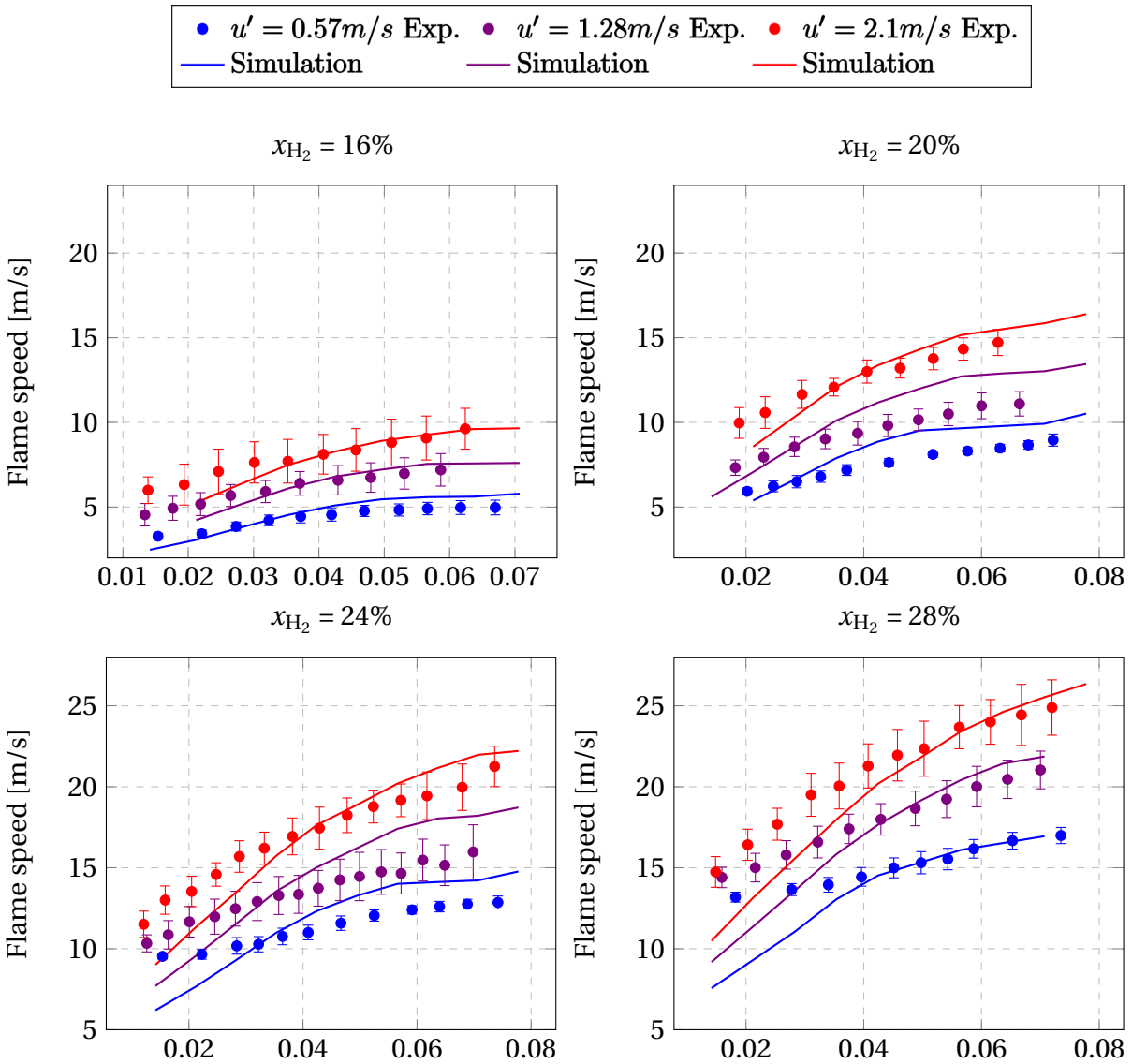


Figure 3.7: Flame displacement speed over the radius r in the spherical vessel validation case. The results are computed using Domain B.

fluence of this effect is potentially significant in short distance close to the ignition point since the gradient of progress variable directly determines the magnitude the burning rate in the Equation 2.24. Another possible source of the observed differences in flame speed results between experiments and simulations close to the ignition point could be the way the mixture is ignited in the experiments and modelled in simulations. Namely, in the experiments, ig-

nitron energy is added to the system which is not the case in simulations where only a conversion of the chemical energy of the fuel is triggered.

3.6 Time integration performance comparison

The relative performance of the time integration methods is presented next. The comparison is made between the first-order forward Euler scheme, the conventional second-order four-stage Runge–Kutta scheme and the second-order m -stage SSP Runge–Kutta scheme which was introduced in Section 2.5.

The simulations were run at the highest stable CFL number (CFL_{\max}) for the given scheme that yielded a result of acceptable accuracy. Furthermore, as described in Section 2.5, in case of the SSP scheme, the m parameter can be increased to achieve the required level of stability for the chosen CFL number. For that reason, a combination of the required m parameter for the achieved CFL_{\max} is reported with the results of the SSP scheme. All presented calculations were completed in parallel, using 4 processors on a desktop PC (AMD Ryzen 7/2700).

Firstly, a performance comparison for simulations of flame propagation and pressure rise on Domain A for 25 ms of simulated time is given in Figure 3.8. Compute times using different methods can be found in Table 3.3. Multiple entries for SSP Runge–Kutta method correspond to different CFL_{\max} numbers and m parameters. The aim was to assess the performance of different schemes at a comparable level of accuracy. However, results in Figure 3.8 show that forward Euler and conventional Runge–Kutta show a delay in the pressure rise compared to the SSP-RK. It persisted regardless of the CFL or mesh fineness. The performance gains shown by the SSP scheme come from a higher CFL_{\max} , i.e. reduction of the number of time steps needed to complete the calculation. The SSP-RK with $m = 14$ and $CFL_{\max} = 2$ computes the result in the shortest CPU time, however the improvement over the $CFL_{\max} = 1$ and $m = 8$ is not dramatic, showing that the benefit of an increased time step approaches its asymptotic limit (Tab. 3.3). The maximum CFL_{\max} for both Euler and the conventional Runge–Kutta schemes had to be severely limited to achieve sta-

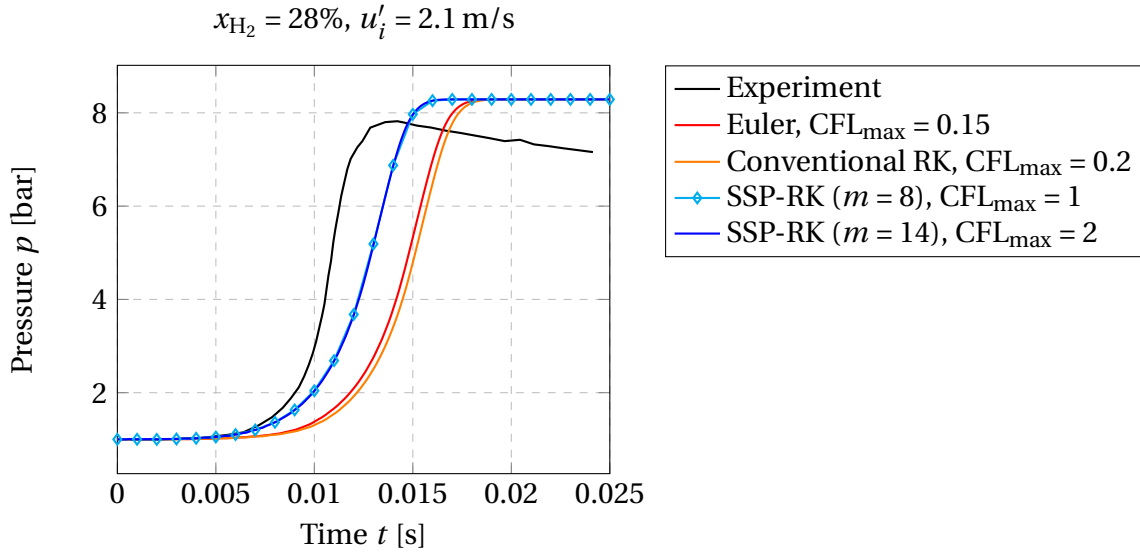


Figure 3.8: Pressure rise at $x_{\text{H}_2} = 28\%$ and high level of turbulence ($u'_i = 2.1 \text{ m/s}$) computed using different time integration methods (Domain A). CPU time comparison is given in Table 3.3.

Table 3.3: Time integration performance for pressure rise simulations (Domain A).

	CFL_{max}	CPU time	Relative time
Euler	0.15	665 s	1.5
Conventional RK	0.2	1324 s	3
SSP-RK ($m = 8$)	1	488 s	1.1
SSP-RK ($m = 14$)	2	442 s	1.0

bility as shown by the values in Table 3.3. Furthermore, the stability limit of the conventional RK scheme is not significantly higher than the one for the simple forward Euler scheme. When limited by a relatively low, stability-bound CFL_{max} in such a way, the conventional four-stage RK takes longer to compute than the forward Euler scheme due to its higher number of stages.

Additionally, the performance of time integration schemes is assessed for simulations of flame propagation using Domain B for 16 ms of simulated time. Figure 3.9 shows the comparison between the analyzed schemes at a compa-

3.6 Time integration performance comparison

able level of accuracy. Table 3.4 lists the required compute time for different methods.

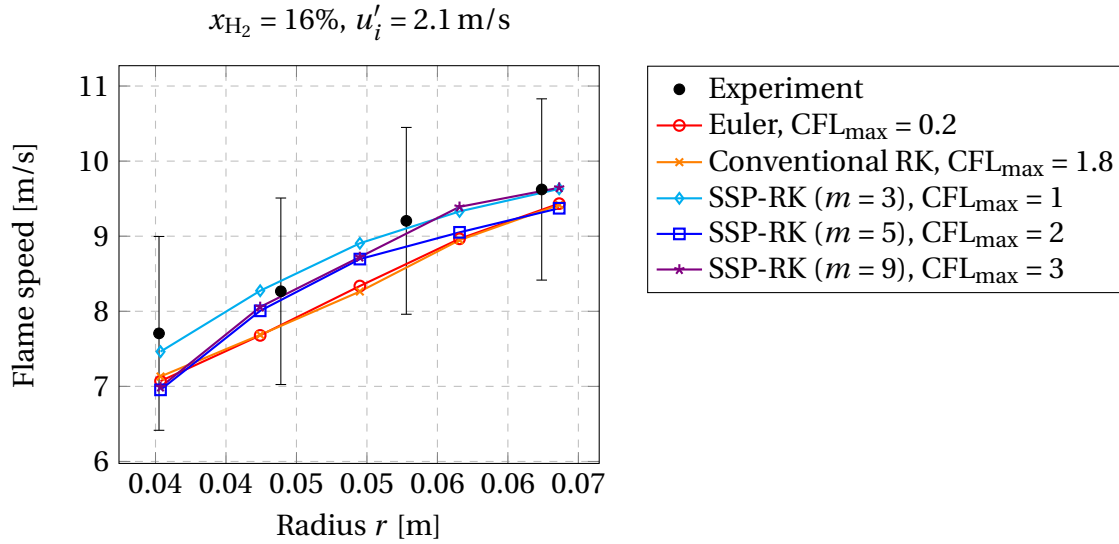


Figure 3.9: Results of turbulent flame speed at $x_{\text{H}_2} = 16\%$ and high level of turbulence ($u'_i = 2.1 \text{ m/s}$) for different time integration methods. Each method is run at the maximum allowable CFL_{\max} needed to achieve comparable level of accuracy. CPU time comparison is given in Table 3.4.

Table 3.4: Time integration performance for flame propagation simulations (Domain B).

	CFL_{\max}	CPU time	Relative time
Euler	0.2	445 s	2.34
Conventional RK	1.8	216 s	1.13
SSP-RK ($m = 3$)	1	241 s	1.27
SSP-RK ($m = 5$)	2	190 s	1.0
SSP-RK ($m = 9$)	3	223 s	1.17

Both Runge–Kutta schemes are able to compute the result in about a half of the CPU time in contrast to the forward Euler scheme. To achieve the same stability and accuracy, the CFL_{\max} of the forward Euler had to be decreased to $\text{CFL}_{\max} = 0.2$. The better performance of the RK schemes comes from the

higher maximum CFL_{\max} , i.e. reducing the number of time steps for the calculation. In case of the SSP scheme, as the CFL_{\max} is increased, the higher m is required. Despite the substantial increase in m at $CFL_{\max} = 2$ and $CFL_{\max} = 3$, the computational efficiency of the SSP method increased overall compared to the baseline forward Euler scheme. However, the highest CFL_{\max} does not result in the highest efficiency and the optimal point is closer to the $CFL_{\max} = 2$. The asymptotic behavior of the performance gain can be observed as in the previous case (Domain A).

While the computational performance of the conventional RK scheme nearly matched the SSP–RK in simulations on Domain B, where pressure did not substantially rise, in case of Domain A simulations, where a steep pressure rise occurs, the limited stability properties of the conventional RK scheme lead to a substantial decrease in computational performance.

The performance comparison presented here shows that the SSP time integration can improve the efficiency of transient simulations by enabling a stable computation in cases where conventional methods are more strongly limited by the maximum achievable CFL condition, e.g. in case of occurrence of steep pressure gradients, which are particularly important in explosion safety analysis.

Part II

Deflagration Modeling in Conditions of Low Turbulence

4 Introduction to the Darrieus–Landau instability

4.1 Outline and motivation

In early stages of accidental gas explosions occurring in various industrial facilities or as a result of a nuclear reactor accidents, the combusted gas mixtures where ignition happens is predominately in quiescent initial state, characterized with negligible gas velocity and equally negligible turbulence intensity. The described conditions can be theoretically labeled as premixed laminar combustion, although their morphology is nonetheless highly wrinkled. The reason for that is the presence of intrinsic flame instabilities, which in such conditions become the main driving mechanism for flame acceleration.

The numerical modeling methodology in the present work is aimed at practical application at scales of interest (e.g. interior of the reactor containment), which due to challenges of numerical simulation of large-scale phenomena (discussed in Chapter 1) requires sub-grid closure models for flame speed.

In Part II of the present work, a scale-adaptive URANS model for flame instability effects on flame propagation by Zivkovic and Sattelmayer (2023) is introduced. The model validation was performed using lean and stoichiometric hydrogen deflagration experiments at medium (~ 1 m) and large (~ 10 m) geometric scales.

Chapter 4 introduces the theoretical background of the DL instability, Chapter 5 presents the derivation of the modeling approach and explains the theoretical limits for its application, while the model validation is presented in Chapter 6.

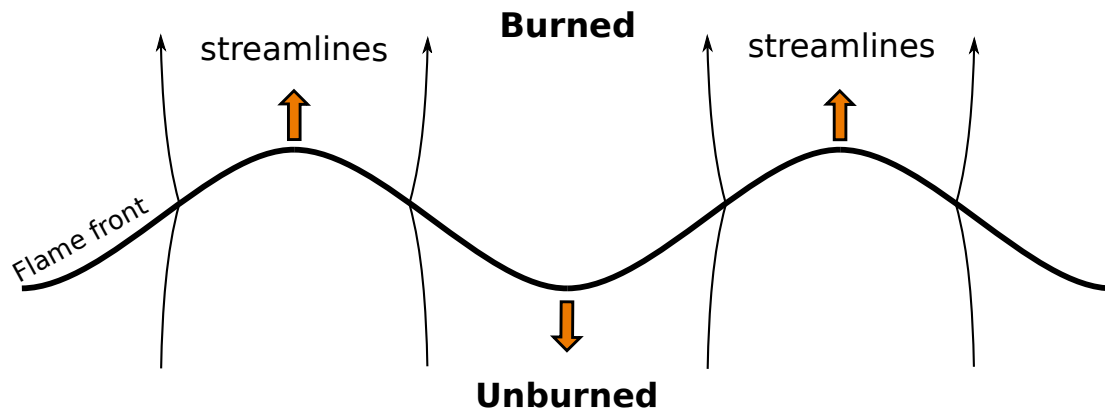


Figure 4.1: A schematic diagram of the Darrieus–Landau (DL) instability at the flame front. Orange arrows show the direction of cusp movement.

4.2 State of the art in Darrieus–Landau instability modeling

Darrieus–Landau (DL) hydrodynamic instability emerges as an effect of gas expansion caused by heat release (Matalon, 2018; Liberman, 2021). Consequently, the DL instability is ubiquitous for premixed combustion, irrespective of the type of fuel. It has been observed for hydrocarbon mixtures (Bradley et al., 2001; Bauwens et al., 2015; Kim et al., 2015b), as well as hydrogen (Kim et al., 2013, 2015b,a; Bauwens et al., 2017) and hydrogen–carbon-monoxide (Jiang et al., 2020) mixtures, where the latter two are of particular importance for nuclear safety. Furthermore, the emergence of flame instability occurs for both lean (Bauwens et al., 2017; Kim et al., 2013, 2015b) and rich (Kim et al., 2013, 2015a) compositions alike. The fundamental mechanism of the DL instability is understood as a self-accelerating feedback loop between a perturbation of the flame front due to gas expansion, which causes an increase in flame surface area (wrinkling), which, in turn, causes a further increase in the reaction rate (Matalon, 2018; Liberman, 2021).

In experiments with unconfined spherical flames, the emergence of DL instability is observed once flame reaches a critical radius r_0 (Bauwens et al., 2017; Sun et al., 2012; Liu et al., 2012), after which the exponential growth in flame radius r continues, a behavior that was first experimentally confirmed in large-scale experiments by Lind (1974) and Gostintsev et al. (1988). A common way of quantifying flame acceleration in experimental studies is to use

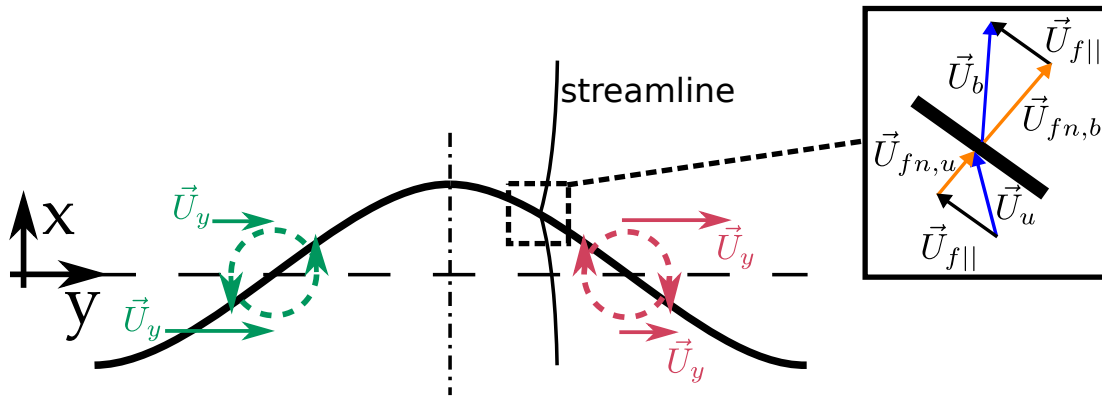


Figure 4.2: A planar, DL-instability-perturbed flame can be understood as a vortex sheet forming due to differences in velocity components in the y direction (Matalon, 2018). The detail shows the velocity diagram at the flame front, corresponding to the location of the discontinuity in the streamline shape.

a power-law function of a global flame radius r . First such correlations were introduced in Gostintsev et al. (1988). However, in nuclear safety applications, more complex geometry is present, often with multiple interconnected compartments, narrow ducts or gaps (Gupta and Langer, 2019). A spherical shape of the flame can no longer be assumed at all stages of propagation, although individual compartments can be large enough that the flame initially propagates (hemi-)spherically for several meters before reaching an obstacle or a change in cross-section (Gupta and Langer, 2019). For this reason, correlations based solely on global flame radius have a very limited applicability, thus a more general mathematical description is preferred from a numerical approach aimed towards industry-scale applications. With this motivation in mind, the modeling approach developed in the present work is not based on the global radius of the flame front.

Numerical and theoretical models of the DL instability have been in development for the past decades, starting from reduced-, or simplified equation modeling in 1D and 2D (Sivashinsky, 1977; Frankel and Sivashinsky, 1982; Matalon and Matkowsky, 1982). Such models have led to improved basic understanding of the phenomenon, explored the stability limits of the perturbed flame fronts, attempted to quantify the self-acceleration and uncovered the

fractal nature of the DL instability (Sivashinsky, 1977; Frankel and Sivashinsky, 1982; Matalon and Matkowsky, 1982; Blinnikov and Sasorov, 1996; Mukaiyama et al., 2013; Creta et al., 2020).

Resolving the DL instability by directly solving Navier–Stokes equations in a DNS is particularly challenging since the DL instability emerges at length scales orders of magnitude larger than the laminar flame thickness δ_1 (Bychkov and Liberman, 2000). Such scales are still beyond the capabilities of the state-of-the-art DNS on large compute clusters, due to computational cost. The problem can be worsened further if detailed chemical mechanisms are to be used. Consequently, highly resolved simulations of DL instability are still mostly confined to 2D. Yu et al. (2015) studied the DL instability effects on planar flames at increasing domain sizes up to $L = 1600 \delta_1$ using highly resolved 2D numerical simulations. The study represents the largest scales simulated by a highly-resolved numerical study that could be found in the literature, although planar flames under the influence of the DL instability were analyzed in 2D by Creta et al. (2020), Berger et al. (2023) and many others. Simultaneous effects of Thermal–diffusive (TD) and the DL instability in the planar 2D setup were investigated by Creta et al. (2020), Berger et al. (2019) and Berger et al. (2023). Apart from planar flames, a cylindrical flame was investigated as well. Studies in 2D were published by Liberman et al. (2004), Altantzis et al. (2013) and Altantzis et al. (2015), and in Three-dimensional (3D) by Liberman et al. (2004) and Altantzis et al. (2015), where the influence of dimensionality on fractal excess and propagation speed was established. Influence of the thermodynamic state on DL instability development was explored in studies by Altantzis et al. (2011) for high pressure, and by Berger et al. (2022a) and Berger et al. (2022b) for various initial temperatures and pressures.

With highly resolved numerical studies being confined to very small-scale flames, industrial applications rely on a suitable sub-grid closure. A LES sub-grid model for the effects of the DL instability on weakly turbulent flames was reported in Keppeler and Pfitzner (2015). It is based on data from highly resolved 2D simulations of planar flames and validated for a Bunsen burner configuration. Lapenna et al. (2021) also used highly resolved 2D simulations of planar flames simultaneously perturbed by DL and TD instabilities and de-

rived a scaling law for the effective (wrinkled) flame speed as a function of the number of unstable wavelengths $n_c = L / \lambda_{textc}$, within the largest scale constraining flame growth. In an LES Subgrid-scale (SGS) closure, the largest scale could be defined as filter width. An a-priori analysis of the derived sub-grid scaling is given by Lapenna et al. (2021), however, implementation and a-posteriori evaluation of the LES model was left for future work.

A demand for efficient explosion modeling in the domain of various safety applications compelled the development of a number of RANS or coarse LES approaches, e.g. by Molkov et al. (2006b) and Velikorodny et al. (2015), that largely approached the problem of sub-grid closure by applying various scaling laws derived for turbulent flames. Use of turbulent scaling laws would often be justified by the assumption of flame-generated turbulence as the driving mechanism of self-acceleration in DL-perturbed flames (sometimes called "self-turbulization"). However, recent results of DNS work by Lipatnikov et al. (2018) and Lipatnikov et al. (2019) show that flame-generated vortex structures can not be assumed to always increase the flame surface area (wrinkling), as they demonstrate that flame-generated vorticity can in certain conditions reduce the flame surface area. Furthermore, recent experimental work by Liu et al. (2021) looked to settle the question of flame-generated turbulence in spherically expanding flames by detailed measurements of the flow field. The study found significant velocity fluctuations in close proximity to the flame in a fully developed self-similar stage of propagation. However, the energy spectra of the tangential velocity component showed a power-law dependence directly related to the fractal dimension of the DL-instability-wrinkled flame, and not to the Kolmogorov turbulence spectra that could be associated with a process of turbulence generation (Liu et al., 2021). These recent developments strongly suggest that a sub-grid flame speed scaling law developed specifically to deal with the effects of the Darrieus–Landau instability is required. A sub-grid model for such effects which can be used for large-scale industrial applications in the safety domain, which is also free of flame shape assumptions and prescribed global geometric parameters – such as flame radius – was, to the best of author’s knowledge, first proposed in Zivkovic and Sattelmayer (2023).

5 Model derivation

5.1 Scale-adaptive, fractal-based model for Darrieus–Landau instability effects

Flames driven by the DL instability appear in the high Damköhler number region in the Borghi diagram (Figure 5.5). Following that, the flame can be considered a thin front and the effective burning rate can be expressed as proportional to the surface area density of the flame front. A flame wrinkling factor (Ξ) is then defined as the ratio of the effective (wrinkled) flame surface A_{eff} and a smooth flame surface A_l (Figure 2.1), which forms the basis of many combustion modeling approaches (Equation 2.25), although it is strictly valid only for unity Lewis numbers (Ozel-Erol et al., 2021). Given that the laminar flame speed S_l in Equation 2.25 depends only on unburned mixture properties and its thermodynamic state, it becomes clear that by modeling the flame wrinkling Ξ , it would be possible to arrive at the effective flame speed $S_{\text{eff}} = \Xi S_l$. Fractal theory provides a general way of mathematically describing wrinkled surfaces based on the assumption of self-similarity. It has been applied to numerous naturally occurring phenomena that are characterized by geometric complexity (Mandelbrot, 1983). Gouldin (1987) applied the fractal theory to express the area ratio of a wrinkled flame front as

$$\Xi = \frac{A_i}{A_o} = \left(\frac{\epsilon_o}{\epsilon_i} \right)^\beta \quad (5.1)$$

where ϵ_i and ϵ_o are the inner and the outer cut-off scales and the exponent β is fractal excess, defined as $\beta = D_3 - 2$, where D_3 is the fractal dimension of a 3D surface, which is indicated by the subscript. Figure 5.1 shows a qualitative plot of the theoretical relationship between quantities defining a fractal surface from Equation 5.1.

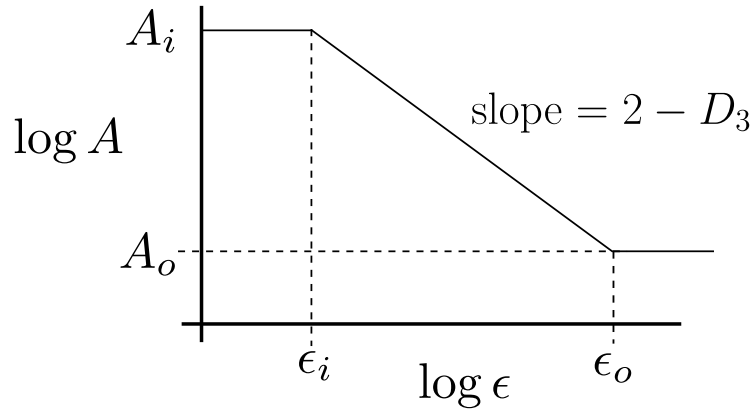


Figure 5.1: Fractal growth of the area of a self-similar surface. In an interval between an inner (ϵ_i) and an outer (ϵ_o) cut-off scale, the growth of surface area is described by a constant slope $2 - D_3$.

Although work by Gouldin (1987) developed a model for turbulent flames, the mathematical description provided by Equation 5.1 is based solely on fractal geometry of a self-similar surface, and is, as such, applied in the present work as basis for modeling the DL instability in absence of turbulence. The fractal nature of the DL instability was investigated in a number of experiments and highly-resolved simulations of unconfined flames. In such a configuration, the flame expands spherically, with its radial growth behavior expressed with

$$r \sim t^\alpha. \quad (5.2)$$

If a flame is in a self-similar (fractal) growth regime, the growth exponent α is constant and positive. The growth exponent α can be determined from the slope of the double logarithmic plot of the radius r over time t as was done in work by Kim et al. (2015b) or Mukaiyama et al. (2013), determining the fractal excess β , since

$$\beta = \frac{\alpha - 1}{\alpha}. \quad (5.3)$$

Experiments by Kim et al. (2015b,a); Bauwens et al. (2017); Kim et al. (2018); Gostintsev et al. (1988) have found constant and positive growth exponents for hydrogen–air flames. Moreover, two-dimensional simulations of planar flames (Blinnikov and Sasorov, 1996; Mukaiyama et al., 2013; Liberman et al., 2004; Yu et al., 2015) confirmed the fractal nature of the DL instability for unconfined flames and established a dependence of the fractal excess on expan-

sion ratio γ , which is defined by

$$\gamma = \frac{\rho_u - \rho_b}{\rho_u}. \quad (5.4)$$

Well-resolved 2D simulations by Mukaiyama et al. (2013) reported a 3D fractal dimension of $D_3 \approx 2.33$, which amounts to a fractal excess of $\beta = D_3 - 2 = 0.33$, where the three-dimensional D_3 was estimated from the 2D result to be by a factor of two greater than the 2D fractal dimension, similar to Liberman et al. (2004). However, experiments by Kim et al. (2015b), Kim et al. (2015a), Bauwens et al. (2017) and Kim et al. (2018) demonstrate that, for a realistic γ , e.g. for hydrogen flames $\gamma \in [0.7, 0.85]$, the fractal excess is generally lower, in the range $\beta \in [0.24, 0.33]$ (Kim et al., 2020). Since the expansion coefficient γ does not vary dramatically with equivalence ratio for most gases, large-scale experiments dating back to Gostintsev et al. (1988) express the fractal excess as a constant for a given type of fuel (Kim et al., 2015a; Bauwens et al., 2017).

Adopting the fractal description provided by Equation 5.1 at its base, a novel modeling approach was developed by Zivkovic and Sattelmayer (2023) for the Darrieus–Landau (DL) instability effects on flame wrinkling. One of the characteristics of the DL instability is that flame cusps caused by it can grow very large, as it was observed in an experiment reported in Schneider and Pförtner (1983). A coarse computational grid will therefore resolve a portion of the largest flame structures, while the closure model is necessary for the unresolved flame scales.

The driving mechanism of the DL instability is gas expansion due to heat release. It is therefore assumed here that the scale of resolved hydrodynamic structures (perturbations) is proportional to the scale of the flame front structures. An assumption that the scale of flame wrinkling is proportional to the scale of hydrodynamic perturbations is in line with the understanding of a DL-wrinkled flame as a vortex sheet (Matalon, 2018). An estimate of the resolved hydrodynamic structures is given by the flame von Kármán length scale $L_{vK,f}$

$$L_{vK,f} = \kappa_{vK} \left| \frac{\frac{\partial f_i}{\partial x_j}}{\frac{\partial^2 f_l}{\partial x_k^2}} \right| \quad (5.5)$$

where $\kappa_{\text{vK}} = 0.41$ is the von Kármán constant, and f_i is the gas velocity in the flame normal direction, defined as

$$f_i = (n_j u_j) n_i, \quad (5.6)$$

where u_j is the gas velocity and

$$n_i = \frac{\frac{\partial b}{\partial x_i}}{\left| \frac{\partial b}{\partial x_i} \right|} \quad (5.7)$$

is the unit normal vector of the flame surface and b is the reaction regress variable. The definition of an outer cut-off scale is based on the observation that, for the flames wrinkled by the DL instability, the hydrodynamic strain caused by thermal expansion is directly evidenced by the velocity gradient field so that $\epsilon_o \propto L_{\text{vK},f}$. A three-dimensional generalization of a von Kármán length scale, albeit in turbulent inert flow, thus with no relation to a flame front, is used for resolved turbulent length scale estimation in a URANS turbulence model by Menter and Egorov (2010) named k - ω SST-SAS.

Given the assumption that ϵ_o is proportional to the flame von Kármán length scale $L_{\text{vK},f}$ the following can be written:

$$\epsilon_o = C_o L_{\text{vK},f} \quad (5.8)$$

where C_o is an unknown scalar proportionality constant.

The inner cut-off scale of the DL instability is a multiple of the laminar flame thickness, dependent on the expansion coefficient, where for realistic expansion coefficients ($\Theta \in [5, 10]$) it becomes $\epsilon_i \approx 20\delta_l$ (Bychkov and Liberman, 2000). Assuming a constant proportionality factor between the two, we write the inner cut-off length scale as

$$\epsilon_i = C_i \delta_l = C_i \frac{\lambda_u}{\rho_u c_{p,u} S_l} \quad (5.9)$$

where another unknown scalar proportionality constant C_i appears between the inner cut-off scale the laminar lame thickness.

With that and using the definition provided by Equation 2.25, the Equation 5.1 becomes

$$\Xi_{\text{DL}} = \left(\frac{C_o L_{\text{vK},f}}{C_i \delta_1} \right)^\beta = \left(C_{\text{DL}} \frac{L_{\text{vK},f}}{\delta_1} \right)^\beta \quad (5.10)$$

where the two unknown constants C_o and C_i are combined into a single one, C_{DL} . The value of the constant was determined empirically as $C_{\text{DL}} = 0.33$ using a canonical case of an unconfined, near-stoichiometric hydrogen deflagration presented in detail in Section 6.2. The value of the constant C_{DL} was subsequently kept for all further cases and configurations (Section 6.2 - 6.4). For the fractal excess β , an experimentally derived value for hydrogen–air mixtures of $\beta = 0.243$ is applied according to Bauwens et al. (2017). Here assumed self-similarity of the flame surface and the choice of the fractal excess are discussed in further detail in Section 5.4.

5.2 Small-scale effects on effective flame wrinkling

The TD instability, local flame curvature and pressure can act in addition to the Darrieus–Landau instability and influence the effective flame speed. These effects take place on smallest scales of the flame front and a RANS modeling approach is not able to directly resolve them (Keppeler and Pfitzner, 2015; Lapenna et al., 2021).

For lean hydrogen–air compositions characterized by less-than-unity Lewis numbers ($Le < 1$), differential heat and mass diffusion rates are present in the reaction zone (molecular scale), the result of which is emergence of the TD instability which induces small-scale flame wrinkling. The dependence of wrinkling on the TD instability is modeled by

$$\Xi_{\text{TD}} = Le_{\text{eff}}^{-1}. \quad (5.11)$$

Equation 5.11 appears in a number of experimental and highly resolved numerical results available in literature. A DNS study by Chakraborty and Cant (2011) reported that the correlation for surface-averaged local flame displacement speed defined as $\overline{(\rho S_d)_s} \approx \rho_u S_1$ improves significantly for non-unity

Lewis numbers when it includes the $1/Le$ scaling, becoming

$$\overline{\rho S_d} \approx \frac{\rho_u S_l}{Le} \quad (5.12)$$

(Chakraborty and Cant, 2011; Klein et al., 2016). Moreover, an experimentally-determined correction factor equal to $1/Le$ was proposed in Muppala et al. (2005) for non-unity Lewis numbers. The factor was included in an algebraic RANS approach for modeling turbulent flame speed and applied at $Le > 1$. Later, in Dinkelacker et al. (2011), the factor was successfully applied at $Le < 1$, including fuels containing hydrogen. A Lewis number correlation of the flame speed was experimentally investigated in Katzy et al. (2017b) for lean hydrogen–air mixtures and $\Xi_{TD} = Le_{\text{eff}}^{-0.9}$ was arrived at, which agrees well with the factor $1/Le$.

The effective Lewis number Le_{eff} in Equation 5.11 follows from Bechtold and Matalon (2001) where it was derived as a weighted average of individual Lewis numbers of reactants such that

$$Le_{\text{eff}} = 1 + \frac{(Le_E - 1) + (Le_D - 1) C_{Ze}}{1 + C_{Ze}} \quad (5.13)$$

where Le_E is the Lewis number of the excessive species, Le_D is the Lewis number of the deficient species, the factor C_{Ze} is defined as $C_{Ze} = 1 + Ze(\Phi - 1)$ and $Ze = E(T_a - T_u) / R_0 T_a^2$ is the Zeldovich number, with E being the global activation energy of the chemical reaction, T_a and T_u are adiabatic and unburned temperature, and R_0 is the gas constant.

The second small-scale effect considered here is due to flame stretch, which can locally increase the flame speed above the laminar flame speed S_l for fuels with negative Markstein lengths such as lean hydrogen (Figure 5.2). This effect was investigated by Katzy (2021) (and references therein) with an aim of empirically quantifying its influence on the effective flame speed. Furthermore, Chakraborty and Cant (2011) reported that $\overline{\rho S_d}$ displays a curvature dependence that is not captured by the Le number correction introduced earlier in Equation 5.12. A correction factor F_c for the curvature effects on laminar flame speed S_l proposed by Katzy (2021) is

$$F_c = (1 + \mathcal{L}\kappa_c)^{-1} \quad (5.14)$$

where $\kappa_c = \frac{\pi}{2}\kappa_{c, \text{ref}}$ is the small-scale local geometric curvature and \mathcal{L} is the Markstein length. In the present work, \mathcal{L} was approximated by the polynomial derived from data of numerous experimental investigations (Aung et al., 1997; Dowdy et al., 1991; Lamoureaux et al., 2003; Taylor, 1991):

$$\mathcal{L} = -0.0002\Phi^3 - 0.00031\Phi^2 + 0.0013\Phi - 0.000752, \quad (5.15)$$

where Φ is the hydrogen–air equivalence ratio. Figure. 5.2 plots the experimental data against the polynomial approximation. The value of $\kappa_{c, \text{ref}} = 500 \text{ m}^{-1}$ originates from OH–PLIF experiments and highly resolved two-dimensional simulations of propagating flames reported by Katzy (2021).

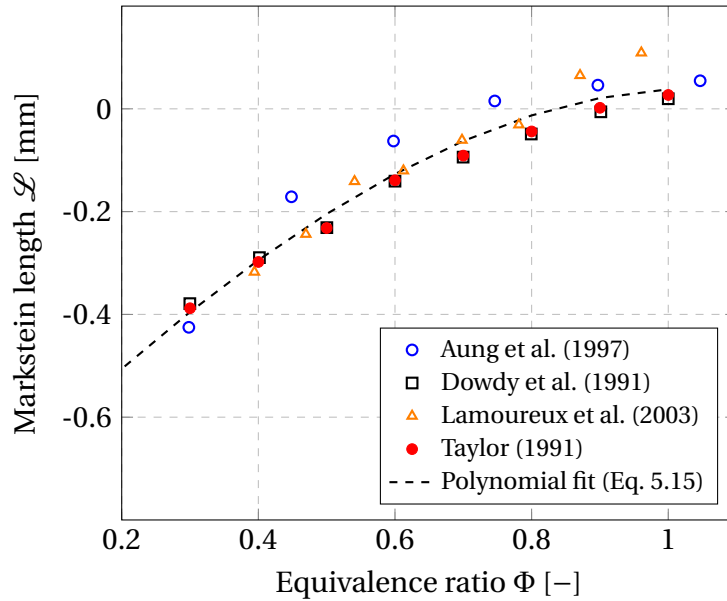


Figure 5.2: Lean hydrogen–air flames are characterized by a negative Markstein length \mathcal{L} .

Finally, the correlation for the effect of pressure on flame wrinkling reported by Muppala et al. (2005) is used, where

$$F_p = \left(\frac{p}{p_{\text{ref}}} \right)^\psi, \quad (5.16)$$

with $p_{\text{ref}} = 1 \text{ bar}$ and $\psi = 0.2$. Equation 5.16 was derived using experimental data for hydrocarbons in range from 1 to 10 bar (Muppala et al., 2005). It was later confirmed valid for mixtures containing hydrogen in Dinkelacker et al.

(2011). The exponent $\psi = 0.2$ is in good agreement with experimental data reported by Katzy et al. (2017a) where, for hydrogen–air mixtures, $\psi = 0.18$ was quantified, albeit the experiments were conducted up to the pressure of 2 bar.

5.3 Total effective flame wrinkling

The total effective flame wrinkling factor, including above-described individual contributions is given by

$$\Xi = \Xi_{\text{DL}} \cdot \Xi_{\text{TD}} \cdot F_c \cdot F_p. \quad (5.17)$$

The wrinkling factor is calculated by an algebraic function that can be easily implemented in a RANS CFD framework. More details about the implementation are given in Section 6.1.

5.4 Model assumptions and validity limits

Assumptions and simplifications that were applied in deriving the model (Equation 5.17) are discussed in the following section, namely

1. assumption of constant fractal dimension,
2. assumption of superimposing small-scale and large-scale effects,
3. assumption of ubiquity of flame instability,
4. assumption of low turbulence intensity.

Assumption of a constant fractal dimension

Variations in the growth exponent α (and by extension in the fractal excess β due to Equation 5.3) were investigated by Kim et al. (2015b) for unconfined

hydrogen, methane and propane deflagrations in two cubic enclosures of 1 m^3 and 27 m^3 in volume. In the experiment, the flame surface was initially smooth in all cases, due to stabilization by stretch. In the second stage, after the initial perturbation of the flame front, a self-acceleration with a growing α could be observed. In the third stage, a self-similar (fractal) regime, characterized by a constant α emerged (Kim et al., 2015b). Small-scale experiments by Cai et al. (2020) confirmed the rising growth exponent in the second stage. However, the setup was not large enough to reach the self-similar propagation (third stage).

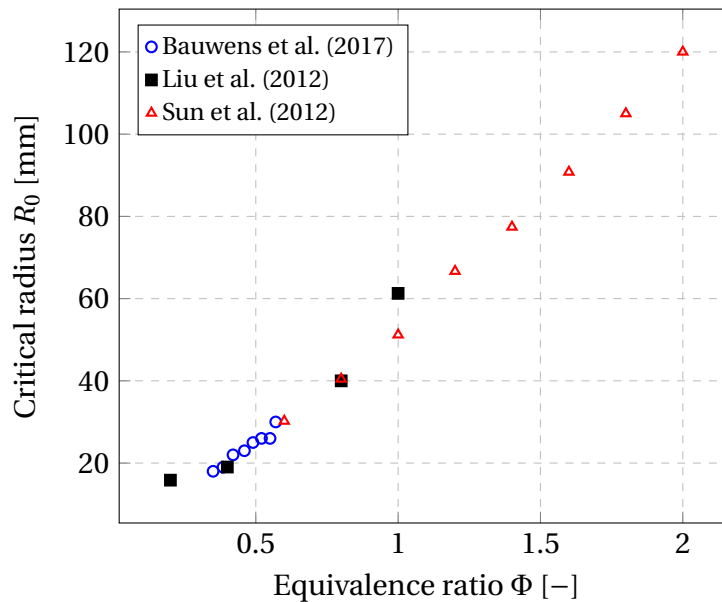


Figure 5.3: Lean hydrogen–air flames are characterized by low critical radii for the onset of cellular instabilities. ($R_{\text{crit}} \approx 10\text{--}50 \text{ mm}$)

An experimental study in a considerably larger enclosure with 64 m^3 in volume by Bauwens et al. (2017) measured a constant growth exponent α , while the distinct stages of growth exponent variation were not observed. The study was carried out with lean hydrogen–air flames ($\Phi \in [0.33, 0.57]$). The observation of a constant growth exponent was consistent with a previous study by Bauwens et al. (2015) with mixtures characterized by negative Markstein lengths. It is likely that in a larger experiment, the initial transient stages could not be detected due to diminishing critical radii for the onset of the instability with the decrease in the Markstein length \mathcal{L} (low Markstein length corresponds to low equivalence ratio Φ in Figure 5.3). This finding corresponds

with the work of Kim et al. (2015a) who derived an empirical flame radius correlation based on a constant growth exponent which agreed well with the large scale experiments by Kim et al. (2015b), Kim et al. (2015a) and Schneider and Pförtner (1983). Moreover, Molkov et al. (2006b) successfully applied a constant fractal dimension of $D_3 = 2.22$, corresponding to fractal excess of $\beta = D_3 - 2 = 0.22$, to large-scale LES simulations.

A constant fractal excess is adopted in the present work given that intended explosion safety applications are concerned with large-scale volumes and any initial fluctuations of growth exponent α can be neglected.

Assumption of superimposing small-scale and large-scale effects

An implicit assumption of superimposing effects of the DL instability effects modeled in Section 5.1 and small-scale effects modeled in Section 5.2 is made in the formulation of the total wrinkling model in Equation 5.17.

The assumption is rooted in the disparate scales of the respective effects, where the DL instability is shown to only emerge in large-enough domains that allow for flame fronts that are orders of magnitude longer than the laminar flame thickness δ_1 (Bychkov and Liberman, 2000).

In contrast, the TD instability is driven by the difference in the thermal and molecular diffusion, which can act to either inhibit or enhance flame surface perturbations (Matalon, 2018). Different natures of the DL instability and the TD instability have been studied by Mukaiyama et al. (2013), where, in addition to the disparity in the length scales between the two instabilities, it was shown that, unlike the DL instability, the TD instability does not exhibit a fractal structure (Mukaiyama et al., 2013).

For three-dimensional unconfined flames, the quantitative effect of TD instability on the flame speed can be seen in the expression

$$S_{\text{eff}} = \left(\frac{R}{R_0} \right)^\beta, \quad (5.18)$$

as R_0 falls severely with the decrease in equivalence ratio and Markstein number (Figures 5.2 and 5.3) (Bauwens et al., 2015, 2017; Gostintsev et al., 1988). Under those conditions, an earlier onset of flame front instability (lower R_0) seems to be initiated by the small-scale wrinkling by the TD instability.

The interaction between the two instabilities has been in focus of numerous studies. Creta et al. (2020) used both Sivashinsky equation modeling and highly resolved 2D Navier–Stokes-based simulations to show that a combination of a destabilizing thermo-diffusive effect and thermal expansion associated with DL instability together produce higher increase in flame surface area density and a higher effective flame speed compared to each of the mentioned effects alone. Flame speed enhancement was shown to be a product of the TD (smaller wavelength) wrinkles being topologically superimposed to DL wrinkles with larger wavelengths (Creta et al., 2020).

Highly resolved simulations of 2D planar flames by (Berger et al., 2019; Creta et al., 2020; Berger et al., 2023) in conditions when both TD and DL are present, show an emergence of finger-like flame structures, which possess a characteristic length distinct from flame cusps formed by solely DL instability. Results found a limit to the size of the flame fingers that was independent of the size of the domain, and a self-similarity regime was not reached for such flames. The 2D planar simulations correspond well to experiments in a Hele-Shaw cell – an experimental setup where a flame propagates in a thin gap between two planar plates – where flame finger topology emerges as well (Fernández-Galisteo et al., 2018; Veiga-López et al., 2019; Gu et al., 2021). Experiments in a Hele-Shaw cell with very lean hydrogen–air flames and varying height of the channel (gap) by Veiga-López et al. (2019) outlined the limits of different morphological regimes, where flame fingers in particular appeared only with sufficiently small gap heights. Experiments by Gu et al. (2021) in similar conditions demonstrated the dependence of the asymptotic flame speed on the gap height as well. Altantzis et al. (2015) numerically investigated circular 2D flames in well-resolved simulations and found finger-like shapes, albeit less elongated in the flame-normal direction. In circular domains, the wavelength grows with the expanding flame, unlike in the planar fronts (Altantzis et al., 2015). A comparison between 3D cylindrical and 2D circular flames was made

by Altantzis et al. (2013) where in the former case the pulsating behavior of the flame motion was more pronounced, resulting in intermittent troughs and crests. A pulsating flame regime was also observed in experiments by Veiga-López et al. (2019) for increased gap heights. In contrast to flames in thin gaps, fully unconfined flame propagation experiments where the flame develops freely in all three dimensions and with a sufficiently large unobstructed volume (Kim et al., 2015b; Bauwens et al., 2015, 2017) show emergence of three-dimensional cellular flame shapes, accompanied by self-similarity measured by a constant fractal excess. This was also observed for cases with negative Markstein numbers, i.e. in conditions where the TD instability appears alongside the DL instability (Kim et al., 2015b; Bauwens et al., 2015, 2017). Mentioned numerical and experimental research shows an important influence of the confinement on the morphological development of instability-perturbed flame fronts. This, in turn, suggests that a universal scaling law for 3D flames can not be directly derived from highly resolved simulation data of 2D flames. Due to still lacking computational resources of the present day, there are no DNS (3D) studies sufficiently large in geometric scale, which could be compared to even small-scale experimental setups (comparable to e.g. Cai et al. (2020), $R \sim 100$ mm). Details of flame topology of unconfined 3D flames in cases where both TD and DL instabilities are present and their complex and nonlinear interaction remains an open question in research.

Despite its simplicity, the model for total effective flame wrinkling given in 5.1 keeps a conceptual view of a flame simultaneously perturbed by DL instability and small-scale effects as a multi-scale phenomenon (Matalon, 2018), where, in Equation 5.10, unresolved scales of the DL perturbed flame are closed and in Equation 5.17 the small-scale effects are applied in separation (assumed that small-scale effects are superimposed to the DL-wrinkled flame front).

Assumption of ubiquity of flame instability at large scales

The model given by Equation 5.17 implicitly assumes an intrinsically unstable flame from the beginning of the flame propagation. Linear stability theory (Matalon, 2018; Liberman, 2021) was not directly used in derivation of the

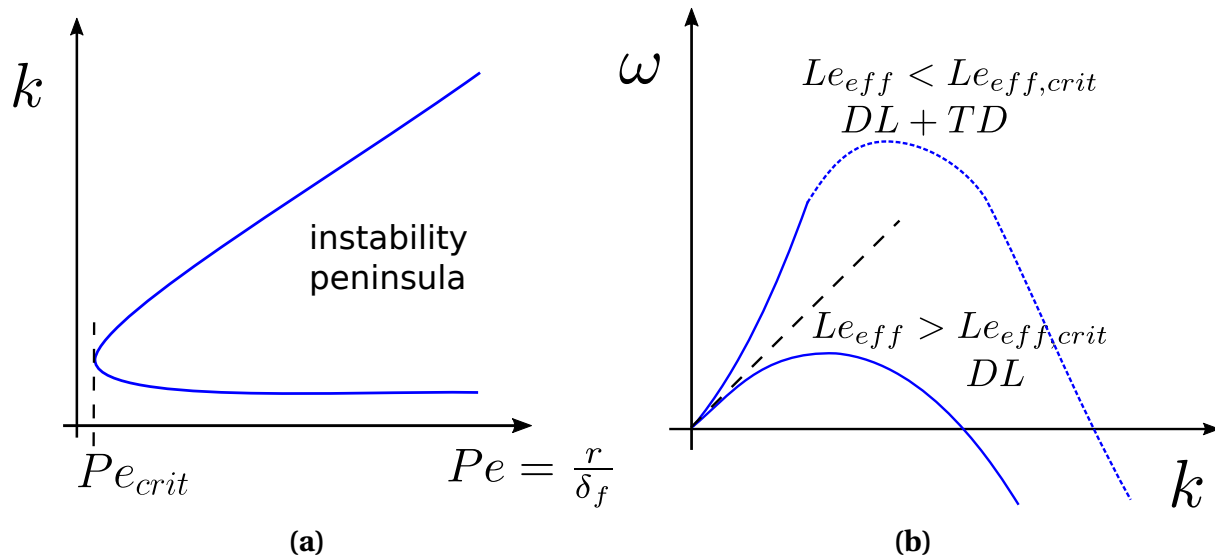


Figure 5.4: Qualitative depiction of the flame instability limits derived from the linear stability theory (Lieberman, 2021; Matalon, 2018).

model equations, but it can be used to explore the validity limits for various conditions. The assumption of an unstable flame in case of lean hydrogen–air mixtures is not a difficult one to make since the critical radius for the onset of cellular instabilities (Figure 5.3) lies within the radius of ~ 50 mm, a distance that can be assumed negligible for intended industrial-scale applications.

Assumption of low turbulence intensity

Validity of the model (Equation 5.10) is limited to the regime of low turbulence. As turbulence intensity increases, turbulent eddies start to dominantly influence the flame front structure, while effects of the DL instability gradually weaken until they vanish completely in highly turbulent flames (Lipatnikov and Chomiak, 2005; Matalon, 2018). Work by Chaudhuri et al. (2011) suggested a theoretical limit to the influence of the DL instability for thermodynamically stable flames ($Le \geq 1$), which approximately corresponds to the area below the red line in the modified Borghi diagram in Figure 5.5. Highly-resolved 2D simulations have been applied to study the limiting interaction between turbulence and the DL instability in works by Creta and Matalon

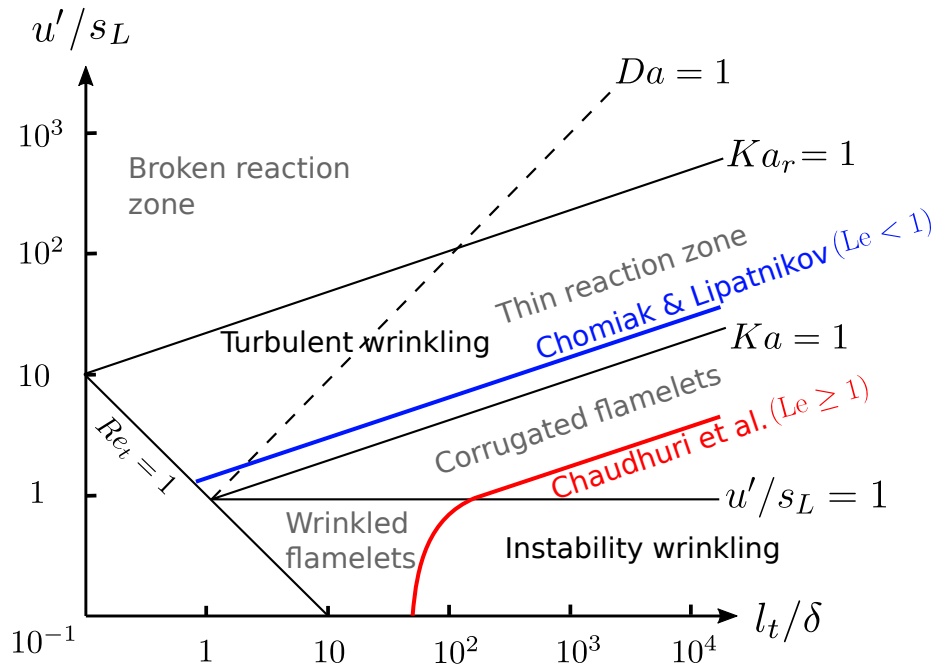


Figure 5.5: DL instability region in the Borghi diagram lies for $Le \geq 1$ below the red line (Chaudhuri et al., 2011) (large scales and low turbulence intensities). Chomiak and Lipatnikov (2023) (blue line) suggest the area of instability effect (TD and DL) to be below $Ka \approx O(10)$.

(2011), Creta et al. (2011), Lapenna et al. (2019) and many others. Recently, Chomiak and Lipatnikov (2023) extended the theoretical criteria proposed by Chakraborty and Cant (2011) to thermo-diffusively unstable ($Le < 1$) flames characteristic for lean H_2 -air mixtures. According to the criterion suggested by Chomiak and Lipatnikov (2023), the synergistic effect of the TD instability in addition to the DL hydrodynamic instability, can only drive the flame front wrinkling in a modestly wider area in the modified Borghi diagram in Figure 5.5), before being neutralized by turbulent strain. The area in question is located below the blue line.

6 Model validation

6.1 Computational setup

The coupled, explicit, density-based, unstructured, 2nd order FVM numerical method derived in Chapter 2 is used for validation simulations here. The AUSM⁺ up flux scheme's pressure and momentum diffusion coefficients were set to $K_p = 0.25$, and $K_u = 0.75$, while the limiting Mach number was $M_{\text{lim}} = 0.1$. The CFD condition was kept at CFL = 1 for all cases, which was achieved by setting the m parameter in Equation 2.74 to $m = 3$. The bounded Sharp and Monotonic Algorithm for Realistic Transport (SMART) (Darwish et al., 2016) scheme was used for cell-face interpolation, while the gradient of the regress variable b appearing in the source term (Equation 2.24) was evaluated using a cell-limited, vertex-based Gauss method. The inclusion of the effect of gravitational acceleration was accomplished by adding the appropriate terms into the momentum and energy equations of the Navier–Stokes set of coupled equations in Equation 2.1 and 2.7. As can be seen in Section 5.1, no explicit model contribution for gravity effects on flame wrinkling is made. In all validation cases in Chapter 6, ignition was performed by switching the regress variable to a burned state ($b = 0$) in the first time step of the simulation. In validation cases in which thermal radiation posed a significant influence, i.e. deflagration in Thermal Hydraulics, Hydrogen, Aerosols and Iodine (THAI) vessel (Section 6.4, a Discrete Ordinate Method (DOM) radiation model was used. An OpenFOAM implementation of a DOM was modified to work with the explicit formulation of the Navier–Stokes equations used in the present work. The radiation model was set up to calculate 32 discrete ordinate angles (2 azimuthal and 4 polar angles) in total at each solution time step. Absorption and emission coefficients of water vapor were calculated using a gray gas

approximation. In the numerical results discussion in Chapter 6, the position of the flame is defined by the value of the reaction regress variable $b = 0.5$.

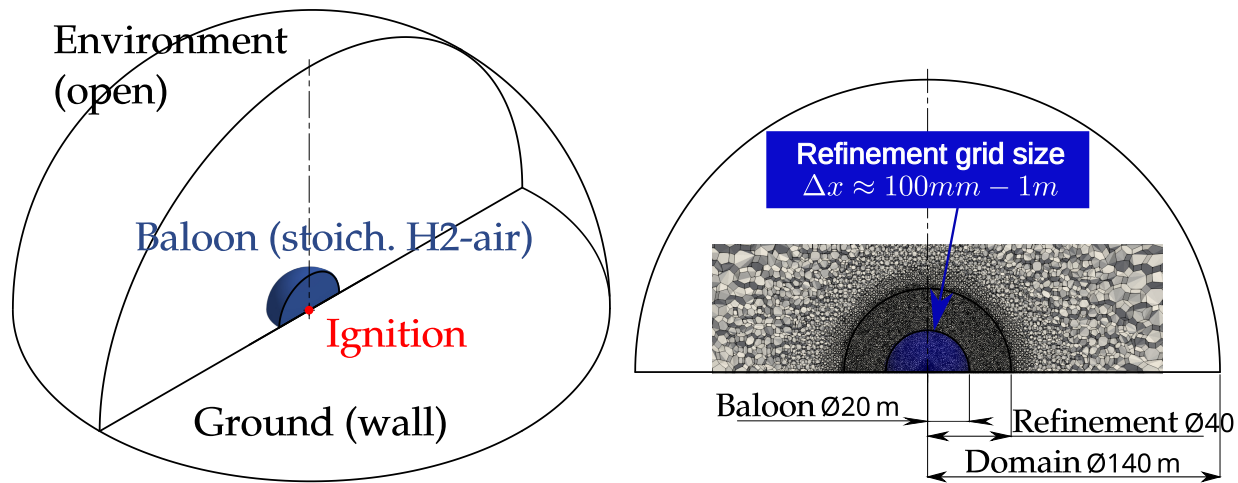
6.2 Large-scale hemispherical near-stoichiometric hydrogen flame

Simulation results for a near-stoichiometric hemispherical hydrogen–air flame propagation at atmospheric conditions are shown in this section. Mixture properties for the case can be found in Table 6.1.

Table 6.1: Characteristic properties of the near-stoichiometric H₂–air case: volumetric hydrogen concentration x_{H_2} , equivalence ratio Φ , initial temperature T_0 , initial pressure p_0 , unstretched laminar flame speed $S_{l,0}$, laminar flame thickness δ_1 , effective Lewis number Le_{eff} , Markstein length \mathcal{L} .

x_{H_2} [%]	Φ [-]	T_0 [K]	p_0 [bar]	$S_{l,0}$ [m/s]	δ_1 [mm]	Le_{eff} [-]	\mathcal{L} [mm]
29.7	1.01	283	0.989	2.07	0.015	1.12	0.04

The study by Schneider and Pfortner (1983) is particularly suitable as a starting point for validation of the DL instability model derived in Section 5.1 given that it considers a nearly-stoichiometric mixture, which allows for the assessment of the DL wrinkling calculated by Equation 5.10, with a negligible influence from other effects that appear in the total effective wrinkling factor (Equation 5.17). Furthermore, the geometric scale of the experiment is comparable to a full-scale reactor containment which allows us to validate the numerical simulations at the scale of intended applications. Lastly, the unconfined deflagration of a homogeneous mixture ignited at its center results in a hemispherical flame shape. Given that the flame propagates undisturbed, it is possible to assess the modeling approach in absence of secondary interactions between the flame and the surroundings (e.g. in a confined geometry, the influence of the walls). The influence of the pressure rise on the flame propagation speed is negligible in the open atmosphere.



(a) Hemispherical computational domain, (b) View of the computational grid and the refined zone.

Figure 6.1: Computational setup for the hemispherical flame propagation, near-stoichiometric H₂-air mixture ($x_{\text{H}_2} = 29.7\%$).

In the experimental study (Schneider and Pförtner, 1983; Becker and Ebert, 1985), a polyethylene balloon with a diameter of 20 m was filled with a homogeneous H₂-air mixture with 29.7% volume fraction of hydrogen. Initial pressure and temperature were 98.9 kPa and 283 K. Mixture homogenization was achieved with induced mixing by fans inside the balloon. To ascertain the mixture distribution, gas samples at different heights were analyzed with gas chromatography. No analysis of the initial turbulence intensity was conducted. Ignition pills (150 J) were used to ignite the flame at the center of the hemisphere. The flame front was imaged with multiple high-speed cameras, providing the data on flame position and shape, which are used here for comparison with numerical results in Figures 6.3 and 6.5. The study (Schneider and Pförtner, 1983) reports an error estimate in flame position measurements of $\pm 5\%$ (error bars in Figure 6.3a).

The computational domain (Figure 6.1) modeled in numerical simulations was hemispherical in shape, with a diameter of 140 m. Figure 6.1 shows the computational domain, boundary conditions and a two-dimensional cut through the computational grid. Figure 6.2 shows a detail of the mesh refinement in the center of the domain. The balloon area from the experiment was

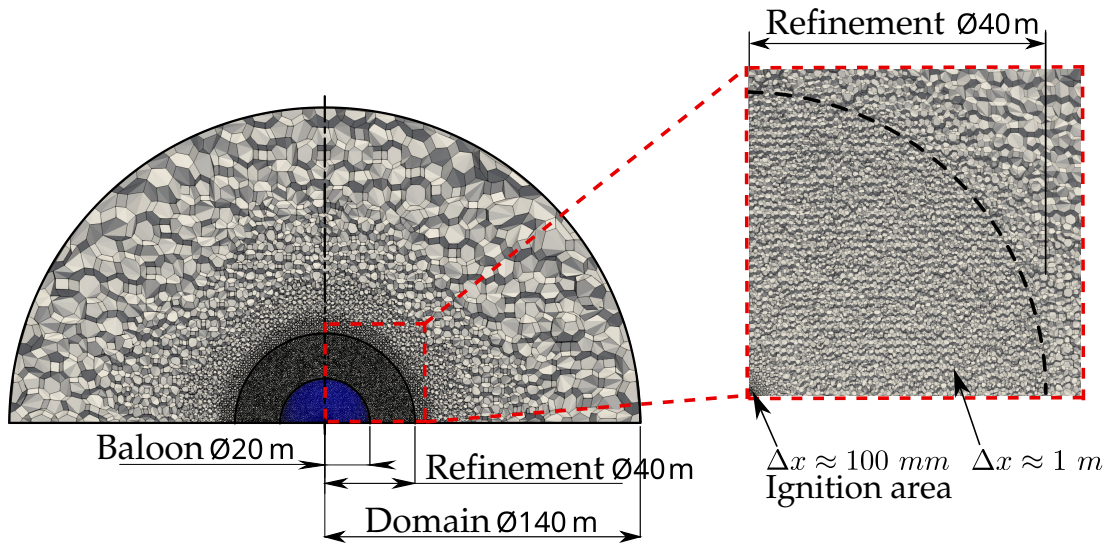
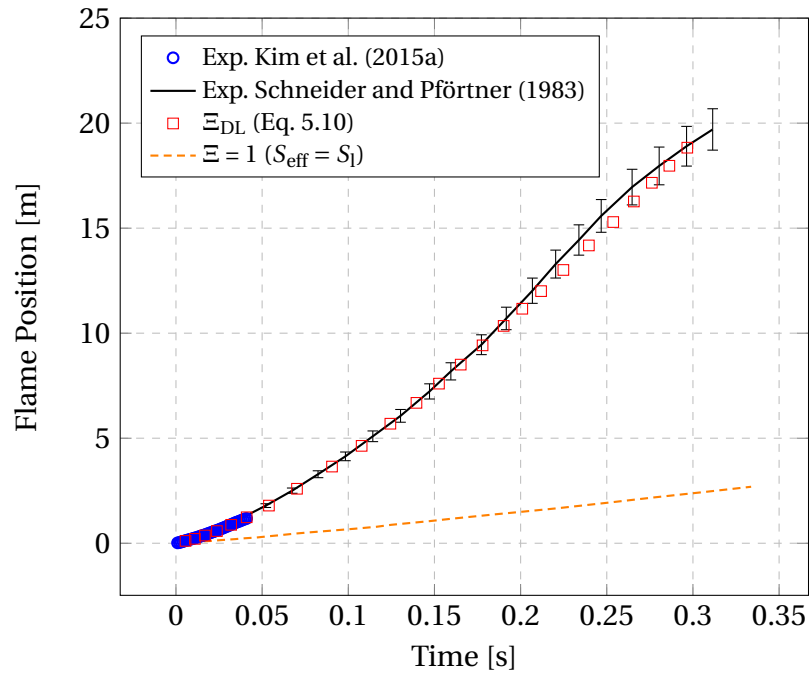


Figure 6.2: Details of the computational grid used for the large scale hemispherical flame propagation.

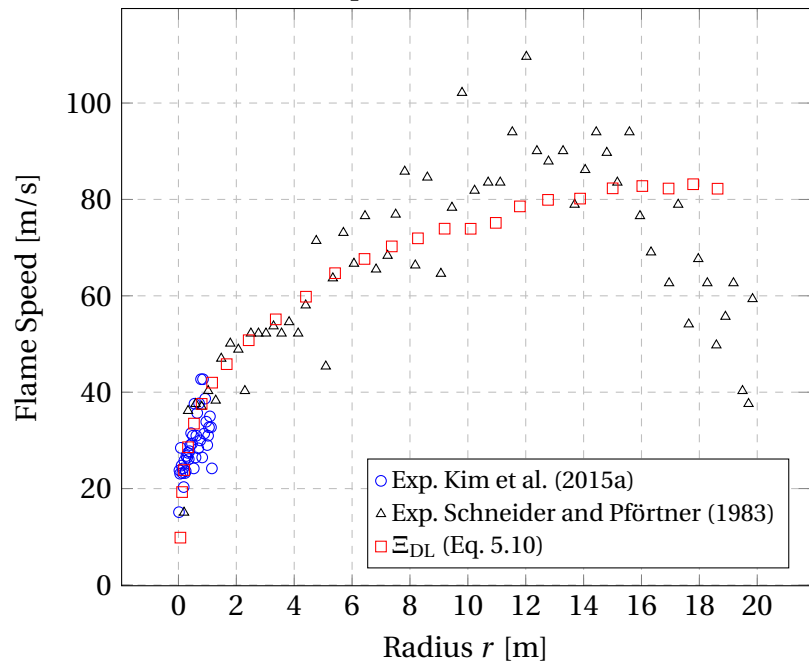
initialized as a H_2 -air mixture, while other mechanical parts present in the experiment (e.g. a wire mesh) were not modeled in the simulations, given that they were considered negligible by the study authors (Schneider and Pfortner, 1983). The volume surrounding the balloon was initialized as air. Boundary conditions at the ground were no-slip walls while the round boundary toward the outside was modeled as a non-reflecting outlet boundary condition (Zivkovic and Sattelmayer, 2021).

The computational grid consisted of polyhedral cells, the advantage of which is in their efficiency when applied with FVM, and relative ease of automatic generation. The cell size varied in the domain, with the refined balloon area (Figure 6.2). Grid spacing at the center of the balloon was approximately $\sqrt[3]{V_{\text{cell}}} = 100 \text{ mm}$ and gradually increased to 1000 mm (1 m) at the edge of the balloon. The grid spacing remained constant up to $d = 40 \text{ m}$ (refinement zone shown in Figure 6.2), and progressively coarsened in radial direction from that point onward. Radiative heat transfer was neglected in this case. Effects of the gravitational acceleration were modeled by source terms in the momentum and energy equations. The initial turbulence in the computational domain was assumed negligible. Flame propagation was initiated by switching the regress variable to burnt state in the middle of the domain (Figure 6.1).

6.2 Large-scale hemispherical near-stoichiometric hydrogen flame



(a) Flame position evolution.



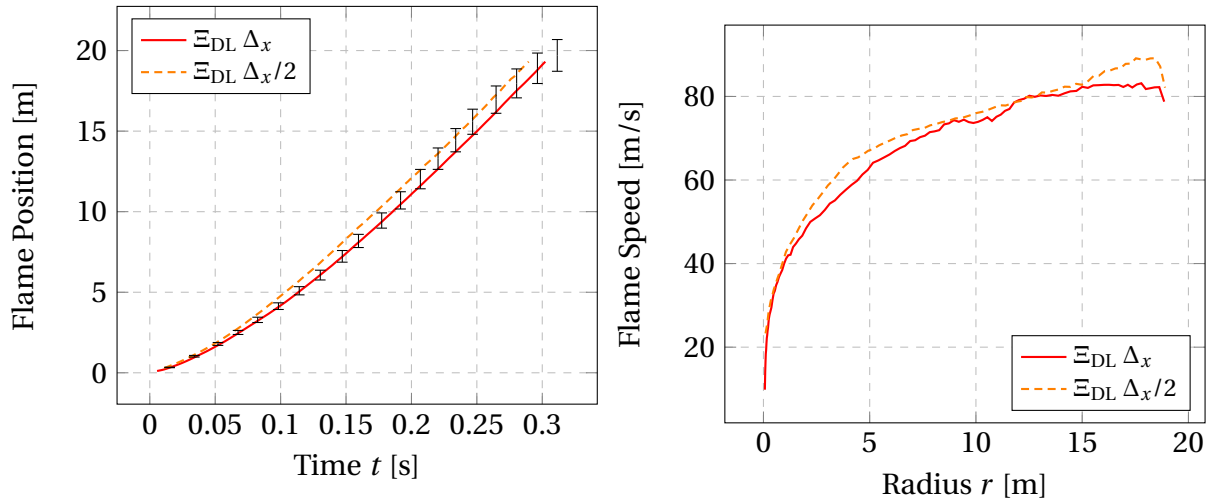
(b) Observable flame speed.

Figure 6.3: Results for the hemispherical H_2 -air flame with $x_{\text{H}_2} = 29.7\%$.

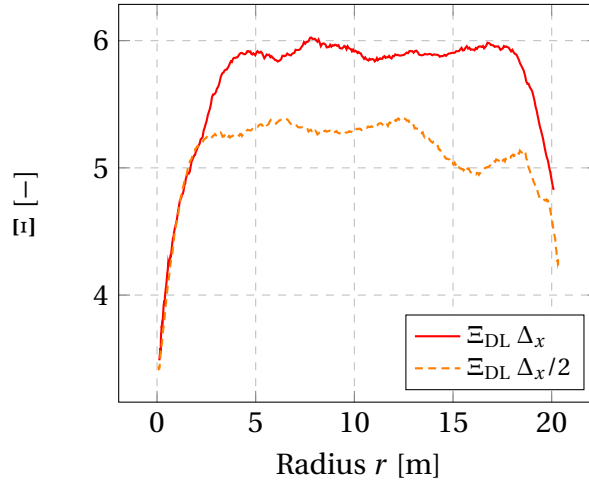
Figure 6.3 compares results of flame position and observable flame speed from simulations and experimental measurements reported in Schneider and Pförtner (1983) and a small-scale experiment with the same mixture composition by Kim et al. (2015a). Results of a simulation without a DL-instability model, marked as S_1 in Figure 6.3, are also included for comparison, in which $\Xi = 1$ was imposed, causing the burning rate in Equation 2.24 to be calculated assuming $S_{\text{eff}} = S_1$ (see Equation 2.25). Flame position calculated by the DL-instability model (Equation 5.10) remains in the $\pm 5\%$ error interval of the flame front measurements. The observable flame speed shown in Figure 6.3b was obtained from the flame position data by differentiation. It is visible that the flame speed drops in the experiment, as the flame propagates further away from the origin. This effect could potentially result from dilution of the fuel mixture by further mixing with the surrounding air as the still-unburned gas gets pushed further away by the incoming expanding gas. In the simulation results, the flame speed seems to asymptotically approach a constant value before the flame gets extinguished, reaching the surrounding inert air. A similar behavior of the flame speed was observed in an earlier numerical study of the same experiment, reported in Molkov et al. (2006b).

A refined grid was used to assess the grid independence of the solution. The grid spacing of the initial grid was halved in the entire domain ($\Delta_x/2$), while maintaining the overall structure of the original (Δ_x) (Figure 6.1). The results of the flame speed shown in the central plot of Figure 6.4 show that the difference in refinement plays a larger role in the earlier phase. The flame accelerates slightly faster for the finer grid due to better resolution of the flame surface gradient. However, the flame speed on both grids converges between $r = 5$ m and $r = 10$ m. As discussed earlier in this section, the mixing effect with the surrounding inert air likely causes a drop in flame speed at a late stage of propagation. This effect can be observed earlier for the coarser mesh, suggesting that the mixing process requires a finer grid to be resolved. However, given the intended application of the developed model, the overall flame speed and propagation behavior seems to be represented well in the area of interest by the coarser (baseline) computational grid. Comparison between effective wrinkling factors Ξ (Equation 5.17) can be seen in Figure 6.4c. For both grids, the wrinkling factor reaches a constant value, albeit the two val-

6.2 Large-scale hemispherical near-stoichiometric hydrogen flame



(a) Flame position evolution on two refinement levels. Error bars from experiment by (Schneider and Pförtner, 1983). (b) Influence of the grid refinement on flame speed.



(c) Wrinkling factor Ξ (Eq. 5.17) computed using two levels of grid refinement.

Figure 6.4: Comparison of results calculated on the base grid (Δ_x) and a refined grid ($\Delta_x/2$).

ues are not equal. This is to be expected for a scale-adaptive model (Equation 5.10), considering that a greater portion of flame surface wrinkling remains unresolved (sub-grid) on a coarser mesh, resulting in a higher value of Ξ . The expected behavior for such a model would be a gradual decrease of the modeled Ξ towards a limiting case of a grid $\Delta_{x,\infty}$, in which case all scales of the flame front would be resolved and the DL modeling term (Equation 5.10)

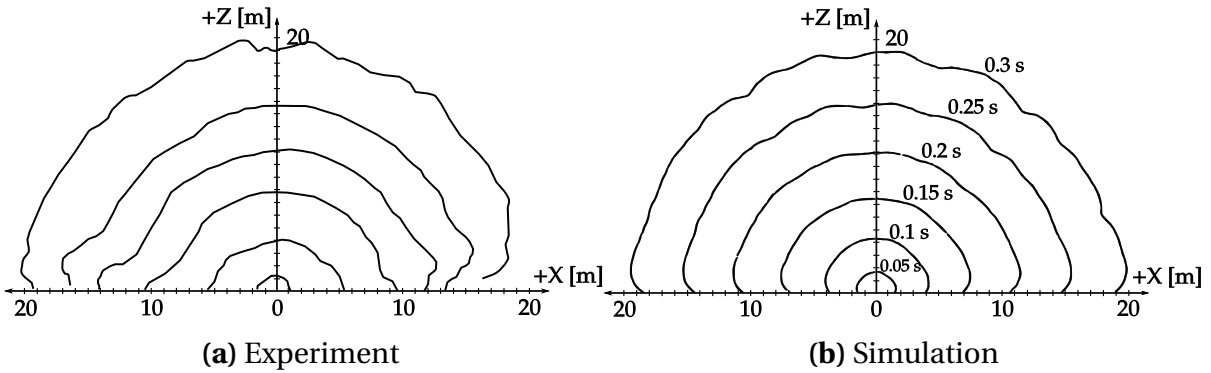


Figure 6.5: Flame shape comparison for hemispherical flame propagation and the near-stoichiometric H_2 –air mixture ($x_{\text{H}_2} = 29.7\%$). The image shows flame position isochrones.

would become redundant. The increase in Ξ for $r < 5$ m in Figure 6.4c is partially due to varying grid size near the ignition area (mesh detail in Figure 6.2). Considering that δ_1 is constant in a homogeneous gas mixture, while fractal excess β and the C_{DL} are described as constants in the model derivation, the evolution of the wrinkling factor Ξ depends solely on flame von Kármán scale $L_{\text{vK},f}$. Results of the wrinkling factor Ξ in Figure 6.4c suggest that a constant value of $L_{\text{vK},f}$ is reached during flame propagation. This asymptotic behavior qualitatively corresponds with a terminal velocity for DL-perturbed flame proposed and discussed in Yu et al. (2015).

As the flame diameter grows in an unconfined space, the flame front retains its hemispherical shape which was well predicted in simulation results (Figures 6.5, 6.6 and 6.7). Experimental contours show a greater intermittency in shape close to the ground (Figure 6.5a). This is likely due to some shear stress in the boundary layer present in the vicinity of the ground. The numerical method solves for the mean reaction progress out of which a mean position of the flame surface follows, resulting in smoother contours close to the ground.

Figures 6.6 and 6.7 show a wrinkled three-dimensional isosurface of $b \approx 0.5$, suggesting that the simulation likely resolves some of the large-scale flame structures. The calculated flame wrinkling field Ξ in Figure 6.6 shows pronounced local minima and maxima. The areas with higher Ξ can be expected

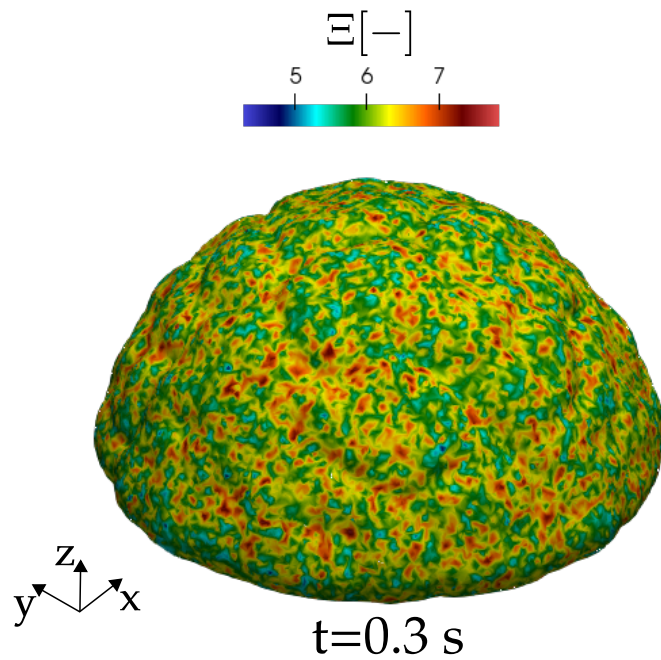


Figure 6.6: A wrinkling factor Ξ field on the isosurface of reaction regress variable $b \approx 0.5$ at $t = 0.3 \text{ s}$.

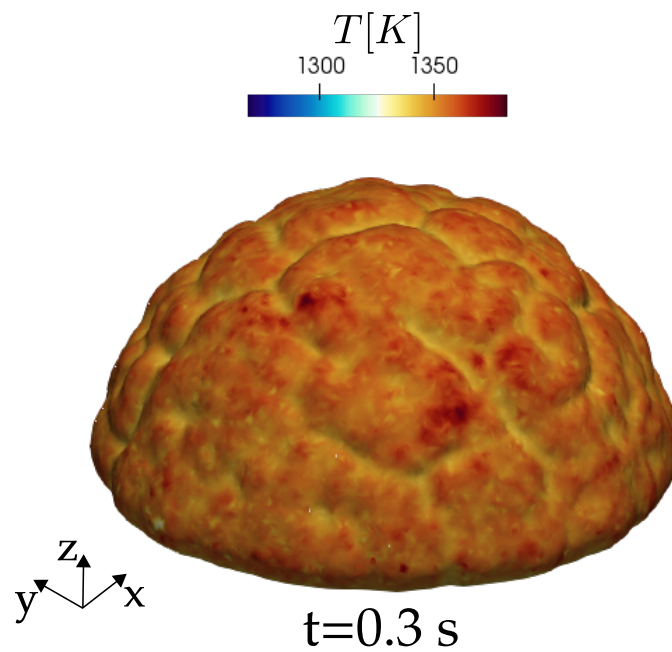


Figure 6.7: A temperature field on the isosurface of reaction regress variable $b \approx 0.5$ at $t = 0.3 \text{ s}$.

to accelerate faster relative to the areas with lower Ξ , which phenomenologically corresponds to the description of a DL-instability-perturbed flame front (Figures 4.1 and 4.2). The temperature field on the flame surface ($b = 0.5$) is shown in Figure 6.7.

6.3 Lean spherical hydrogen flames

The second validation case is considering unconfined spherical flame propagation for lean hydrogen–air mixtures at atmospheric conditions listed in Table 6.2 and at quiescent initial state. Lean H_2 –air mixtures are particularly important for nuclear reactor safety (Bentaïb et al., 2015). They are characterized by the TD instability effects described in Section 5.2, which can make them more prone to self-acceleration.

Table 6.2: Properties of spherical lean H_2 –air cases. Volumetric hydrogen concentration x_{H_2} , equivalence ratio Φ , initial temperature T_0 , initial pressure p_0 , unstretched laminar flame speed $S_{l,0}$, laminar flame thickness δ_1 , effective Lewis number Le_{eff} , Markstein length \mathcal{L} .

x_{H_2} [%]	Φ [-]	T_0 [K]	p_0 [bar]	$S_{l,0}$ [m/s]	δ_1 [mm]	Le_{eff} [-]	\mathcal{L} [mm]
19.08	0.57	298	1.0	0.75	0.038	0.60	-0.15
16.9	0.49	298	1.0	0.54	0.052	0.53	-0.21
14.2	0.40	298	1.0	0.32	0.084	0.47	-0.30
12	0.33	298	1.0	0.20	0.136	0.43	-0.37

Validation data was measured in experiments by Bauwens et al. (2017) that were performed in a rectangular 64 m^3 vented enclosure with homogeneous H_2 –air mixtures. Flame position data was measured in the area of 0.6 m in diameter. The geometric scale of the experiment is considerably smaller than the scale of a typical nuclear reactor containment (also when compared to Section 6.2). However, a suitably large unconfined experiment with lean hydrogen combustion is, to the best of authors’ knowledge, unavailable in literature. Despite a smaller scale of the flame, a coarse computational grid was generated such that it remains in the range of grid cell sizes that would be

6.3 Lean spherical hydrogen flames

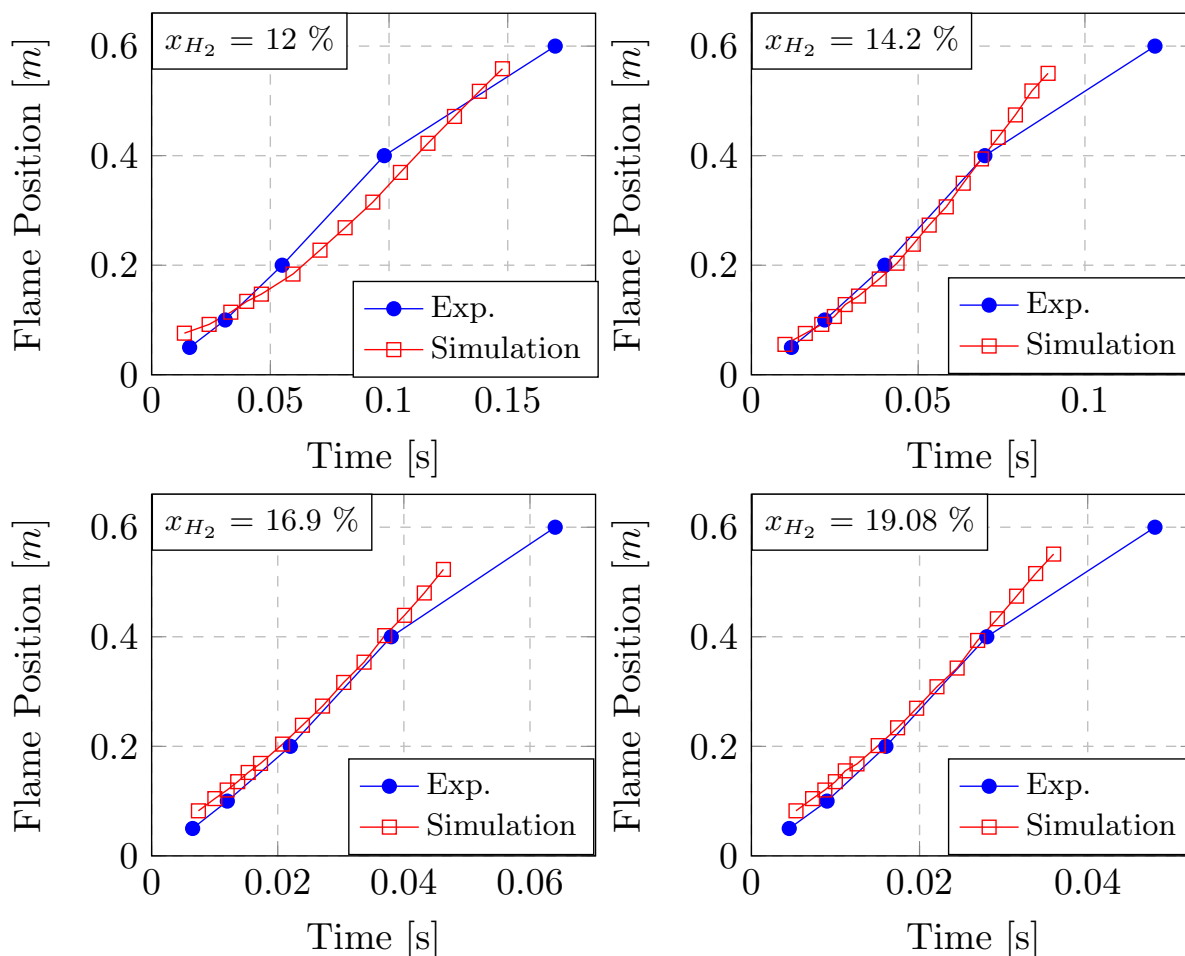


Figure 6.8: Spherical flame propagation for lean hydrogen–air mixtures. Experimental data from Bauwens et al. (2017).

used in a large-scale application. The domain was discretized with unstructured polyhedral grid cells with uniformly distributed grid spacing of approx. $\sqrt[3]{V_{\text{cell}}} = 90$ mm. The computational domain was made large enough to ensure boundary conditions do not interfere with the flame propagation initiated in the center. After ignition, the flame propagates spherically in all directions. Both gravity and radiative heat transfer were neglected in the computational setup for this case.

Figure 6.8 shows the evolution of flame position for mixtures from $x_{H_2} = 12\%$ vol. to $x_{H_2} = 19.08\%$ vol. The numerical model reproduces the nonlinear accelerating behavior of the flame. The results of the flame position generally agree

with the measured data. Experiments in the study by Bauwens et al. (2017) were conducted only once for each mixture which provided no way to analyze the measurement uncertainty or scatter. However, it can be expected that, as the hydrogen mixture becomes leaner, the flame becomes more unstable resulting in a wider standard deviation interval of the measured flame position, as was demonstrated in another experimental study by Goulier et al. (2017b) at lean stoichiometries and quiescent initial conditions. Although the agreement between experiments and simulations appears to be better for $x_{\text{H}_2} = 14.2, 16.9$ and 19.08% vol. than for the leanest mixture $x_{\text{H}_2} = 12\%$ vol., it should be kept in mind that the discussed uncertainty in measured flame position is likely to be the highest for the leanest case.

In the experimental results, a drop in flame speed is visible between the fourth and fifth measurement location ($r > 0.4$ m). This is not in agreement with the expectation that the flame acceleration in a homogeneous mixture follows an exponential acceleration curve (Bradley et al., 2001; Kim et al., 2013). Although this slowdown was not discussed in Bauwens et al. (2017), it is possible that it originates from dilution of the fuel mixture by the surrounding air, happening at distances further away from the center of the initial mixture cloud, an effect that was discussed for the validation case in Section 6.2. In the simulations, a homogeneous mixture was initialized in the entire domain and such a reduction of flame speeds at larger radii was not observed. The significance of validation in lean H_2 -air conditions presented here is tied to simultaneous effects of DL instability (Section 5.1) and small-scale effects (Section 5.2), although the pressure effect on flame wrinkling in Equation 5.17 is negligible in this case. High pressure conditions and lean mixtures will be the subject of the following Section 6.4.

6.4 Lean hydrogen flames in the THAI facility

The third validation case considers lean H_2 -air combustion in the large-scale THAI facility, at an elevated initial pressure (Kotchourko et al., 2012). The vessel is cylindrical in shape, 9.2 m in height and 3.2 m in diameter, with a narrow section near its bottom. Simulation results for experiments HD12 (HD – hy-

drogen deflagration) and HD2R (R – repeated) are presented in this section, where a homogeneous $x_{\text{H}_2} = 8\%$ vol. mixture was ignited near the bottom of the vessel resulting in an upward propagation. Initial pressure and temperature were 1.485 bar and 291 K, respectively (Tab. 6.3). Considering the initial conditions for the flame propagation, none of the terms in the model equation for the total effective flame wrinkling Equation 5.17 can be considered negligible. In the experiments, the flame position was measured using thermocou-

Table 6.3: Mixture characteristics for the THAI validation case. Volumetric hydrogen concentration x_{H_2} , equivalence ratio Φ , initial temperature T_0 , initial pressure p_0 , unstretched laminar flame speed $S_{l,0}$, laminar flame thickness δ_1 , effective Lewis number Le_{eff} , Markstein length \mathcal{L} .

x_{H_2} [%]	Φ [-]	T_0 [K]	p_0 [bar]	$S_{l,0}$ [m/s]	δ_1 [mm]	Le_{eff} [-]	\mathcal{L} [mm]
8	0.21	291	1.485	0.05	0.550	0.37	-0.50

ples mounted inside the vessel, along its centerline and on three additional axes, as shown in Figure 6.12. Pressure transducers were flush mounted at the vessel wall. The experiments in the THAI facility have been used for benchmarking of several CFD and lumped parameter codes (Kotchourko et al., 2012).

The computational model in the present work considered both gravitational acceleration and radiative heat transfer. The computational domain (Figure 6.9) consisted of the vessel volume, discretized into an unstructured polyhedral grid of nearly uniform-sized (approx. $\sqrt[3]{V_{\text{cell}}} = 200$ mm) control volumes (with slightly finer cells towards the walls).

Figure 6.10 shows temporal evolution of the vertical position of the flame (Figure 6.10a) and the flame speed along the vessel centerline (Figure 6.10b). Both show good agreement between experiments and simulations. The experimental data was taken from two experiments (HD12 and HD2R) conducted at same nominal operating conditions (x_{H_2} , p and T). Flame position measurements show a small difference between HD12 and HD2R at the start of flame propagation, with the difference growing slightly as the flame is rising towards

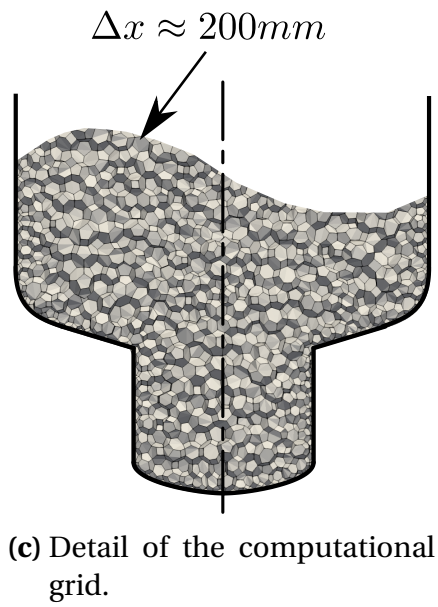
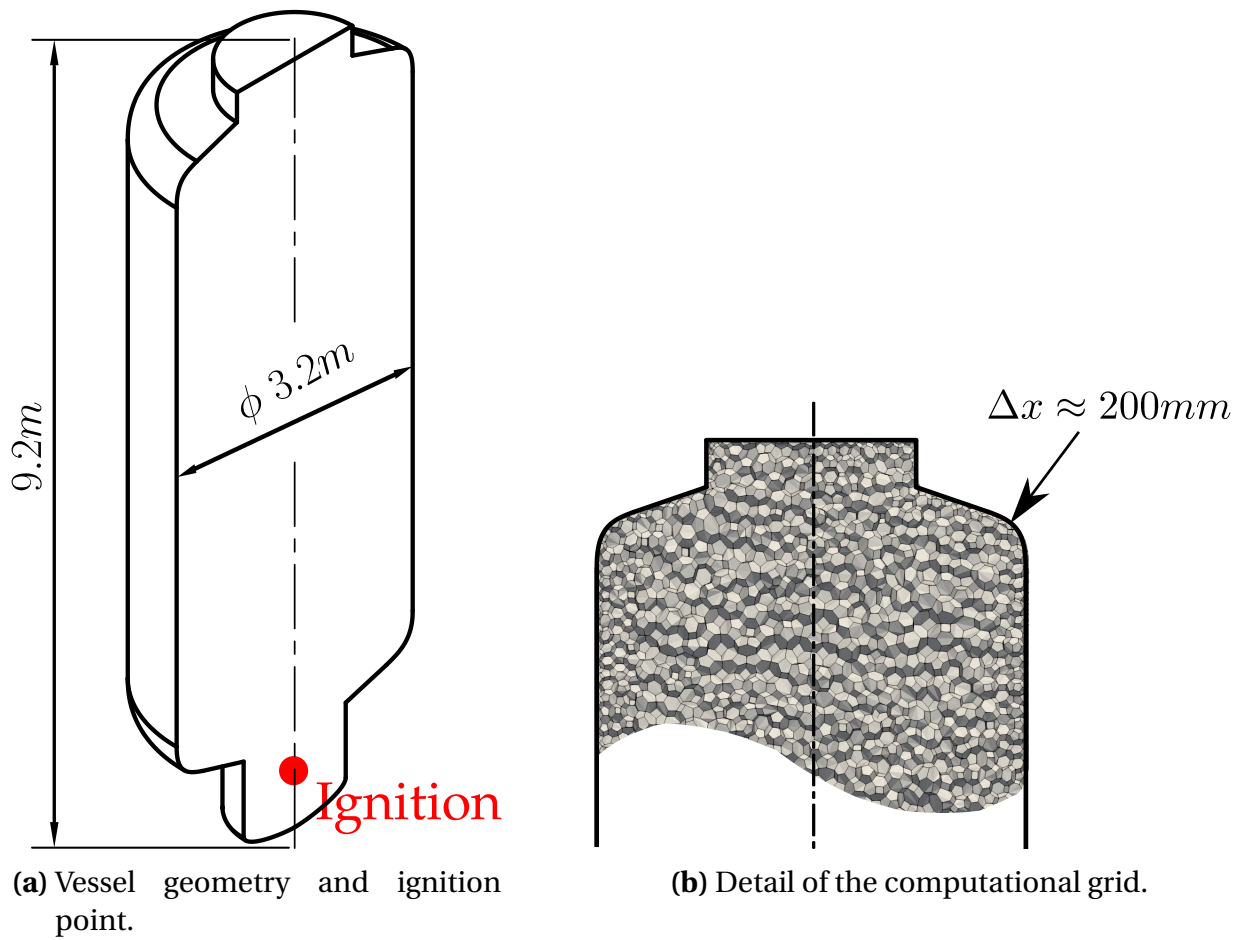
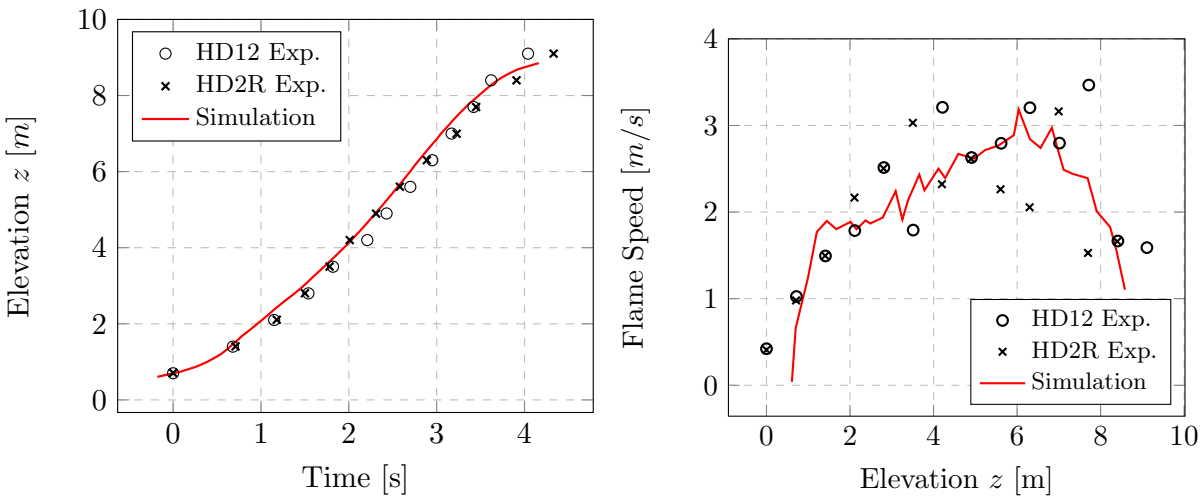


Figure 6.9: Computational domain representing the THAI vessel and a cut through the unstructured polyhedral grid.

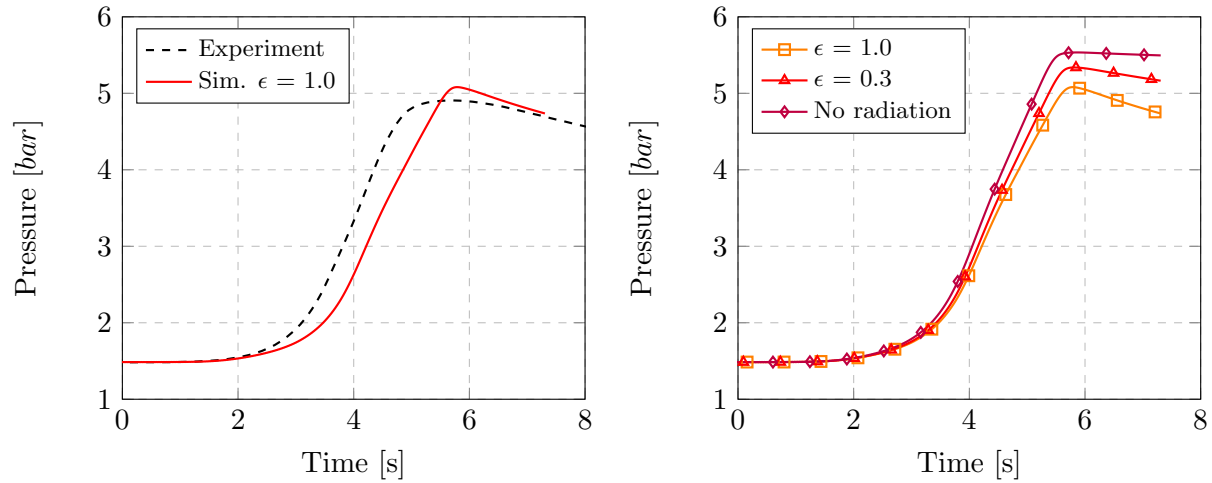


(a) Flame position over time along the centerline. (b) Flame speed along the vessel centerline.

Figure 6.10: Upward hydrogen deflagration in the THAI vessel, cases HD12 & HD2R ($x_{\text{H}_2} = 8\%$, Tab. 6.3)

the top of the vessel. This is in line with observations in Section 6.2 where a similar increase in scatter was observed as distance increases. However, since the THAI facility is closed, there can be no dilution effect from the surrounding air. Flame time of arrival is defined in all results as relative to flame arrival at the first measurement location, mounted at $z = 0.7$ m (0.2 m above ignition location). Such definition allowed for clearer comparison since the time of ignition in the experimental data is uncertain.

The pressure plot in Figure 6.11 shows simulations predicting the pressure peak fairly well, with the maximum pressure in the simulation being moderately higher. The benchmarking exercise in Kotchourko et al. (2012) concluded that computational models which included all heat transfer mechanisms (i.e. including thermal radiation) obtained a better agreement with pressure measurements. The difference in peak pressure between models with and without heat loss modeling could be as high as $p = 0.75$ bar (Kotchourko et al., 2012). Although the THAI facility had no means of quantifying the relative importance of different heat transfer mechanisms, computational work by Sathiah et al. (2016a) suggests that radiative heat transfer played the most significant role in overall heat loss. This observation is supported by the pressure



(a) Comparison between calculated and measured pressure transient. (b) Difference in pressure results between different choices of surface emissivity ϵ and a case without modeled radiation heat transfer.

Figure 6.11: Pressure rise for the THAI hydrogen deflagration case HD12 ($x_{\text{H}_2} = 8\%$).

plots in Figure 6.11 showing the comparison between a case where radiation was neglected, in contrast to cases with radiation. Despite a very good agreement between experiments and simulations with respect to vertical flame position along the vessel centerline (Figure 6.10a), there is a larger difference in the rate of pressure rise in Figure 6.11a. The difference may originate from a third-power dependence of volume on the spatial dimensions, which amplifies the differences, given that the rate of pressure rise depends on the total combusted volume of fresh gas. Greater difference between simulations and experiments in lateral propagation, i.e. toward vessel walls could be another possibility that can be seen in the flame shape comparison in Figure 6.12. The first row in the Figure 6.12 shows flame position isochrones interpolated from the thermocouple measurements (Kotchourko et al., 2012). Simulation results are given in the second row. They were extracted as two-dimensional cut planes of the regress variable corresponding to experimental measurement locations. Experimental data shows a significant difference in flame position and shape between three different measurement planes, especially in lateral directions. Furthermore, experimental data shows a degree of asym-

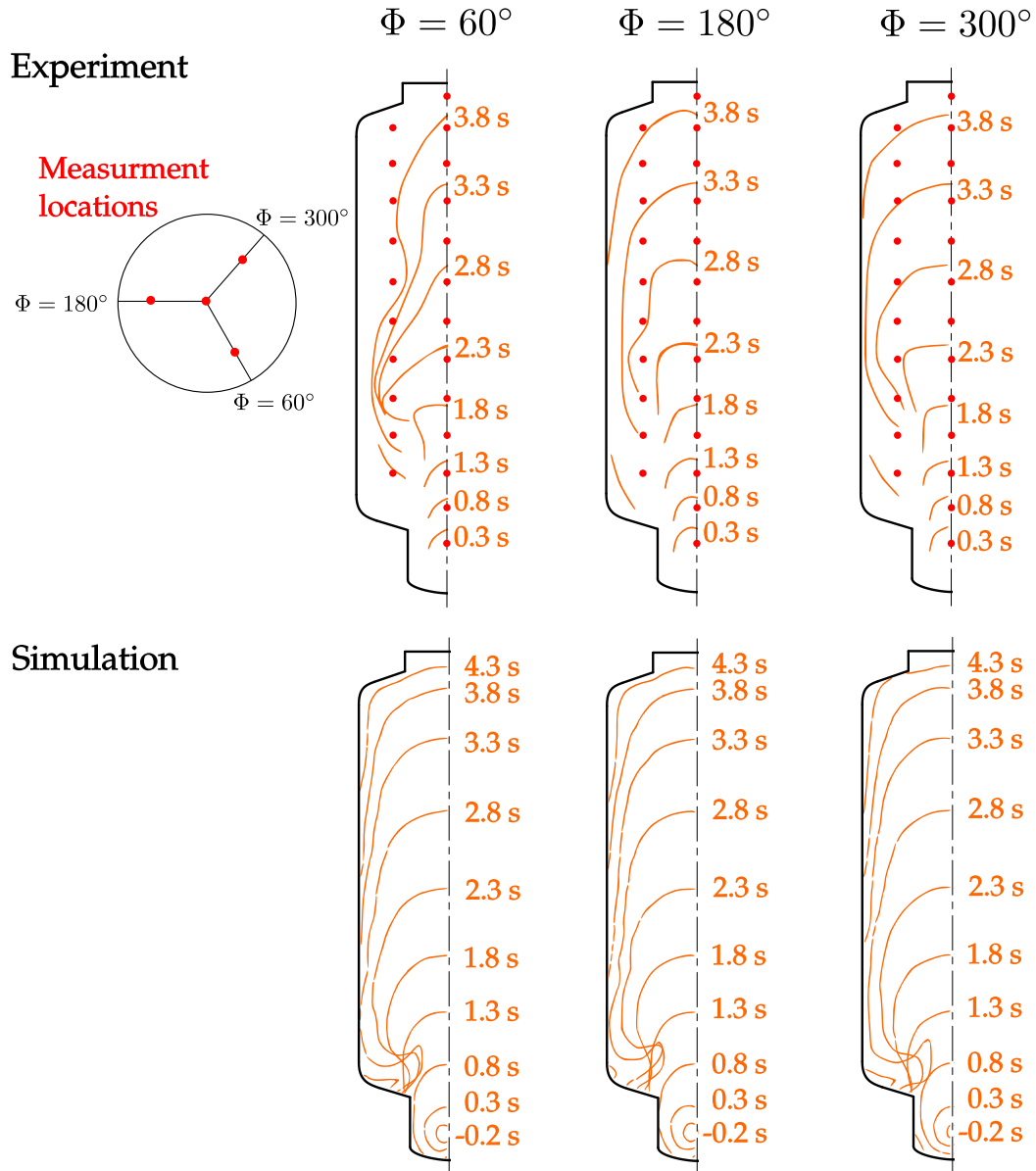


Figure 6.12: Flame shape comparison for the upward hydrogen deflagration in the THAI vessel, case HD12 ($x_{\text{H}_2} = 8\%$).

metry in flame shape. This is, on the one hand, in line with the previously discussed expectation of a highly unstable flame occurring for very lean conditions (Goulier et al., 2017b). On the other hand, it can not be fully excluded that the presence of vessel walls influences lateral propagation.

In contrast to the data interpolated from measurements, the flame shape in the simulation results is more symmetric and smooth, due to simulations producing an averaged flame position that was calculated with a relatively coarse spatial and temporal discretization. A coarse discretization is generally unable to resolve higher frequencies that could be present in flame motion. The flame is not completely symmetric in the simulation results either. However, the asymmetry here likely stems from a lack of symmetry in the unstructured computational grid, which resulted in marginally off-center ignition. Only one grid point was ignited, thus the shape of that particular polyhedral grid cell had influenced the initial propagation of the flame.

Compared to previous validation cases (Section 6.2 and 6.3) flame propagation in the present case can no longer be characterized as unconfined. If flame shapes are compared in Figure 6.6 and Figure 6.13 (or Figure 6.5 and 6.13), an elongated shape with a thin part near the bottom can be observed in the THAI vessel, in contrast to Section 6.2 where flame remains hemispherical. The driving mechanism behind the elongation in the present case is a recirculation zone that forms as shown in Figure 6.14. The recirculation zone persists throughout the flame propagation and travels upwards with the flame. The cause of the recirculation flow structure seems to be the expanding gas that gets deflected by the wall partly upward and partly downward, creating vortex structures seen in Figure 6.14.

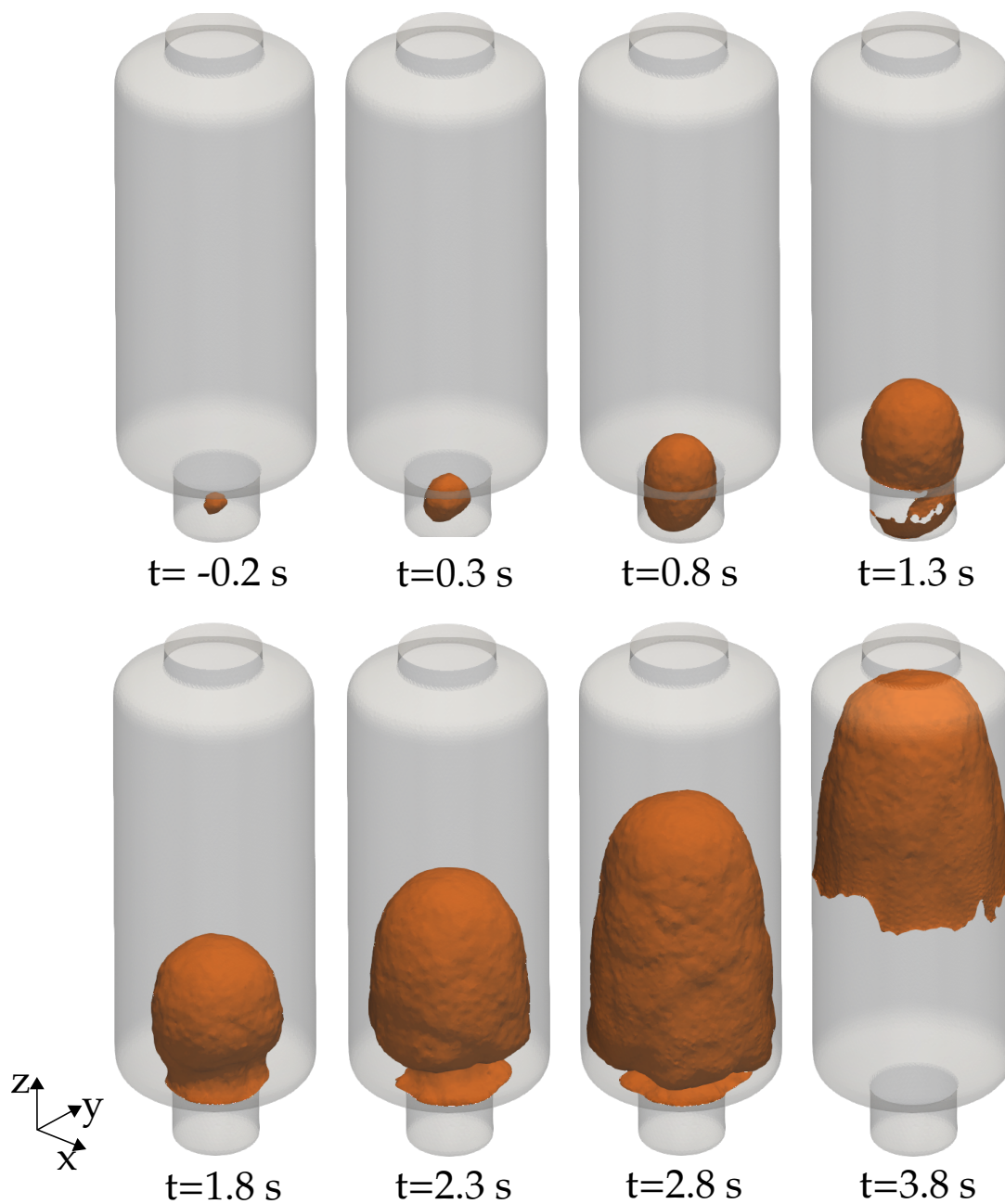


Figure 6.13: Isosurfaces of the flame front in the THAI vessel, defined as reaction regress variable $b \approx 0.5$ show an elongated flame shape.

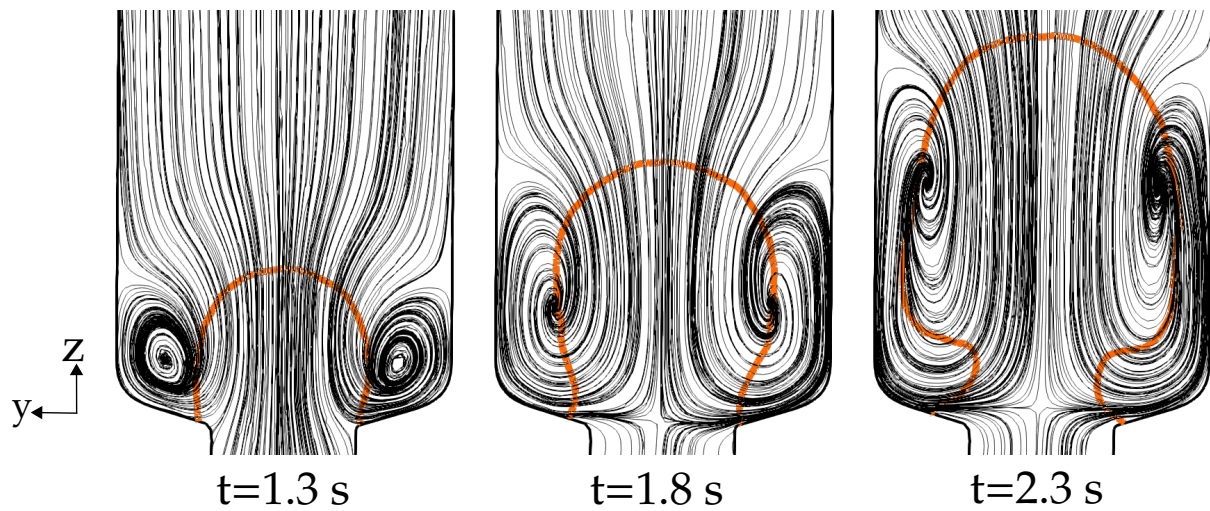


Figure 6.14: A cut through the flame surface is shown by the $b \approx 0.5$ isoline (orange). Streamlines (black) show a recirculation zone near the THAI vessel wall where fresh gas is pushed downward.

7 Concluding remarks

Part II of the present work presented the derivation of a scale-adaptive URANS approach for modeling the effects of the Darrieus–Landau instability on hydrogen–air flames at large geometric scales. The advantage of the new sub-grid model is that it can allow for industrial-scale explosion simulation without prohibitive computational cost. Furthermore, the model formulation has no dependence on global flame front radius nor it introduces flame shape assumptions. Small-scale effects of thermal–diffusive instability, local flame curvature and pressure were included using empirical correction factors.

The proposed numerical model demonstrated a reasonable agreement with multiple experiments at medium and large scales, in conditions of negligible initial turbulence. Computational setups with coarse grids were used where the grid spacing is orders of magnitude larger than the laminar flame thickness $\Delta_x \gg \delta_l$. Validation included both unconfined atmospheric deflagrations, as well as a deflagration in a large-scale cylindrical vessel with elevated initial pressure. Mixtures in the validation studies ranged from lean to stoichiometric.

Part III

Application to Generic Containment Accident Analysis

8 Introduction to combustion CFD for reactor accident analysis

8.1 Full-scale containment combustion simulations

An overview of numerical methods and CFD codes in the explosion safety domain was given in Section 1.2.2. Here, the focus is on an overview of published work that applied such methods to full-scale reactor containment analysis. First such CFD simulations were performed using tailor-made numerical analysis tools from the GASFLOW family, i.e. COM3D and DET3D. Breitung and Royl (2000) detailed the analysis workflow and provided examples of gas dispersion (GASFLOW), turbulent deflagration (COM3D) and detonation (DET3D) calculations of generic Boiling Water Reactor (BWR) and PWR cases.

Baraldi et al. (2007) reported numerical simulations of hydrogen deflagrations in an EPR containment at the plant scale, using two CFD codes: commercial CFX(v4) and in-house REACFLOW (Wilkening and Huld, 1999). In the study, the Eddy–Dissipation Combustion (EDC) model was applied for combustion and $k-\epsilon$ model for turbulence (Baraldi et al., 2007). Although the geometric representation of the containment was greatly simplified, several configurations with different positions, numbers and sizes of cross-compartment vents have been analyzed in the study, demonstrating the potential value of combustion CFD simulations in making design decisions and the importance of performing analyses at the real scale of the application.

A study of a Westinghouse PWR containment was reported by Hsu et al. (2014), where the particular reactor containment is characterized by a very large free gas volume of $100\,000\text{ m}^3$. A SBO scenario was investigated, first using the Modular Accident Analysis Program (MAAP) lumped parameter code to

determine hydrogen sources and subsequently using the FLACS CFD solver to compute hydrogen distribution and combustion. Maximum volume concentration of hydrogen in the containment reached $\approx 7\%$ with the resulting post-combustion pressure peak of 2.55 bar. However, there was no mention of modeling inert steam (H_2O) or carbon monoxide (CO) in the study (Hsu et al., 2014).

Work by Manninen et al. (2002) analyzed an SBO scenario where a hydrogen leak from an inerted BWR containment into an adjacent room above the reactor occurs in the Olkiluoto power plant. The room is 856 m^3 in size and initially contains only air. In there, a stagnant, stratified mixture of hydrogen–air forms (Manninen et al., 2000). Flame acceleration simulations were carried out using the commercial CFD code Fluent, applying $k-\epsilon$ turbulence- and EBU combustion models. This model combination was likely to overpredict the flame speed, but despite that, flame acceleration did not reach DDT conditions according to the simulation results. Additionally, a detonation load study was conducted using the DET3D solver where a detonation wave was directly initialized in the simulation. The latter allowed for analyzing the highest theoretical pressure peaks for the given mixture.

Dimmelmeier et al. (2012) applied the GASFLOW family of solvers to analyze the combustible gas control system of the EPR containment of the PWR reactor type, while Xiao et al. (2017b) applied the successor of the solver family, GASFLOW-MPI, to perform explosion simulations of the Fukushima Dai-ichi accident involving the BWR reactor type. Recently Kang et al. (2020) used GASFLOW and COM3D to analyze hydrogen combustion in the APR1400 reactor containment for an SBO accident and Kang et al. (2022) for a Small Break (SB)–LOCA, while Yabing et al. (2022) used GASFLOW-MPI to assess Flame Acceleration (FA) and DDT risk in a containment of an APWR 1000 reactor. Cited studies focused mostly on quasi-static pressure and temperature loads due to slow combustion of lean hydrogen–air and hydrogen–steam–air mixtures. None of the studies reported turbulence levels at the moment of ignition.

Kim and Hong (2015) investigated the potential for flame acceleration during an SBO accident in a containment of a Korean APR1400 reactor. GASFLOW was used for hydrogen and steam distribution analysis, where its structured

Cartesian (voxel-based) grids allowed for quick simulation turnover. However, Kim and Hong (2015) found such grids impractical for generic shapes of the in-containment structures, modeling of which resulted in a high degree of geometric simplification. Furthermore, a cylindrical coordinate system was chosen for the containment to reduce dead cells and stair-shaped walls associated with purely Cartesian grids in GASFLOW (Kim and Hong, 2015). Gas mixing results from GASFLOW were then used to initialize flame propagation simulations in OpenFOAM using a Partially Stirred Reactor (PaSR) combustion model (Kim and Hong, 2015). The OpenFOAM formulation of FVM which uses unstructured and body-fitted grids allowed for more flexibility in handling geometric complexity.

An OpenFOAM-based solver for explosion modeling was used by Hasslberger et al. (2017b) to analyze the APR1400 as well. There were three realistic scenarios in the study, one for an SB-LOCA, and two for an SBO accident (with and without the three-way valve operation). Initial conditions for the scenarios came from LP simulations using MAAP5 code. Given the lack of turbulence modeling in LP codes, there was no data on turbulence intensity available for initialization. Since the LP nodalization is much coarser than a CFD grid, a mapping procedure was developed in the cited work to interpolate and smoothen the LP result while keeping the mass and energy of original LP nodes conserved. Apart from the described realistic scenarios, a number of hypothetical DDT simulations were conducted by initializing unrealistically high hydrogen and low steam compositions, arriving at highly conservative initial conditions (Hasslberger et al., 2017b). Furthermore, Hasslberger et al. (2017a) used the same OpenFOAM-based code to analyze combustion phenomena in a Konvoi-type reactor containment. However, gas distribution simulations were not carried out in that study. Instead, hypothetical scenarios with respect to initial mixture composition, thermodynamic state and an assumed low level of turbulence were used such that a conservative analysis of DDT occurrence in the containment was achieved, demonstrating the capability of the autoignition-based DDT model implemented in the OpenFOAM-based solver to perform an efficient computation of a containment-scale case. Studies by Hasslberger et al. (2017a,b) used a turbulent flame speed correlation by Dinkelacker et al. (2011) to model the early deflagration stage.

In contrast to full containment studies where very coarse grids are necessary – e.g 22 cm in (Hasslberger et al., 2017a,b), 50 cm-1 m in (Kang et al., 2020), 1 m in (Hsu et al., 2014) – CFD can be a useful tool for studies where only a section of a nuclear facility is analyzed, allowing for more complex geometric details to be resolved. Manninen et al. (2002) used cell sizes of $\Delta_x = 10$ cm to resolve a single room in a BWR reactor building, which was enough to include larger pipes and other structures that were important for turbulence generation during flame propagation. Daudey and Champassith (2014) carried out an explosion risk analysis for six rooms at the Flamanville EPR reactor facility, ranging from 64 m³ to 600 m³ in volume using the CFD tool FLACS. Computational grids with 5 cm average cell size allowed for piping and various installed equipment to be resolved. Explosion simulations were initialized by assuming an "equivalent stoichiometric flammable cloud", which provides the safety-relevant conservative (worst-case) scenario. Moreover, the experiments used for deriving empirical inputs for efficient numerical models were mostly done at stoichiometry and in standard conditions, leading to lower model uncertainty at those operating points. For these reasons, the practice of initializing equivalent stoichiometric flammable clouds remains a standard in the industry (Daudey and Champassith, 2014). However, work by Daudey and Champassith (2014) used gas distribution CFD simulations in FLACS at a later stage to arrive at more realistic initial conditions, which were often leaner and more inhomogeneous than the assumed stoichiometric cloud. The result comparison between the two led Daudey and Champassith (2014) to conclude that using only equivalent stoichiometric gas clouds can lead to overly-conservative conclusions, emphasizing that a balance between realistic and conservative modeling needs to be pursued for some industrial applications.

8.2 Motivation and objectives of the present work

In the present work, a full-scale 3D CFD combustion analysis of a Konvoi reactor containment (Figure 8.1) during a severe accident is shown. Like in many references cited in Section 8.1, an LP code is first used to model the pre-ignition accident stages spanning multiple days. However, greater emphasis is

put on generating as realistic initial conditions as possible by applying CFD to the final stage of the mixing process immediately prior to ignition.

LP codes provide a computationally efficient way of obtaining results on long-lasting accident development process and contain sub-models for important phenomena like core melting or steam evaporation and condensation. Furthermore, they can account for the influence of the installed containment safety systems on the course of the accident.

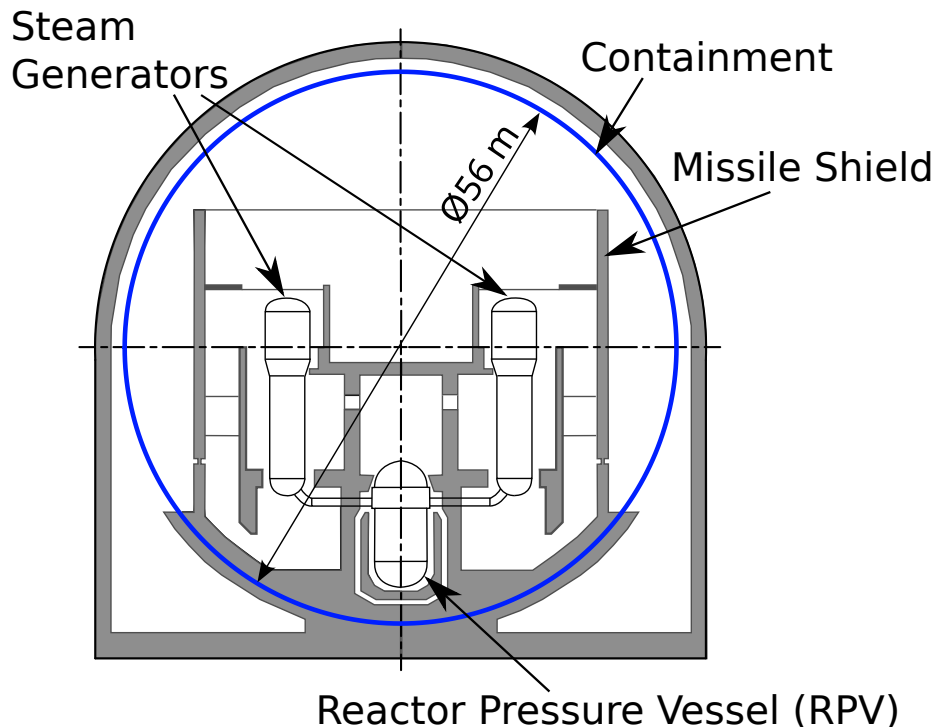


Figure 8.1: A simplified schematic diagram of the Konvoi-type reactor containment.

The analyzed accident case deals with an SB-LOCA, as defined in the Generic Containment case (Kelm et al., 2014) where the LP code Containment Code System (COCOSYS) was used (Allelein et al., 2008; Reinke et al., 2019). Following that, the results of the COCOSYS simulation are mapped on a CFD grid in order to initialize a simulation of the final stage of the gas mixing process. CFD methods can provide a more detailed insight into the complex thermo-hydraulic processes emerging inside a reactor containment. A systematic CFD

validation has been performed by Kelm et al. (2016) demonstrating a general capability of CFD to predict containment gas flows.

In the present work, the CFD code *containmentFoam* was used, developed specifically for the purpose of reactor containment thermal hydraulics and gas dispersion analysis (Vijaya Kumar et al., 2021; Kelm et al., 2021b). A more detailed pressure and temperature distribution in the containment is obtained with *containmentFoam*, as well as velocity and turbulence quantity fields. The latter is considered key in the present study due to the potentially strong influence of turbulence on the flame acceleration via turbulent flame wrinkling. Analysis of turbulence levels in the gas mixing phase prior to ignition has, to the best of author's knowledge, not been reported in the literature so far (Section 8.1). The CFD tool *containmentFoam*, based on the open-source CFD code OpenFOAM, has been validated for hydrogen mixing under representative thermal-hydraulic conditions of a LOCA using a set of benchmark cases (Kelm et al., 2019). Development of *containmentFoam* is focused on introducing or improving models that are important for accident analysis such as capturing relevant transient flow structures, e.g. jet penetration, where an understanding of turbulent heat and mass transfer phenomena can especially benefit from detailed numerical analysis (Kampili et al., 2021), radiative heat transfer (Liu et al., 2022) or steam condensation (Vijaya Kumar et al., 2021). Furthermore, work by Wenig et al. (2021) deals with uncertainty quantification for the mixing process simulations obtained with *containmentFoam*. Apart from nuclear safety, the tool has been applied to hydrogen safety in a mobility application in a study by Kelm et al. (2021a), where the accidental leakage on a liquid hydrogen carrier ship was analyzed.

Furthermore, earlier flame propagation studies found in the literature (Section 8.1) applied various forms of turbulent flame correlations for flame speed modeling, implicitly assuming a turbulent flame regime. No such a-priori assumption is made in the present work and the choice of flame speed closure is made according to the results of gas mixing CFD. For a discussion on flame speed model validity limits see Section 5.4. Furthermore, the turbulence generated during the flame propagation was analyzed in the present work.

Another goal of the present study is to demonstrate how the developed CFD methodology can be used to generate new data on important questions in the combustion phase of the reactor accident. Results of the simulations provide insight on the main integral variables of interest such as pressure evolution, overall combustion rate or maximum reached flame speed, as well as local details on flow and flame structures. Finally, the question of DDT potential in the analyzed accident scenario was assessed from the simulation results.

Part III is laid out as follows: in Section 9.1 the Generic Containment is introduced, together with the individual compartments of the Konvoi containment relevant for the study. In Section 9.2 the details of the analyzed SB-LOCA accident are given. Sections 9.3 and 9.4 introduce the computational domain, grid and the initial conditions for the combustion CFD, followed by the computational setup and models in Section 9.5. Section 9.4 also provides the details on the analysis chain integration. Simulation results are discussed in Section 9.6.

9 Numerical simulation of combustion in the generic containment

9.1 "Generic Containment" definition

The CFD simulations in the present work are initialized using results from the "Generic Containment" LP model developed by Kelm et al. (2014) following the recommendation of OECD/NEA ISP-47 (Allelein et al., 2007). The work on defining the Generic Containment was undertaken in the framework of the EU-FP7 project SARNET 2 where the Generic Containment LP nodalisation was defined based on a "Konvoi" PWR type (a.k.a "KWU-Baulinie '80") of nominal 1300 MW_e (Kelm et al., 2014). The original COCOSYS model of the power plant was developed earlier by Gesellschaft für Anlagen- und Reaktorsicherheit gGmbH (GRS) (Bönigke et al., 1998), while a simplified COCOSYS model was derived for the Generic Containment to be used in benchmark exercises that were composed of three runs with increasing complexity. The model included steam, liquid water, hydrogen, carbon monoxide, carbon dioxide releases, as well as various heat sources (Kelm et al., 2014).

The Konvoi reactor cooling system consists of four primary loops passing through four vertical U-tube steam generators. The steel shell of the reactor containment fully encloses the reactor system and has a design pressure of 8 bar and volume of $V \approx 70000 \text{ m}^3$. Besides the steel containment, the reactor building consists of an outer concrete structure. The Generic Containment case LP setup models the various rooms and compartments of the reactor building with 16 simplified volumes (zones) where individual structures and piping installations have been merged into a smaller number of logical groupings. Volume zones are connected by atmospheric (gas) and drain (liquid) junctions. Doors, rupture discs and pressure relief flaps have been sim-

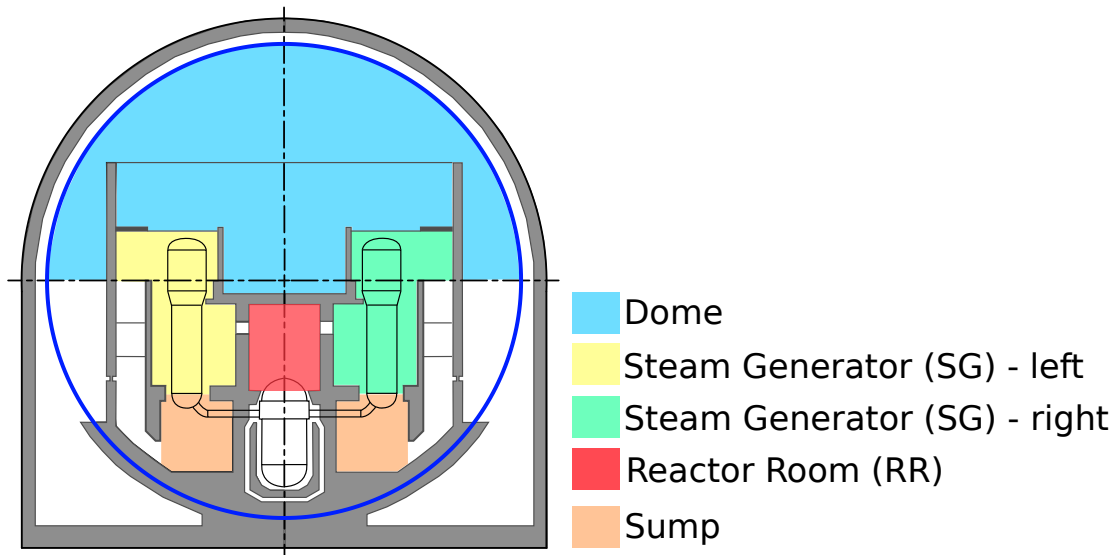


Figure 9.1: Schematic diagram of containment sections (zones) relevant to the present work: Dome, SG left & right, Sump and RR.

plified in a similar way and are represented by a rupture disc model that takes into account their respective opening overpressure. In the simplified nodalisation of the Generic Containment, the total heat capacity and the heat transfer area of the plant have been preserved (Kelm et al., 2014).

Figure 9.1 shows a schematic diagram of the containment zones from the Generic Containment case that are relevant to the present work: Reactor Room (RR), Steam Generator (SG) left, SG right, Sump and Dome. The compartments of the Konvoi containment can be conceptually divided into the "inner containment" which includes compartments within the missile shield and below the burst membranes placed on the top of the SG compartments, and the "outer containment" consisting of the Dome and the area behind the missile shield (Sonnenkalb et al., 2015).

9.2 The analyzed accident scenario

The Small Break (SB) - Loss of Coolant Accident (LOCA) scenario analyzed in the present work is based on the specification from the benchmark exercises defined in the SAMHYCO-NET research network (Klauck et al., 2021; Reinecke et al., 2022).

The progression of the accident is as follows. Initially, loss of primary coolant leads to the core heating up to the point of melting. Next, as the core damage continues to increase, the molten material relocates to the lower plenum of the Reactor Pressure Vessel (RPV). Emergency cooling water is then completely spent on reflooding the damaged core in the RPV. Finally, the RPV integrity fails and the melt relocates to the reactor cavity below. This marks the end of the "in vessel" phase of the accident.

In the next, "ex vessel" phase, the MCCI begins and additional amounts of hydrogen are produced, as well as carbon monoxide and carbon dioxide, the latter of which is neglected in the present work. Furthermore, the MCCI then stabilizes in the dry reactor cavity. Heat transfer from the containment towards the environment causes gradual condensation of the inert steam, increasing the explosion potential.

The unmitigated scenario, i.e. without Passive Autocatalytic Recombiners (PARs) operation, was modeled in the present work, representing a conservative scenario of PARs deactivation due to poisoning, fouling, thermal damage, mechanical damage or corrosion (Chakraborty, 2020).

Time [h]	Accident phase
0:00	Loss of coolant.
0:41	Core melting begins.
3:06	Melt relocation to lower plenum.
03:24	RPV failure, MCCI begins.
13:00	MCCI stabilized in a dry cavity, steam condensation begins.
47:00	Ignition in the reactor room (RR) compartment.

Table 9.1: Breakdown of the SB–LOCA accident sequence prior to ignition.

9.3 Computational domain and grid

The computational domain for numerical simulations in the present work consisted of the full-scale volume of a simplified Konvoi containment. The simplified geometry was provided by the GRS. The geometry was earlier used in a CFD study of combustion and DDT by Hasslberger et al. (2017a).

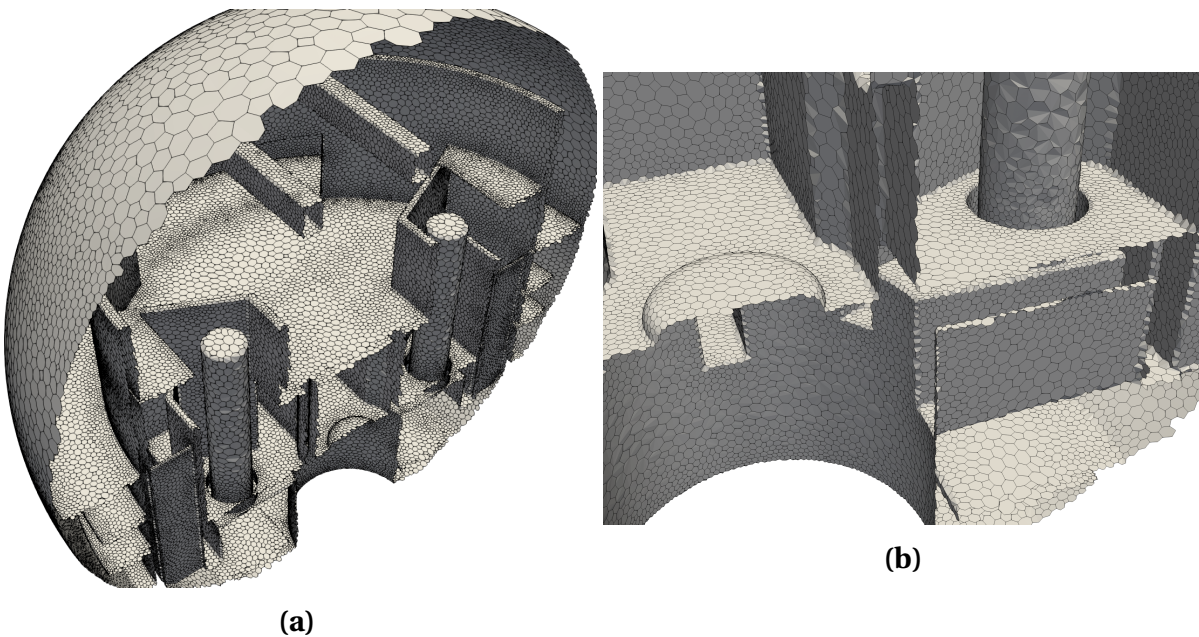


Figure 9.2: A 3D view of the unstructured polyhedral computational grid.

An unstructured polyhedral grid was generated with cell sizes ($\Delta_x = \sqrt[3]{V_{\text{cell}}}$) in the range between 0.1 m (in more confined regions close to important geometric features) and 1 m (in the top part of the containment dome). Polyhedral cells used in the present work allow for a very efficient volume discretization in terms of cell count and cell connectivity, resulting in the total grid cell count of approximately 650 000.

Near-wall areas have not been treated with increased element density (e.g. boundary layer refinement) since, for flame acceleration simulations, the area of interest is mostly in the bulk of the volume where the flame travels, while the solid walls are typically where the flame quenches. However, this modeling decision has implications on turbulence generation at the walls, which is

discussed in the Section 9.6. Figure 9.2 shows the surface grid and a detail of the more-confined sections RR, SG and Sump. Figure 9.3 shows 2D cut planes through the mesh.

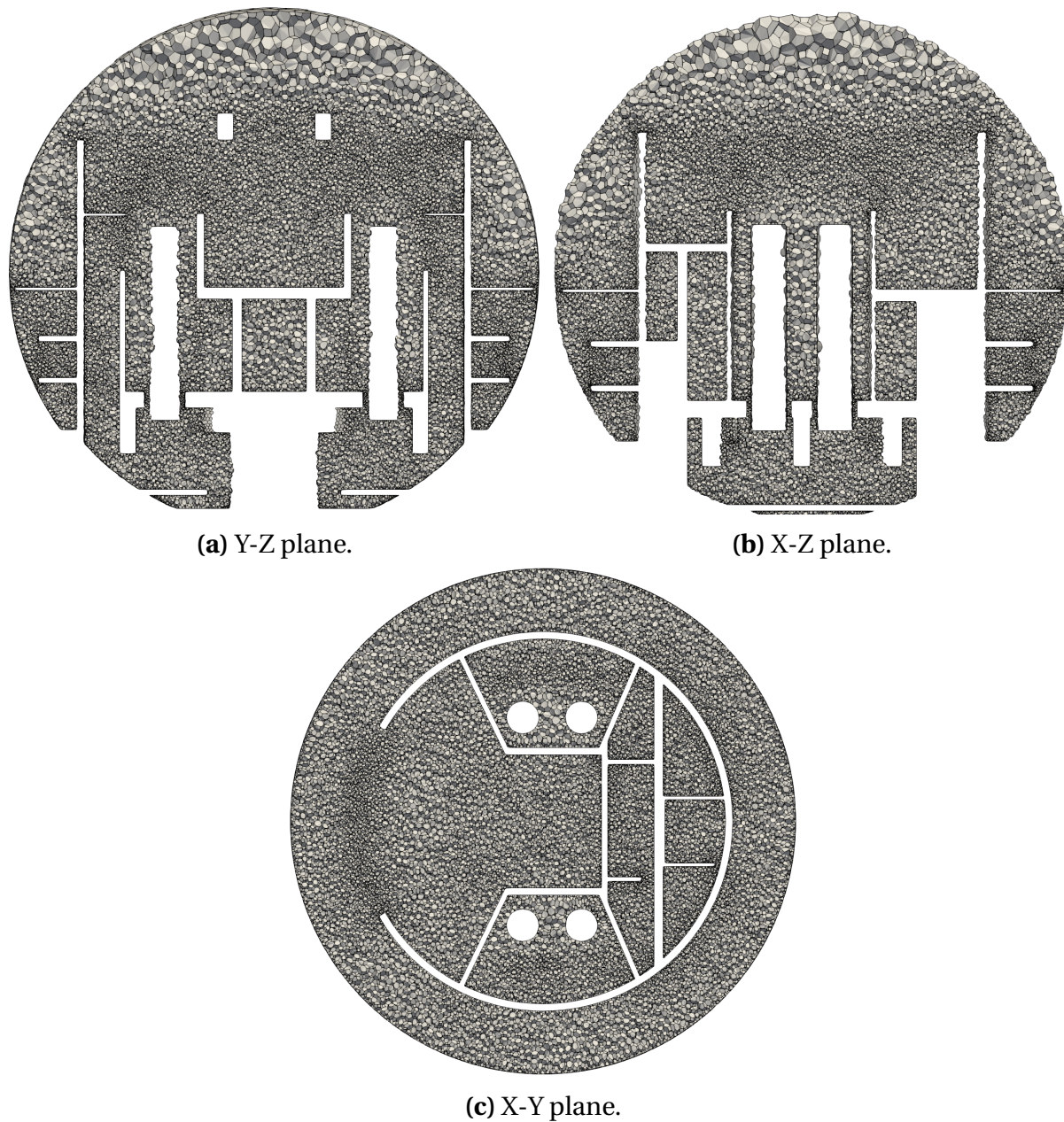


Figure 9.3: Cut-plane view of the unstructured polyhedral computational grid.

9.4 Initial conditions and ignition

9.4.1 Mixture formation phase

Given that conditions in different rooms and compartments of the containment prior to ignition depend on the complex and dynamic process of flammable mixture formation and a CFD analysis of flame propagation requires realistic initial conditions including spatial distribution and thermodynamic state of gas species, surface temperature of structures, etc., the modeling strategy adopted in the present work uses results of COCOSYS calculations of an SB-LOCA scenario in the the Generic Containment (Section 9.2), and gas distribution simulations with an OpenFOAM-based solver developed for that purpose (Kelm et al., 2021b). Figure 9.4 shows the schematic diagram of the analysis chain, including the steps required to generate the initial conditions for the combustion CFD.

In the accident scenario analyzed in the present work (Section 9.2) MCCI had stabilized in a dry cavity after $t = 13$ h from the beginning of the accident. Steam condensation gradually continued from that time onwards until $t = 47:00$ h, when ignition in the reactor room (RR) compartment occurs. The gas composition at that moment is shown in Table 9.2 and Figure 9.5.

	H ₂	O ₂	H ₂ O	CO	CO ₂	N ₂
vol.%	19.60	9.83	28.92	4.67	0.00	36.97

Table 9.2: Gas composition table at $t = 47$ h of the accident.

A detailed 3D gas mixing CFD using *containmentFoam* was initialized with Generic Containment COCOSYS results at $t = 47:00$ h. It simulated the next 5 min of time, ending at $t = 47:05$ h, which was enough to obtain the main flow patterns in the containment and produce turbulence and gas distribution fields. Results of *containmentFoam* simulation can be seen in Figure 9.6. Moreover, the simulation was able to provide a more detailed temperature and pressure field distribution immediately prior to ignition, both of which can significantly influence the combustion dynamics.

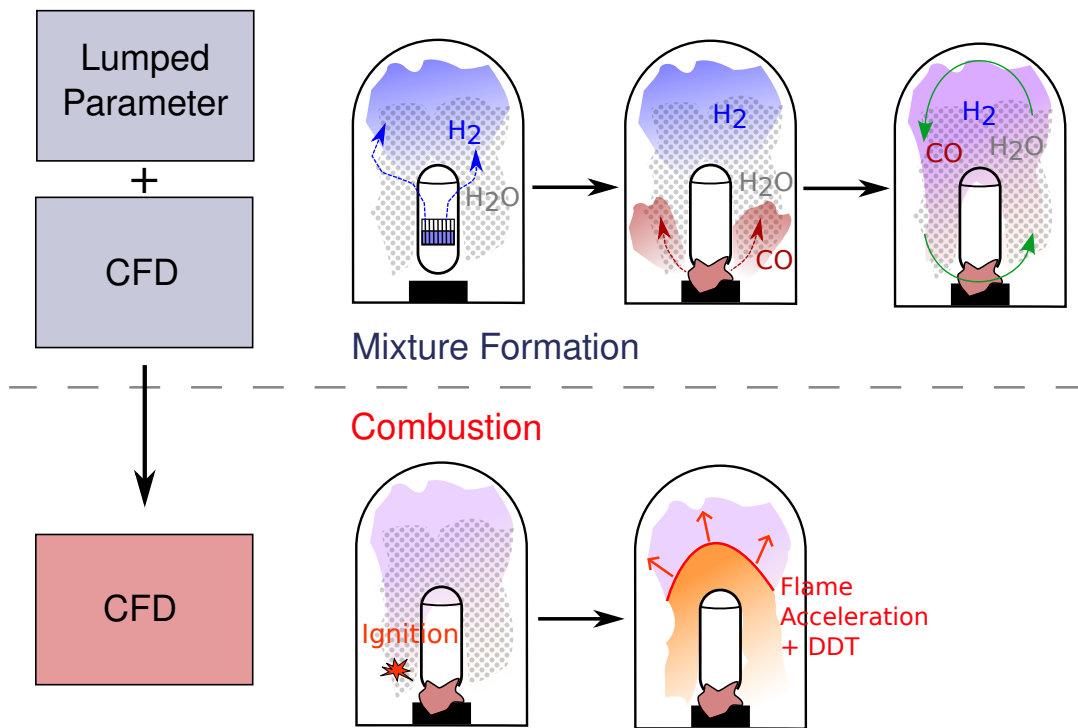


Figure 9.4: Schematic diagram of the reactor accident analysis chain used in the present work. In the mixture formation phase, the LP code used is COCOSYS, results of which were mapped to a CFD solver *containmentFoam*. The combustion CFD was performed using *explosionDynamicsFoam*, derived in Part I and Part II of the present work.

Furthermore, an estimation of turbulence quantities were calculated using a buoyancy-modified k - ω SST model, the results are shown in Figure 9.7. Turbulent kinetic energy k fields in the results show that turbulence production in the buoyancy-driven flows in the containment remains very low for the modeled scenario, as k does not exceed $1.3 \text{ J/kg (m}^2/\text{s}^2)$, a value that would have a negligible effect on flame wrinkling.

Results of both LP (COCOSYS) and CFD (*containmentFoam*) simulations show a negligible difference in gas composition between the RR, SG and Dome containment zones, which can be seen in Figure 9.6a showing the hydrogen mass fraction (x_{H_2}) field. Such a uniform distribution is an effect of convective recirculation loops that form in the containment, enhancing the gas mixing

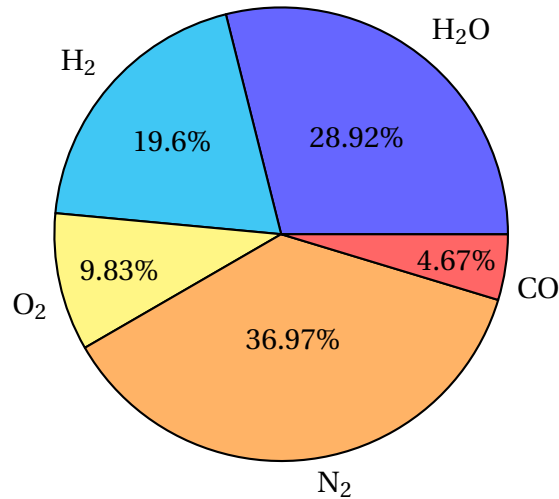


Figure 9.5: Gas composition in % vol. at $t = 47$ h of the accident.

and resulting in a nearly completely homogeneous mixture. This corresponds with the behavior in other PWR-type containments, e.g. in (Hasslberger et al., 2017b). Unlike with BWR reactor designs where leaking hydrogen from the containment can accumulate in the reactor building above the containment due to buoyancy, and result in a stratified hydrogen–air mixture (Manninen et al., 2000), which was, e.g. the case in the well-know Fukushima-Daiichi accident (Xiao et al., 2017b). In case of the Konvoi containment (and other PWRs), the emergence of one or more convective loops is promoted by the plant design with the aim of diluting the flammable gas, i.e. avoiding locally-rich fuel pockets with high FA potential.

The convective flow patterns in the Konvoi containment are depicted by the schematic diagram in Figure 9.8. Different patterns emerge depending on mainly the size and location of the release from the primary circuit, causing different pressure distributions in the containment, such that, in case of SB-LOCA or transient scenarios like SBO, only burst membranes in the ceiling of steam generator (SG) compartments break, resulting in one convection loop, while in cases of Medium Break (MB)- or Large Break (LB)-LOCA, a higher pressure differential emerges that breaks the stronger burst doors in the missile shield, resulting in two dominant convection loops and a more intense homogenization of gases (Sonnenkalb et al., 2015).

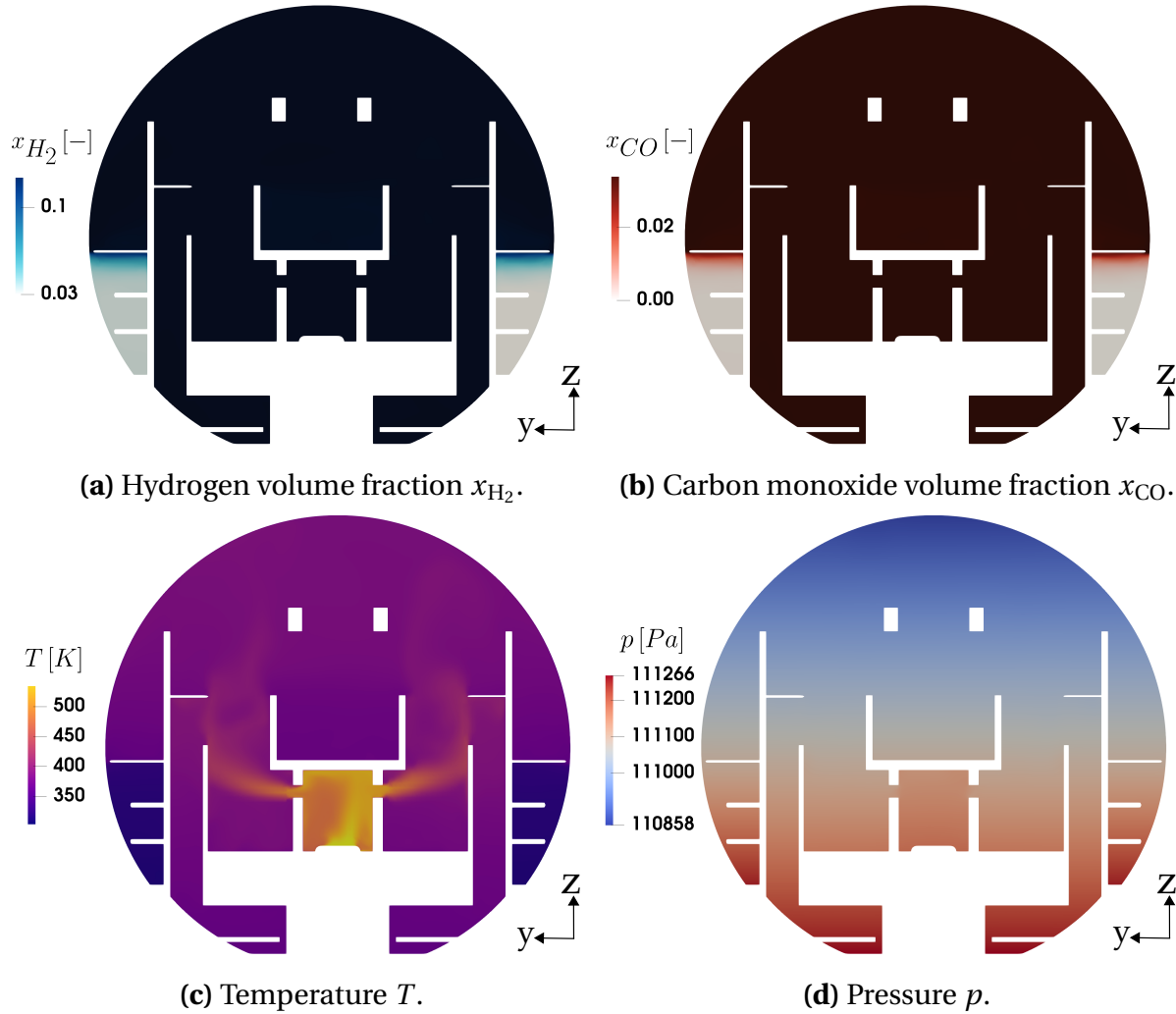


Figure 9.6: Cut-view of the mixture composition and thermodynamic state initial conditions for flame propagation analysis of the Generic Containment case.

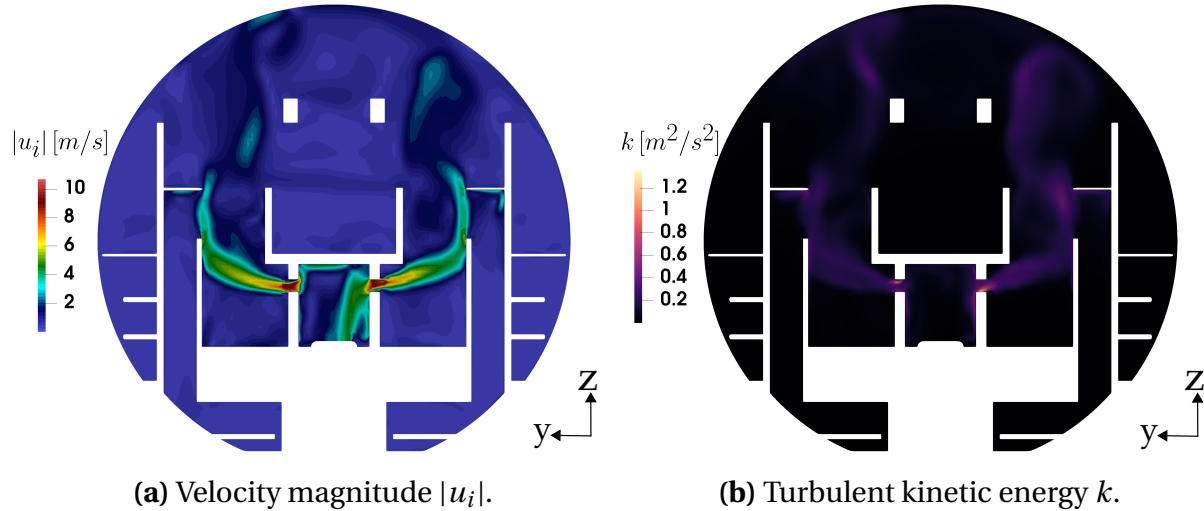


Figure 9.7: Cut-view of the velocity and turbulence initial conditions for flame propagation analysis of the Generic Containment case.

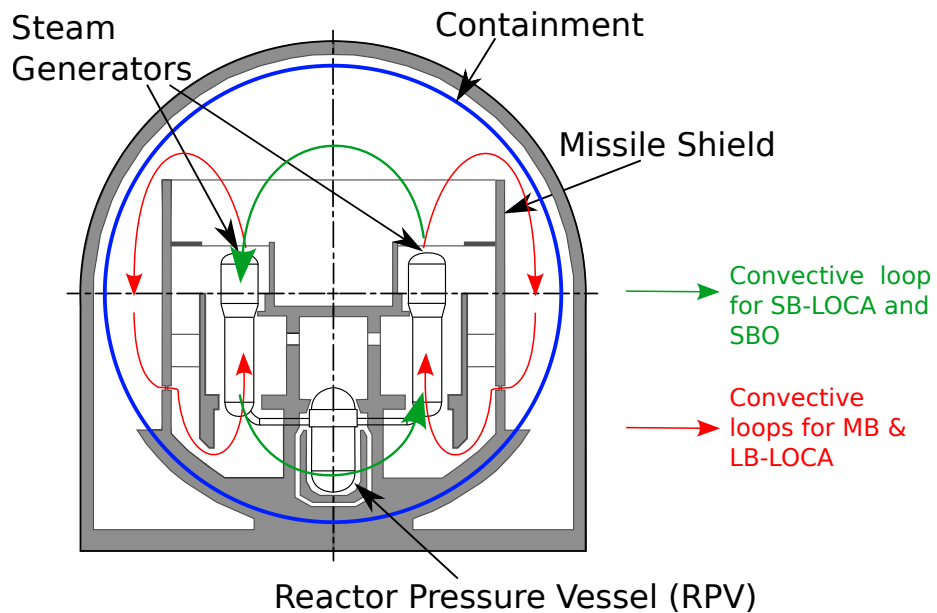


Figure 9.8: Schematic diagram of the Konvoi-type reactor containment showing convective loops in different accident scenarios: a single loop in case of SB-LOCA or SBO and two loops in case of MB- or LB-LOCA.

9.4.2 Ignition location

The flame propagation simulations begin with ignition of the gas mixture at the location in the reactor room (RR), near the top surface of the RPV (Figure 9.9). This location was chosen because of its high temperature and with that related higher likelihood of ignition near a hot surface (Figure 9.6c). Additionally, earlier studies by Manninen et al. (2002), Hasslberger et al. (2017b) and Kim and Hong (2015) have demonstrated a higher flame acceleration potential in parts of the containment with higher degree of confinement (Manninen et al., 2002; Hasslberger et al., 2017b), and with a longer vertical flow path and more complicated geometry along the way (Kim and Hong, 2015). Figure 9.9 shows that the chosen ignition location satisfies all of these criteria.

Figure 9.9 shows the ignition location in the RR compartment and the location of the three pressure probes used in the simulation, while Table 9.3 provides the coordinates of the locations in question. Ignition was achieved in

	Compartment	x [m]	y [m]	z [m]
Ignition	RR	-2.5	0	11
Pressure probe P1	RR	1	0	16
Pressure probe P2	SG left	0	12	16
Pressure probe P3	Dome	0	0	30

Table 9.3: Coordinates of the ignition location and pressure probes (Figure 9.9).

the simulations by switching the regress variable to burned state ($b = 0$) in the first time step of the simulation.

9.5 Computational setup

Boundaries of the computational domain (Figure 9.2) were defined as no-slip, adiabatic, wall boundary conditions on all surfaces. For turbulence quantities, wall functions were used. The numerical method from Chapter 2 was applied, while for sub-grid closure of flame wrinkling, the URANS model for

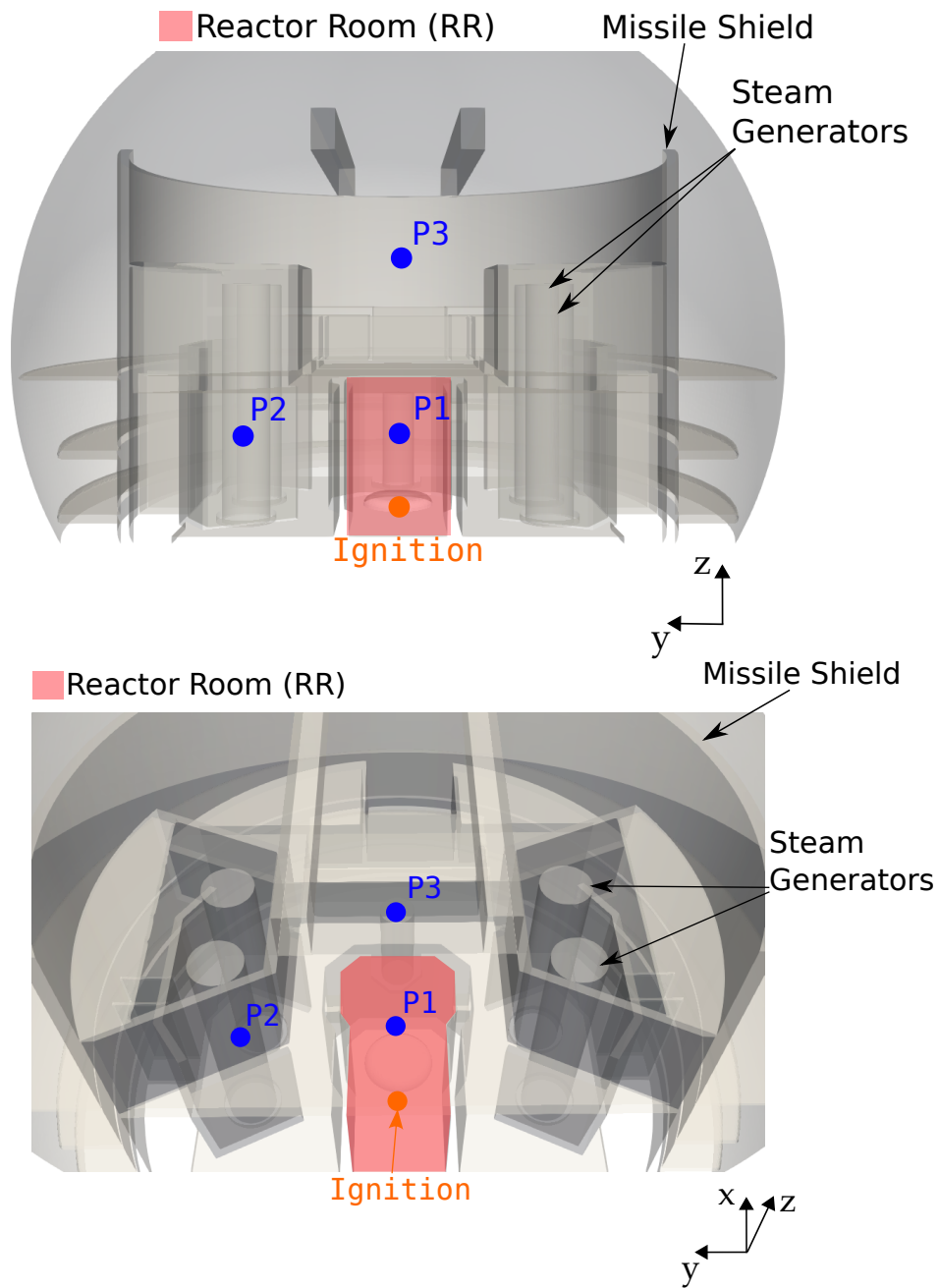


Figure 9.9: Computational domain for the Generic Containment simulations included the entire volume of the simplified containment geometry. Figure shows a 2D and an isometric view of ignition location and pressure probes.

flame instability effects was used as it was defined and validated in Part II. The flame curvature correction factor F_c in Equation 5.14 was derived for hydrogen

fuel. Due to a lack of corresponding experimental data for hydrogen–carbon-monoxide, and due to a relatively low CO content in the mixture (Figure 9.5), the same curvature factor was applied here without modification. The computational setup here was identical with respect to AUSM⁺ up flux scheme coefficients and interpolation schemes to the one used in the validation of the flame wrinkling model in Section 6.1. In the present case, the SAS turbulence model was used (Section 2.3.2). Although the initial conditions contained no significant turbulent intensity, the model was used to calculate the turbulence generated during the flame propagation. Gravitational acceleration was included with the corresponding terms in the momentum and energy equations of the Navier–Stokes equations (Equation 2.1 and 2.7), while radiative heat transfer was not included in the model. Slow flame simulations require longer to reach complete combustion, which can severely impact the required computational cost. In the present work, 3.5 s of physical time at CFL = 1 and with the SSP parameter $m = 3$ took approximately 14 days to complete on a 64-core compute node with two AMD EPYC 7502 32-core CPUs. The domain was discretized with 650 000 polyhedral cells.

9.6 Results

9.6.1 Early phase ($t < 1.3$ s)

The moment of ignition is marked as $t = 0$ s and all results are discussed relative to that moment, starting with the *early phase* of flame propagation, which corresponds to $t < 1.3$ s. In that period, the flame remains fully within the compartments of the inner containment (RR, SG) (Figure 9.1).

The flame starts to propagate in a hemispherical shape immediately after ignition as can be seen for $t = 0.4$ s in Figures 9.11 and 9.14 in which the flame position is defined by the reaction regress variable $b = 0.5$. However, soon thereafter the flame reaches the first obstacle, the wall of the reactor room (RR) compartment.

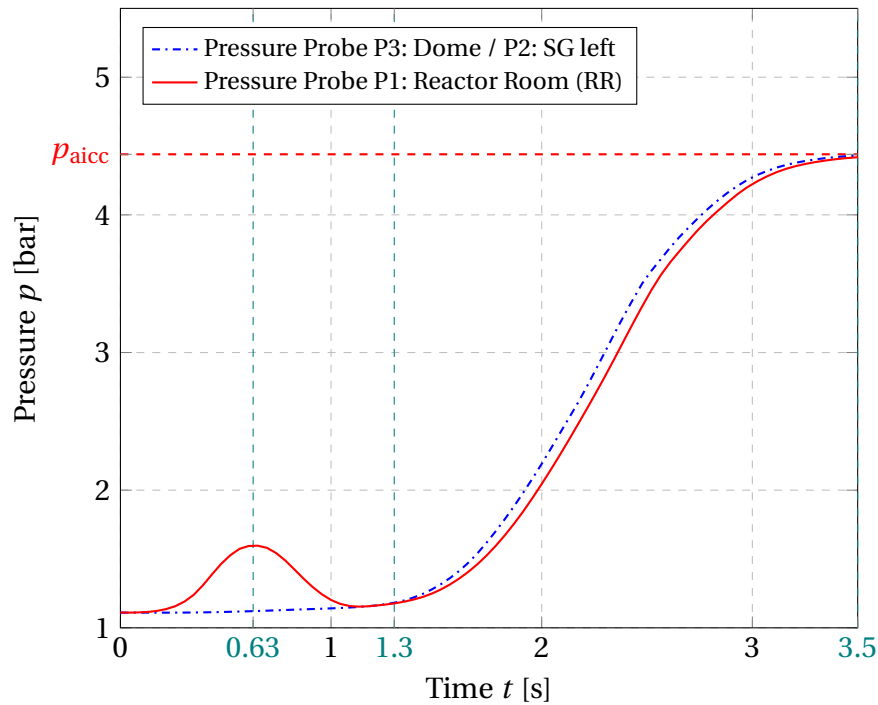


Figure 9.10: Pressure rise results in the containment during the flame propagation. Pressure probe locations are defined in Table 9.3.

Pressure starts to rise in the RR compartment as indicated in the pressure plot in Figure 9.10, causing a flow to emerge through the two narrow ducts connecting the reactor room (RR) to the steam generator (SG) compartments. A relatively narrow duct cross-section means a high degree of confinement of the RR, which causes the pressure in the RR to quickly rise above the one in the SG. In turn, this leads to a formation of high gas velocities (jets) from the ducts into the SG compartment.

By $t = 0.6$ s, the flame had risen to the height of the ducts, where it begins to be advected by the gas jets. A portion of the flame front enters the SG volume in an elongated shape. The flame position snapshots at $t = 0.8$ s show that the flame had reached the top wall of the RR by that moment. Simultaneously the flame propagates further into the SG compartment. Gases pushed in front of the flame that formed a jet from the ducts impinged on the wall behind the steam generators that stands opposite to the ducts (Figure 9.12a). The gas jet is deflected by the wall, generating a radial wall-attached flow running parallel

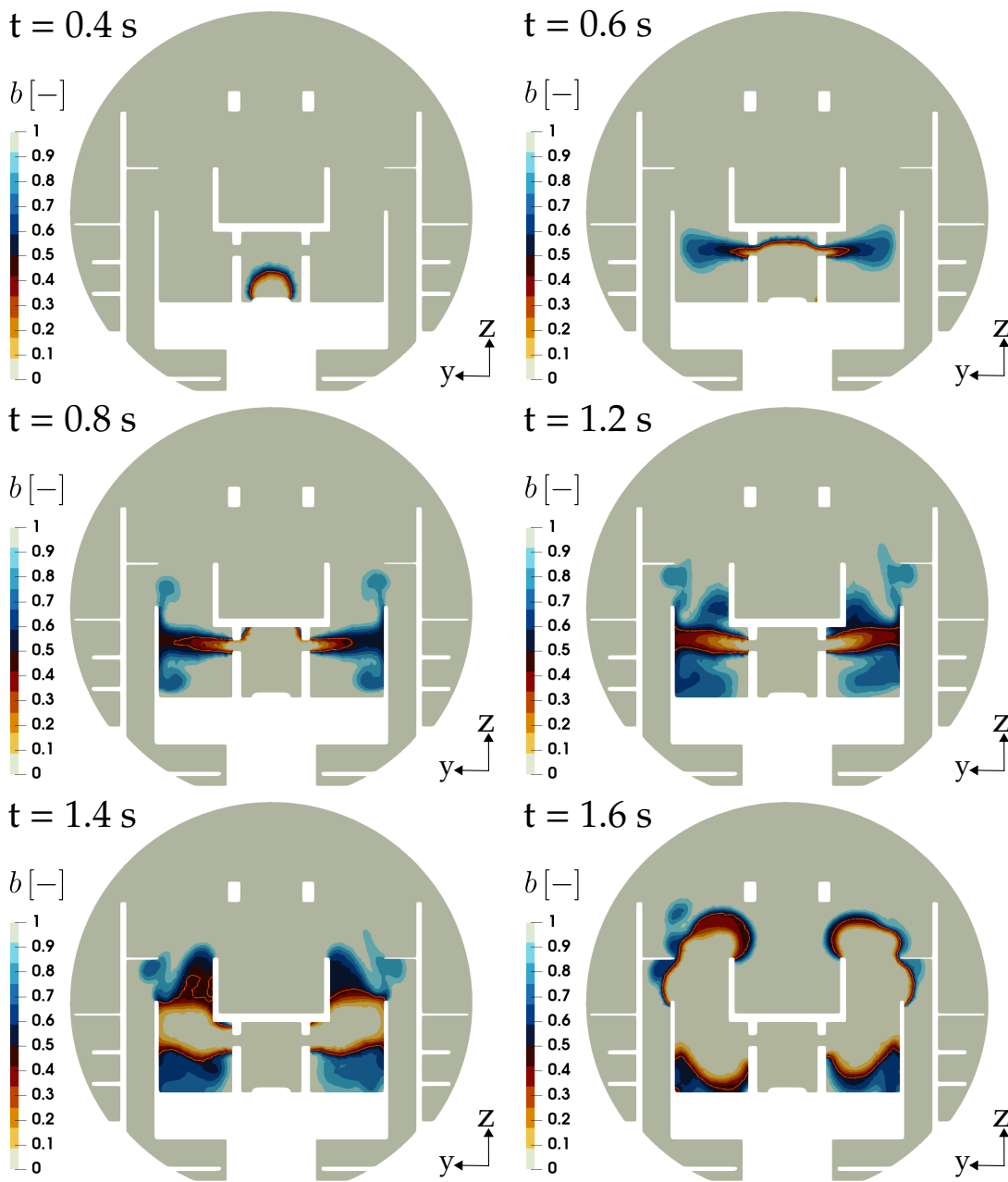


Figure 9.11: 2D cut planes showing the time evolution of the flame position represented by the reaction regress variable (b) fields for the *early phase* of flame propagation ($t < 1.3$ s). The isoline where $b \approx 0.5$ is highlighted in bright orange. The cut planes pass between steam generators and cut through the centerline of the two ducts connecting the RR and SG sections.

to the wall surface. The jet-wall interaction, together with the wall-generated shear stresses in the ducts created a moment of peak turbulence generation in the containment. The turbulent kinetic energy peaks briefly at $k_{\max} \approx 50 \text{ m}^2/\text{s}^2$

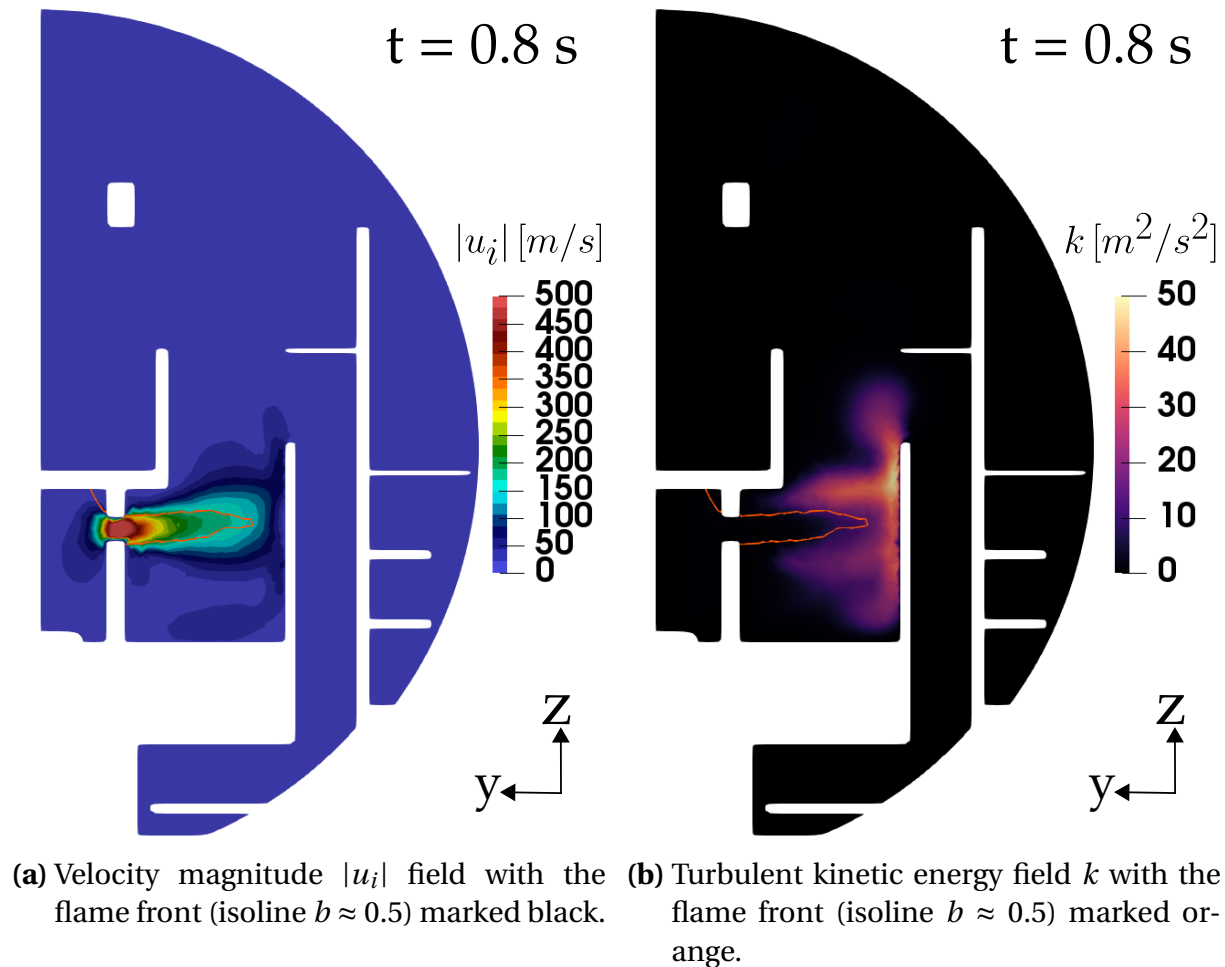


Figure 9.12: Gas jet from the reactor room (RR), right after the peak pressure is reached in that compartment. The flame is elongated by the strong advection. Additionally, turbulence generation is shown by the k field.

in the interval between $t = 0.8 \text{ s}$ and 1 s , dropping sharply to $k_{\max} \approx 27 \text{ m}^2/\text{s}^2$ by $t = 1.2 \text{ s}$. Figure 9.12b shows the k field at $t = 0.8 \text{ s}$, with the flame ($b \approx 0.5$) marked by an orange isoline. Given the importance of turbulence intensity for the development of flame wrinkling and, in turn, flame acceleration, it is important to analyze the turbulence generated in the domain during flame

propagation. Using the turbulent flame speed correlation experimentally derived by Goulier et al. (2017b), appropriate for low turbulence levels in H₂ - CO mixtures (Desclaux et al., 2022), an estimate of the turbulent flame wrinkling Ξ_t can be calculated:

$$\Xi_t = 1.61 \left(\frac{u'_i}{S_1} \right)^{0.526} \left(\frac{r}{L_t} \right)^{0.33} \text{Le}^{-0.14}. \quad (9.1)$$

Given the relationship between fluctuating velocity component u'_i and turbulent kinetic energy k is

$$u'_i = \sqrt{\frac{2}{3}k}, \quad (9.2)$$

using the maximum value for the turbulent kinetic energy on the flame front surface defined by $b \approx 0.5$ at $t = 0.8$ s of

$$\max_{b=0.5} k = 44.5 \left[\frac{\text{m}^2}{\text{s}^2} \right], \quad (9.3)$$

assuming fully developed wrinkling where $\left(\frac{r}{L_t} \right) \rightarrow 0$, and dropping the Lewis number term since the mixture Lewis number $\text{Le} = 1.2$ is greater than unity (> 1) the $\max_{b=0.5} \Xi_t$ estimate becomes

$$\max_{b=0.5} \Xi_t \approx 1.61 \left(\frac{\sqrt{\frac{2}{3} \cdot 44.5}}{0.74} \right)^{0.526} = 4.6. \quad (9.4)$$

The flame speed model used in the simulation accounting for instability-driven (quasi-laminar) wrinkling predicted at the corresponding location of the flame front the maximum value of

$$\max_{b=0.5} \Xi_{\text{inst}} = 4.73 \quad (9.5)$$

The difference between the two values of flame wrinkling is small, with the maximum Ξ_{inst} being slightly higher, meaning that the use of quasi-laminar flame speed model can be considered sufficiently conservative in this case. Results show that the generated turbulence remains too low to drive flame acceleration. However, due to coarse grid resolution it is likely that the simulation was not able to sufficiently resolve the turbulence generation. A more

detailed CFD study focusing on the jet-like flow from RR into the SG compartments would be necessary to further investigate the turbulence levels.

Narrow cross section of the ducts and strong gas flow (jets) make the flame assume an elongated tube-like shape, while advection pushes the flame toward the wall opposite to the ducts. After the flame impacts the wall it starts to propagate both upward and downward inside the SG compartment. However, due to buoyancy, the stronger propagation direction is upward. The flame almost entirely envelops the steam generators by $t = 1.3$ s. After that, it leaves the inner containment section (RPV, RR, SG) and enters the dome area as is shown in Figures 9.11 and 9.14.

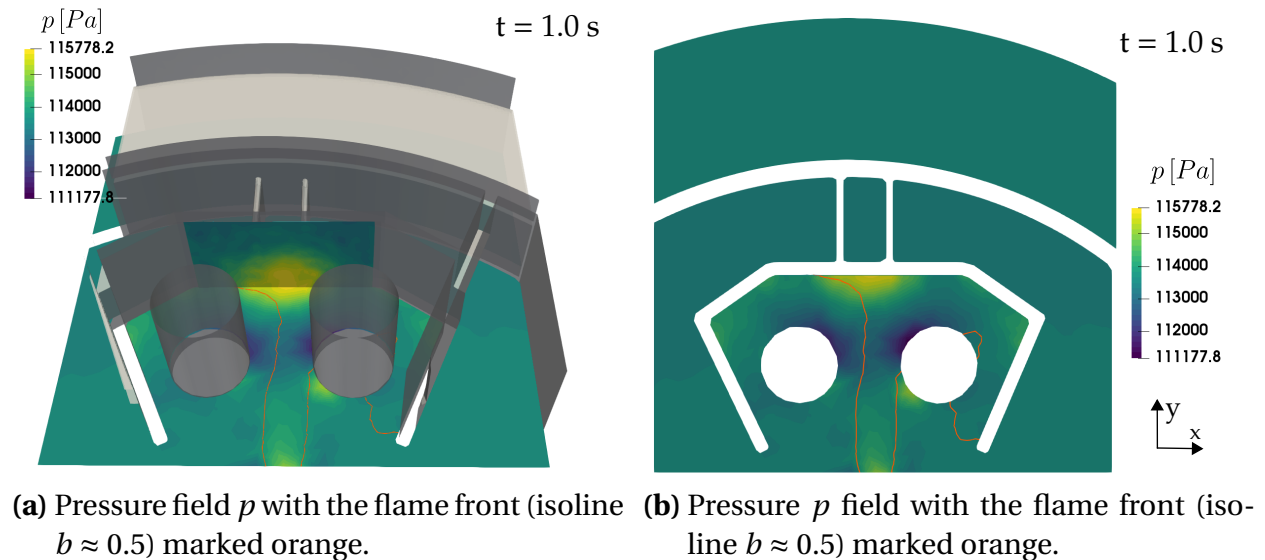


Figure 9.13: Pressure field p on the location of gas jet impingement on the wall behind the steam generators shows a moderate overpressure on the impacted side of approx. 2000 Pa.

The reaction regress (b) fields in Figure 9.11 suggest that, due to higher gas velocities and possibly, in a smaller degree, due to some diffusion by the generated turbulence, the b field becomes more spread out in the timesteps where high gas velocity is present ($t \approx 0.6$ s - 1.6 s), while the b gradient is fairly steep otherwise ($t < 0.4$ s or $t > 1.6$ s), with the flame front remaining thin.

Pressure rise in the reactor room (RR) is plotted in Figure 9.10 relative to the pressure rise in the containment dome (Dome) and the left steam generator

(SG left). The RR compartment experiences a quick initial rise in pressure, but as the available uncombusted gas in the RR gets diminished, the pressure starts to drop after peaking at ≈ 1.6 bar at $t = 0.63$ s. At that moment, the flame front already exited the RR compartment and propagates through the steam generator (SG) section.

Gas explosions are able to potentially generate strong local pressure maxima, sometimes referred to as blast waves. Even in cases of slow deflagrations that do not generate high enough pressures to endanger the integrity of the containment, local pressure and temperature loads could still damage various equipment installed in the containment. In the case analyzed here, the pressure rise is gradual in the containment volume given that the flame speed remains in the deflagration regime. Figure 9.13 shows that the gas jet impinging on the wall behind the steam generators results in only a moderate maximum overpressure on the impacted side of 2278 Pa. The maximum thermal load on the surfaces is equal to the adiabatic flame temperature of the mixture of approx. 2200 K.

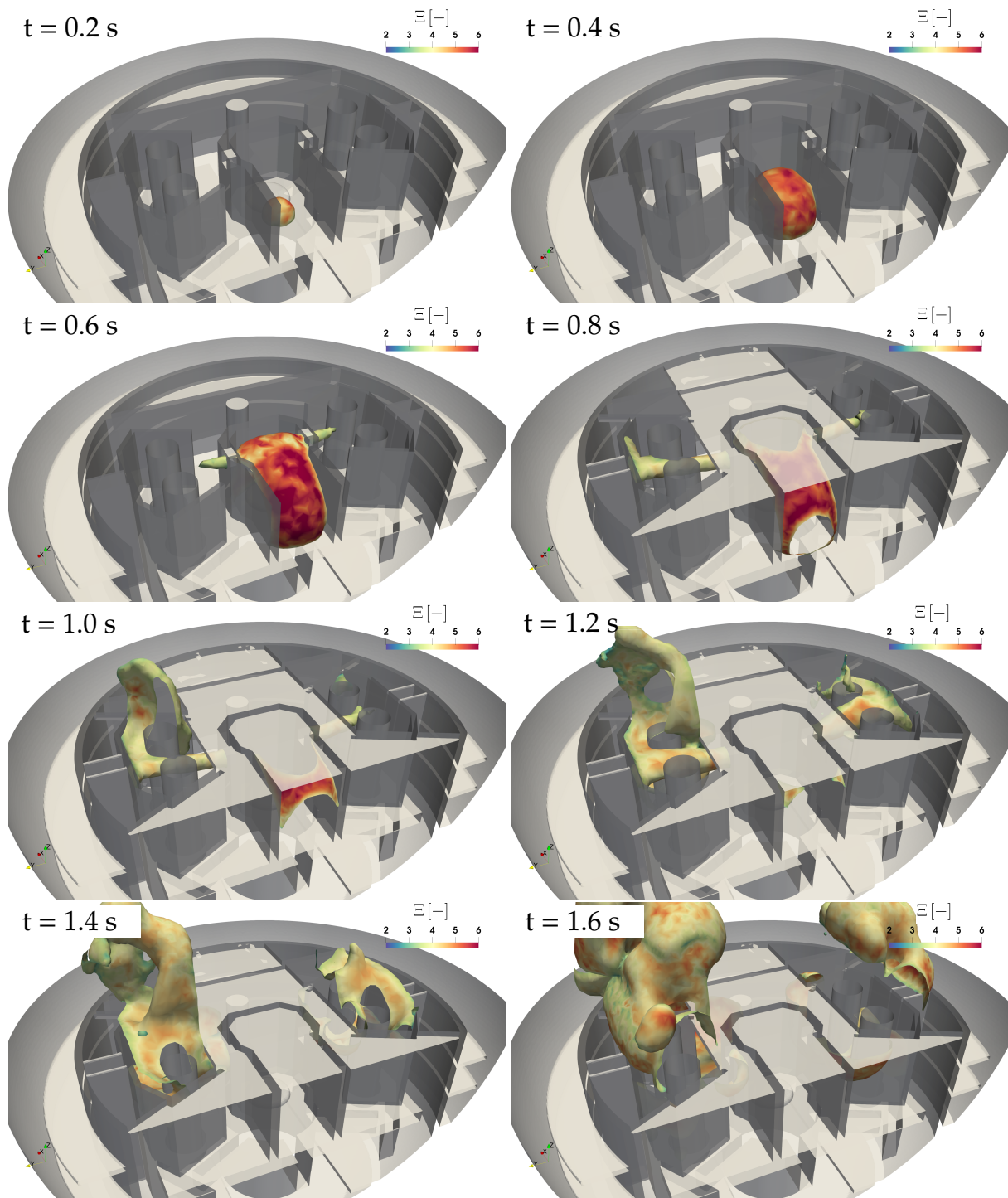


Figure 9.14: Time evolution of the flame position represented by the isosurface of the flame regress variable $b \approx 0.5$. The field Ξ shows the flame wrinkling factor.

9.6.2 Late phase ($t > 1.3$ s)

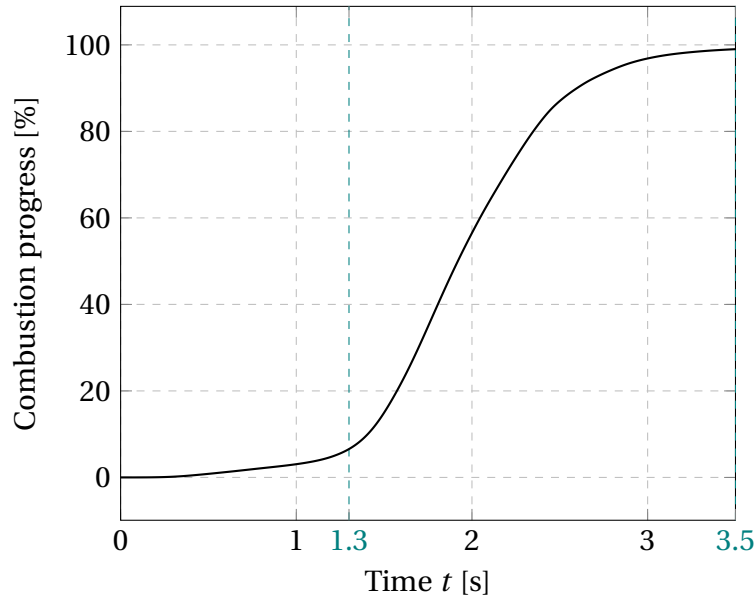


Figure 9.15: Overall combustion progress tracked as total combusted volume in the domain.

The second, *late phase* of flame propagation begins with the flame exiting the compartments of the inner containment (RR and SG) and entering the dome section at approximately $t = 1.3$ s. This moment corresponds with the inflection point in the overall combustion progress when the consumption rate of unburnt mixture rapidly speeds up as shown in Figure 9.15. By entering the dome section, the flame surface is able to rapidly expand due to no longer being confined by the walls, as was the case inside the inner containment. At the moment of the inflection point in the overall combustion progress, the pressure starts to rise rapidly such that the initial overpressure doubles by $t = 2$ s (Figure 9.10). At that moment, approximately 35% of the flammable mixture is combusted (Figure 9.15). In the next 0.5 s the combusted volume percentage increases rapidly to 80%. Simulation results show that after $t = 1.3$ s pressure rises slightly slower in the RR in comparison to other compartments. The reason is that, at that stage, the rise in pressure is driven by the combustion in the outer containment, while the RR gets pressurized via two ducts connecting it to the SG, through which a gas flow into the RR emerges.

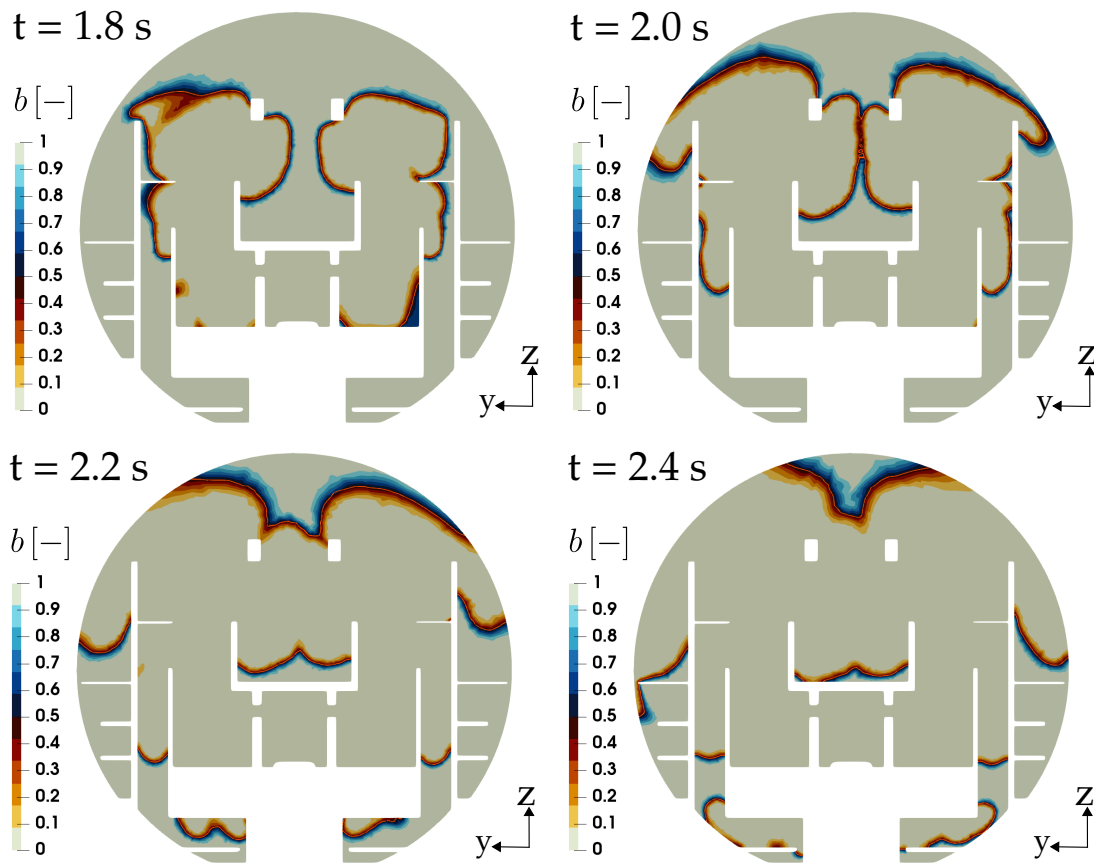


Figure 9.16: Time evolution of the b fields for the *late phase* of flame propagation ($t > 1.3$ s). The $b \approx 0.5$ isoline is highlighted in bright orange. The cut planes pass between steam generators and cut through the centerline of the two ducts connecting the RR and SG sections.

Flame position results (Figures 9.16 and 9.17) show dominantly upward propagation direction after the flame leaves the inner containment and enters the dome. At first, two parallel flame structures emerge simultaneously from the two steam generator sections (SG left and SG right), which connect in the centerline of the dome at approx. $t = 2.0$ s. The flame speed is reduced when the flame leaves the more confined, inner part of the containment, a behavior that corresponds with other studies of PWR containments with large free volumes (Kim and Hong, 2015; Hasslberger et al., 2017b). However, looking at the integral value of the combustion progress, defined as the ratio of total combusted

volume in the containment, the rate of combustion in the containment increases at that same moment due to rapid growth of the flame surface. The flame position results at $t = 1.8$ s show that, after propagating upwards and reaching the top edge of the missile shield and the crane-mounting structure, a branch of the flame bends downwards and enters the area behind the missile shield. Simultaneously, the upward propagation continues and the flame reaches the top of the containment around $t = 2.6$ s.

At the moment when the simulation ended ($t = 3.5$ s), the complete combustion of the flammable gases has been reached (Figure 9.15), while the pressure peaked at the adiabatic isochoric complete combustion pressure p_{aicc} , which is the final theoretical point of a closed-volume combustion with adiabatic boundary conditions.

Over the course of the entire process of flame propagation, the predicted flame wrinkling Ξ does not reach a level that could potentially result in either a fast deflagration (flame propagating at sonic speed) or DDT. The flame speed in the unburned gas frame of reference, sometimes called fundamental flame speed, e.g. by Beccantini and Studer (2010), peaks at

$$\max(S_{\text{eff}}) = \Xi_{\text{max}} \cdot S_1 = 17.8 \cdot 0.74 = 13.2 \frac{\text{m}}{\text{s}}, \quad (9.6)$$

while the observable flame speed estimate – in the fixed coordinate system – peaks in the gas jet at $V_{\text{max}} = 456.7$ m/s, which is insufficient to cause shock-flame coupling as a mechanism of DDT initiation, given that the Chapman–Jouguet (CJ) detonation velocity of the mixture (Table 9.2) is $V_{\text{CJ}} \approx 1712$ m/s. Although it is not possible to generally define the conditions for the onset of DDT, in e.g. smooth tubes, a deflagration is required to accelerate at least to approximately half of the CJ detonation velocity (in a fixed coordinate system) to result in the onset of detonation (Lee, 2008).

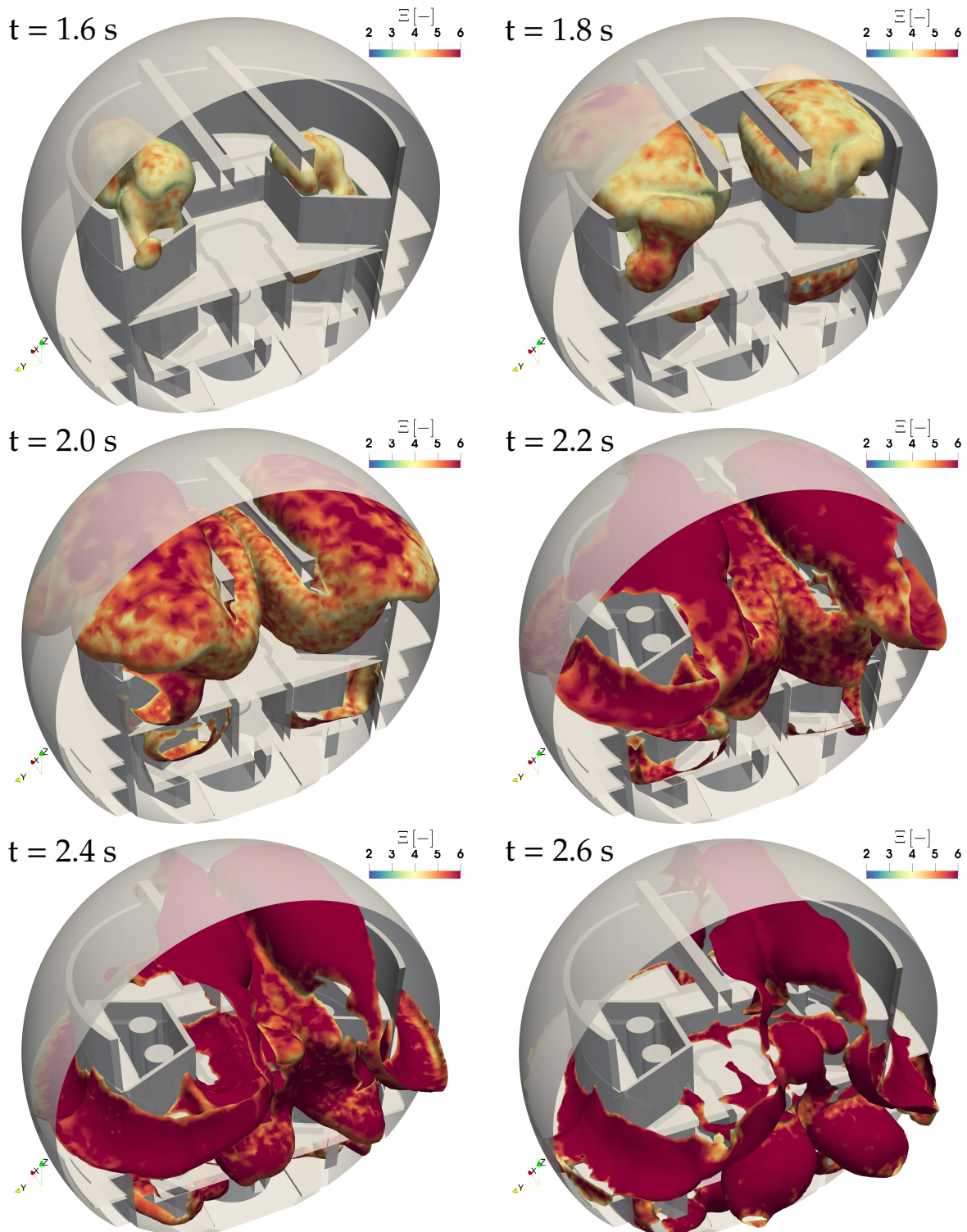


Figure 9.17: Time evolution of the flame position represented by the isosurface of the flame regress variable $b \approx 0.5$. The field Ξ shows the flame wrinkling factor.

10 Concluding remarks

Part III demonstrated an analysis of the SB–LOCA accident scenario consisting of the combined workflow where prior results from mixture formation analyses using LP (COCOSYS) and CFD (*containmentFoam*) tools were used to initialize a combustion CFD methodology developed in Parts I and II of the present work. The integrated analysis chain was able to generate new insights about the potential consequences of the reactor accident in question. Moreover, CFD simulations with *containmentFoam* were used for the first time on the full reactor containment scale to provide a realistic estimate on the turbulence level, gas composition fields and convective flow patterns, which provided detailed initial conditions for the subsequent flame propagation CFD analysis.

Combustion simulations were performed using the numerical method described in Part I and due to nearly-quiescent initial conditions only the instability-driven flame wrinkling was modeled using the scale-adaptive flame speed closure developed in Part II. The combustion analysis of the SB–LOCA accident in the Generic Containment provided results for the main integral variables of interest such as the pressure rise transient, the overall combustion rate, as well as the maximum flame speeds reached. Detailed study of significant local flow structures was also made possible, such as the gas jet forming at the exit of the reactor room (RR), or the multiple flame paths that were discovered in the CFD results.

A phenomenon observed in other PWR reactor type containments where the observable flame speed drops after the flame leaves a more confined inner part of the containment was reproduced in the present work as well. Additionally, it was shown that this drop in flame speed does not equal to a lower overall combustion rate since the flame surface expands more rapidly in lack of

confinement, which increases the rate of combustion measured by total combusted volume.

The combustion CFD simulation predicted turbulence generation, mostly in areas of high gas velocity, although the turbulence intensity did not reach a level which could significantly increase the flame wrinkling, which was estimated using the turbulent flame correlation by Goulier et al. (2017b). However, it is likely that the coarse mesh used in the present study is insufficient to resolve shear stresses in the jet flow or near-wall boundary layers, potentially resulting in turbulence underprediction. Therefore, a detailed simulation of the duct jet flow is proposed for future work.

The combustion regime with respect to flame speed in the analyzed accident scenario can be characterized as a slow deflagration (sometimes called "slow burn" in the nuclear safety literature) since no fast flames or DDT criteria have been reached.

Part IV

Conclusion

11 Summary

The topic of numerical method development for combustion simulation at large scales was explored in the present work, the motivation for which originated from flame propagation problems in nuclear safety, where premixed gas explosions pose a concern in case of severe reactor accidents. The summary of the main findings will be presented in the following.

The density-based numerical method for transient compressible reacting flow presented in Chapter 2, based on explicit time integration with Strong Stability Preserving (SSP) Runge–Kutta scheme is shown to allow an increase in computation stability for cases where conventional methods are more strongly limited by the allowable maximum CFL condition. This applies to cases both with and without sharp discontinuities (e.g. shock, flame front). By enabling stable computation of flame propagation cases in present work at $CFL = 1$, which is required for time-accurate resolution of the transient physical phenomena of accelerating flames, the numerical method improved the efficiency of the simulations in comparison to, e.g. method used in work by Ettner (2013) or Hasslberger (2017), where the maximum CFL in reacting flow had to be limited to $CFL < 0.3$ for reasons of stability.

Spatial discretization by an all-speed high-resolution scheme AUSM⁺up, together with the robust SSP time integration enabled the developed density-based numerical method to avoid being limited to only one of the flame propagation regimes of interest to explosion safety, which is one of the main requirements for simulation codes in the field (as discussed in more detail in Section 1.2.2). Furthermore, the numerical method avoids the need for ad-hoc switching between pressure-based and density-based solution frameworks which would introduce a reliance on arbitrary stopping criteria, dependence on user judgment and manual intervention, increasing the overall uncertainty of the solution. The method presented in Part I is a step toward the goal of

unified modeling of the complete temporal evolution of the explosion event from ignition to detonation. Validation was first carried out at laboratory-scale (Chapter 3), using experimental results of spherical hydrogen flame propagation at controlled turbulence levels and lean stoichiometries. Validation simulations show good prediction of flame speed and pressure rise under conditions relevant to reactor safety research.

In Part II of the thesis, a sub-grid RANS modeling approach for instability effects on hydrogen–air flames was introduced. It consists of a scale-adaptive, fractal-based flame speed closure for the Darrieus–Landau instability. A number of factors for small-scale effects are incorporated into the model as well, such as the thermal–diffusive instability, local flame curvature and pressure, which are all important when considering lean hydrogen–air mixtures. The new model proposed here is aiming to address a lack of suitable models for the quasi-laminar flames occurring especially in early stages of industrial explosions, as was detailed in Chapter 4. The advantage of the RANS model is that it allows for industrial-scale explosion simulation without prohibitive computational cost. Validation was performed using the results of large-scale experiments conducted under conditions of negligible turbulence and in presence of gravitational effects (Chapter 6). Additionally, validation was performed using coarse grids where the grid spacing is several orders of magnitude larger than the laminar flame thickness. Such grids are a necessity for modeling large-scale volumes in industrial applications. Furthermore, the model formulation is not limited by the flame shape nor it requires a global flame front radius as an input parameter.

Finally, Part III demonstrated an application of the developed numerical simulation method to the flame propagation analysis in a full-scale reactor containment undergoing a severe accident. Considerable challenges remain in the attempts to efficiently model large-scale combustion and not many CFD studies of real-scale containments have been published in the literature, an overview of which was given in Section 8.1. While many of the cited studies impose various assumptions that resulted in conservative estimates for the combustion scenarios, a particular focus in the present work was on generating as realistic initial conditions as possible using simulations of thermal-

hydraulic phenomena in the containment prior to ignition, which included the prediction of turbulence intensity. Furthermore, by initializing the flame propagation CFD solver with the results of gas distribution simulations from dedicated tools, the combustion numerical method was effectively integrated into the reactor accident analysis chain. According to the results of the flame propagation simulation performed in the present work, the particular scenario of an SB-LOCA investigated here did not produce flame acceleration sufficient for DDT in the containment volume.

12 Outlook

A number of possible avenues for further research are open for potential continuation of the present work, some of which will be suggested in the following.

The results in Section 2.5.1 and Section 3.6 have shown that the number of SSP time integration stages (m in Equation 2.74) is a parameter which can be adjusted to increase the stability of the numerical solution method when needed, or otherwise be set for optimal efficiency. Currently, the number of stages is set by the user in the simulation setup configuration files, with an option of manual modification during the simulation runtime. An adaptive algorithm that would dynamically adjust the parameter to an optimal value while the simulation is running could further improve the efficiency of the method.

The flame speed closure for instability-driven flames derived in Chapter 5 is valid for initial flame propagation in quiescent mixtures characterized by negligible turbulence intensity, while turbulent flame speed correlations, e.g. by Dinkelacker et al. (2011) or Goulier et al. (2017b), are developed for fully-developed turbulent flames. Given that real-world applications of accelerating flames may include complex geometry where the flame initially propagates in a quasi-laminar regime, but can also encounter a region of significant turbulence generation, a coupling strategy for blending the different models may be important for industrial applications. Coupling can be achieved by implementing the theoretical criteria, e.g. by Chaudhuri et al. (2011) or Chomiak and Lipatnikov (2023) directly in the code, which would locally (on the level of an individual grid cell) apply the correct implementation. Alternatively, a conservative approach could involve taking the maximum of the two, i.e. $\max(\Xi_{\text{DL}}, \Xi_{\text{turb}})$ in Equation 2.24.

Correlation for the effect of small-scale curvature on flame wrinkling defined in Equation 5.14 (Section 5.2) has been experimentally derived by Katzy (2021) for lean hydrogen flames. Simulation setup in the Konvoi containment analysis (Section 9.5) used the unmodified Equation 5.14 on the account of the unburned gas composition consisting primarily of hydrogen, while the influence of the small ratio of carbon-monoxide in the mixture was neglected (Section 9.4). However, the potential effect of gradual addition of carbon-monoxide on the small-scale flame curvature could be investigated in a similar experimental study to the one by Katzy (2021) for hydrogen-air mixtures.

Models used for efficient numerical simulations rely on the availability of input data in a few key aspects. For example, reaction rate closure with an imposed laminar flame speed enables the one-step chemistry modeling. The needed input can come from experimental measurements or calculated using highly-resolved 1D simulations of geometrically simple flame configurations (e.g. planar flames) with detailed chemistry. Although such a practice is widely used in combustion modeling in general, gas mixtures that emerge in a reactor containment undergoing a severe accident pose a specific challenge. Combustion of hydrogen with some admixture of carbon-monoxide with very high steam dilution and non-standard (elevated) pressures (1.5–2 bar) and temperatures (75–300 °C) is unique to the domain of reactor safety and the required input data usually needs to be specifically derived for that application. Low availability of input data results in a high modeling uncertainty and further work is required. All of the combustion modeling in the present work and, to the best of author’s knowledge, elsewhere in the literature, were based on combustion in standard air, while reduced oxygen conditions that can emerge as a result of PARs operation (Klauck et al., 2021), have not yet been investigated.

Atmosphere inside a reactor containment during an accident can include a significant amount of water droplets, either injected as spray from installed sprinklers, or as a result of partial condensation (Bentaïb et al., 2015). Physics of water spray, turbulence and flame interactions is complex (Boeck et al., 2015), and a sub-grid model has not yet been developed which could be used in an efficient CFD approach and applied for large-scale nuclear safety simulations.

The simulations in Section 6.4 showed that radiative heat transfer can play a significant role in safety-relevant combustion, in particular for accurate prediction of peak pressure as well as pressure drop after the combustion is complete. In the present work, the DOM radiation model was used. However, a potentially more computationally efficient radiation modeling approach could be investigated, e.g. based on a Monte Carlo method (Liu et al., 2022; Kapulla et al., 2023).

One of the purposes of consequence analysis with respect to explosion safety is the assessment of potential damage caused by pressure impulses generated by the combustion. A straightforward extension of the deterministic safety analysis methodology would be developing a Fluid–Structure Interaction (FSI) simulation tool by coupling the combustion CFD developed in the present work to a structural mechanics numerical simulation code.

Bibliography

- Allelein, H., Fischer, K., Vendel, J., Malet, J., Studer, E., Schwarz, S., Houkema, M., Paillere, H. and Bentaïb, A. (2007), International standard problem ISP-47 on containment thermal hydraulics, *NEA News* **25**(2), 28.
- Allelein, H.-J., Arndt, S., Klein-Hessling, W., Schwarz, S., Spengler, C. and Weber, G. (2008), COCOSYS: Status of development and validation of the German containment code system, *Nuclear Engineering and Design* **238**(4), 872–889.
- Altantzis, C., Frouzakis, C. E., Tomboulides, A. G. and Boulouchos, K. (2015), Direct numerical simulation of circular expanding premixed flames in a lean quiescent hydrogen-air mixture: Phenomenology and detailed flame front analysis, *Combustion and Flame* **162**(2), 331–344.
- Altantzis, C., Frouzakis, C., Tomboulides, A. and Boulouchos, K. (2013), Numerical simulation of propagating circular and cylindrical lean premixed hydrogen/air flames, *Proceedings of the Combustion Institute* **34**(1), 1109–1115.
- Altantzis, C., Frouzakis, C., Tomboulides, A., Kerkemeier, S. and Boulouchos, K. (2011), Detailed numerical simulations of intrinsically unstable two-dimensional planar lean premixed hydrogen/air flames, *Proceedings of the Combustion Institute* **33**(1), 1261–1268.
- Arntzen, B. J. (1998), *Modelling of turbulence and combustion for simulation of gas explosions in complex geometries*, PhD thesis, Norwegian University of Science and Technology (NTNU).

- Aung, K., Hassan, M. and Faeth, G. (1997), Flame stretch interactions of laminar premixed hydrogen/air flames at normal temperature and pressure, *Combustion and Flame* **109**(1-2), 1–24.
- Baraldi, D., Heitsch, M. and Wilkening, H. (2007), CFD simulations of hydrogen combustion in a simplified EPR containment with CFX and REACFLOW, *Nuclear Engineering and Design* **237**(15-17), 1668–1678.
- Barfuss, C., Heilbronn, D. and Sattelmayer, T. (2019), Simulation of deflagration-to-detonation transition of lean H₂-CO-air mixtures in obstructed channels, *8th International Conference on Hydrogen Safety (ICHS)*, Adelaide, Australia.
- Bauwens, C. R., Bergthorson, J. M. and Dorofeev, S. B. (2015), Experimental study of spherical-flame acceleration mechanisms in large-scale propane-air flames, *Proceedings of the Combustion Institute* **35**(2), 2059–2066.
- Bauwens, C. R. L., Bergthorson, J. M. and Dorofeev, S. B. (2017), Experimental investigation of spherical-flame acceleration in lean hydrogen-air mixtures, *International Journal of Hydrogen Energy* **42**(11), 7691–7697.
- Beccantini, A. and Studer, E. (2010), The reactive Riemann problem for thermally perfect gases at all combustion regimes, *International Journal for Numerical Methods in Fluids* **64**(3), 269–313.
- Bechtold, J. K. and Matalon, M. (2001), The dependence of the Markstein length on stoichiometry, *Combustion and Flame* **127**(1), 1906–1913.
- Becker, T. and Ebert, F. (1985), Vergleich zwischen Experiment und Theorie der Explosion großer, freier Gaswolken, *Chemie Ingenieur Technik* **57**(1), 42–45.
- Bentaïb, A., Bleyer, A., Meynet, N., Chaumeix, N., Schramm, B., Höhne, M., Kostka, P., Movahed, M., Worapittayaporn, S., Brähler, T. et al. (2014), SAR-NET hydrogen deflagration benchmarks: Main outcomes and conclusions, *Annals of Nuclear Energy* **74**, 143–152.
- Bentaïb, A., Meynet, N. and Bleyer, A. (2015), Overview on hydrogen risk research and development activities: methodology and open issues, *Nuclear Engineering and Technology* **47**(1), 26–32.

- Berger, L., Attili, A. and Pitsch, H. (2022a), Intrinsic instabilities in premixed hydrogen flames: Parametric variation of pressure, equivalence ratio, and temperature. Part I - Dispersion relations in the linear regime, *Combustion and Flame* **240**, 111935.
- Berger, L., Attili, A. and Pitsch, H. (2022b), Intrinsic instabilities in premixed hydrogen flames: parametric variation of pressure, equivalence ratio, and temperature. Part II - Non-linear regime and flame speed enhancement, *Combustion and Flame* **240**, 111936.
- Berger, L., Grinberg, M., Jürgens, B., Lapenna, P. E., Creta, F., Attili, A. and Pitsch, H. (2023), Flame fingers and interactions of hydrodynamic and thermodiffusive instabilities in laminar lean hydrogen flames, *Proceedings of the Combustion Institute* **39**(2), 1525–1534.
- Berger, L., Kleinheinz, K., Attili, A. and Pitsch, H. (2019), Characteristic patterns of thermodiffusively unstable premixed lean hydrogen flames, *Proceedings of the Combustion Institute* **37**(2), 1879–1886.
- Bielert, U., Breitung, W., Kotchourko, A., Royl, P., Scholtyssek, W., Vesper, A., Beccantini, A., Dabbene, F., Paillere, H., Studer, E., Huld, T., Wilkening, H., Edlinger, B., Poruba, C. and Mohaved, M. (2001), Multi-dimensional simulation of hydrogen distribution and turbulent combustion in severe accidents, *Nuclear Engineering and Design* **209**(1), 165–172.
- Blinnikov, S. I. and Sasorov, P. V. (1996), Landau-Darrieus instability and the fractal dimension of flame fronts, *Phys. Rev. E* **53**, 4827–4841.
- Boeck, L., Kink, A., Oezdin, D., Hasslberger, J. and Sattelmayer, T. (2015), Influence of water mist on flame acceleration, DDT and detonation in H₂-air mixtures, *International Journal of Hydrogen Energy* **40**(21), 6995–7004. Publisher: Elsevier.
- Bönigke, G., Ewig, F., Friedrichs, H., Heitsch, M., Hüttermann, B., Jendrich, U., Meier, S., Scharfe, A., Sonnenkalb, M. and Rohde, J. (1998), Contributions to elaboration of concept and measures for optimized management of

- beyond-design-basis accidents in German LWR power plants; Untersuchungen von Maßnahmen des anlageninternen Notfallschutzes zur Schadensbegrenzung für LWR, *Technical Report GRS-A-2601*, GRS.
- Bradley, D., Cresswell, T. and Puttock, J. (2001), Flame acceleration due to flame-induced instabilities in large-scale explosions, *Combustion and Flame* **124**(4), 551–559.
- Bradshaw, P., Ferriss, D. H. and Atwell, N. P. (1967), Calculation of boundary-layer development using the turbulent energy equation, *Journal of Fluid Mechanics* **28**(3), 593–616. Publisher: Cambridge University Press.
- Bray, K. and Libby, P. A. (1986), Passage times and flamelet crossing frequencies in premixed turbulent combustion, *Combustion Science and Technology* **47**(5-6), 253–274.
- Bray, K. and Moss, J. (1977), A unified statistical model of the premixed turbulent flame, *Acta Astronautica* **4**(3-4), 291–319.
- Breitung, W., Chan, C., Dorofeev, S., Eder, A., Gerland, B., Heitsch, M., Klein, R., Malliakos, A., Shepherd, J. and Studer, E. (2000), Flame acceleration and deflagration-to-detonation transition in nuclear safety, *Organisation for Economic Co-operation and Development, Paris, France, Technical Report No. NEA/CSNI*.
- Breitung, W. and Royl, P. (2000), Procedure and tools for deterministic analysis and control of hydrogen behavior in severe accidents, *Nuclear Engineering and Design* **202**(2-3), 249–268.
- Bychkov, V. and Liberman, M. A. (2000), Dynamics and stability of premixed flames, *Physics Reports* **325**(4-5), 115–237.
- Cai, X., Wang, J., Bian, Z., Zhao, H., Dai, H. and Huang, Z. (2020), On transition to self-similar acceleration of spherically expanding flames with cellular instabilities, *Combustion and Flame* **215**, 364–375.
- Chakraborty, A. (2020), *Optimization of passive autocatalytic recombiners (PARs) with respect to gas-phase ignition*, Dissertation, Rheinisch-Westfälische Technische Hochschule (RWTH) Aachen, Aachen.

- Chakraborty, N. and Cant, R. S. (2011), Effects of Lewis number on flame surface density transport in turbulent premixed combustion, *Combustion and Flame* **158**(9), 1768–1787.
- Chase, M. W. (1998), *NIST-JANAF thermochemical tables*, Vol. 9, American Chemical Society Washington, DC.
- Chaudhuri, S., Akkerman, V. and Law, C. K. (2011), Spectral formulation of turbulent flame speed with consideration of hydrodynamic instability, *Physical Review E* **84**(2), 026322.
- Chomiak, J. and Lipatnikov, A. N. (2023), Simple criterion of importance of laminar flame instabilities in premixed turbulent combustion of mixtures characterized by low Lewis numbers, *Phys. Rev. E* **107**, 015102.
- Creta, F., Fogla, N. and Matalon, M. (2011), Turbulent propagation of premixed flames in the presence of Darrieus–Landau instability, *Combustion Theory and Modelling* **15**(2), 267–298.
- Creta, F., Lapenna, P. E., Lamioni, R., Fogla, N. and Matalon, M. (2020), Propagation of premixed flames in the presence of Darrieus–Landau and thermal diffusive instabilities, *Combustion and Flame* **216**, 256–270.
- Creta, F. and Matalon, M. (2011), Propagation of wrinkled turbulent flames in the context of hydrodynamic theory, *Journal of Fluid Mechanics* **680**, 225–264.
- Cutrono Rakhimov, A., Visser, D. C., Holler, T. and Komen, E. M. J. (2017), The role of CFD combustion modelling in hydrogen safety management – VI: Validation for slow deflagration in homogeneous hydrogen-air-steam experiments, *Nuclear Engineering and Design* **311**, 142–155.
- Darwish, M., Mangani, L. and Moukalled, F. (2016), *The finite volume method in computational fluid dynamics: an advanced introduction with OpenFOAM and MATLAB*, Springer Cham.
- Daudey, N. and Champassith, A. (2014), Accidental hydrogen release inside a nuclear power plant: CFD modelling and consequence analysis, *10th In-*

- ternational Symposium on Hazards, Prevention and Mitigation of Industrial Explosions (ISHPMIE)*, Bergen, Norway.
- Desclaux, A., Idir, M., Comandini, A., Bleyer, A., Bentaïb, A. and Chaumeix, N. (2022), Experimental study on turbulent flame speed of H₂-CO/air mixtures relevant to late phase accident scenario, *International Colloquium on the Dynamics of Explosions and Reactive Systems (ICDERS)*, Naples, Italy.
- Dimmelmeier, H., Eyink, J. and Movahed, M.-A. (2012), Computational validation of the EPR™ combustible gas control system, *Nuclear Engineering and Design* **249**, 118–124.
- Dinkelacker, F., Manickam, B. and Muppala, S. (2011), Modelling and simulation of lean premixed turbulent methane/hydrogen/air flames with an effective Lewis number approach, *Combustion and Flame* **158**(9), 1742–1749.
- Dowdy, D. R., Smith, D. B., Taylor, S. C. and Williams, A. (1991), The use of expanding spherical flames to determine burning velocities and stretch effects in hydrogen/air mixtures, *Symposium (International) on Combustion*, Vol. 23, Elsevier, pp. 325–332.
- Efimenko, A. A. and Dorofeev, S. B. (2001), CREBCOM code system for description of gaseous combustion, *Journal of Loss Prevention in the Process Industries* **14**(6), 575–581.
- Egorov, Y. and Menter, F. (2008), Development and application of SST–SAS turbulence model in the DESIDER Project, in S.-H. Peng and W. Haase (eds), *Advances in Hybrid RANS-LES Modelling*, Vol. 97, Berlin, Heidelberg, pp. 261–270. Series Title: Notes on Numerical Fluid Mechanics and Multidisciplinary Design.
- Ettner, F. A. (2013), *Effiziente numerische Simulation des Deflagrations-Deflagrations-Übergangs*, PhD Thesis, Technische Universität München.
- Ettner, F., Vollmer, K. G. and Sattelmayer, T. (2014), Numerical simulation of the deflagration-to-detonation transition in inhomogeneous mixtures, *Journal of Combustion* **2014**.

- Fernández-Galisteo, D., Kurdyumov, V. N. and Ronney, P. D. (2018), Analysis of premixed flame propagation between two closely-spaced parallel plates, *Combustion and Flame* **190**, 133–145.
- Fiorina, C., Clifford, I., Kelm, S. and Lorenzi, S. (2022), On the development of multi-physics tools for nuclear reactor analysis based on OpenFOAM: state of the art, lessons learned and perspectives, *Nuclear Engineering and Design* **387**, 111604.
- Fischer, M., Henning, A. and Surmann, R. (2014), Mitigation of severe accidents in AREVA's Gen 3+ nuclear power plants, *Nuclear Engineering and Design* **269**, 323–329.
- Frankel, M. and Sivashinsky, G. (1982), The effect of viscosity on hydrodynamic stability of a plane flame front, *Combustion Science and Technology* **29**(3-6), 207–224.
- Gostintsev, Y. A., Istratov, A. and Shulenin, Y. V. (1988), Self-similar propagation of a free turbulent flame in mixed gas mixtures, *Combustion, Explosion and Shock Waves* **24**(5), 563–569.
- Gottlieb, S., Ketcheson, D. I. and Shu, C.-W. (2011), *Strong stability preserving Runge-Kutta and multistep time discretizations*, World Scientific.
- Gouldin, F. C. (1987), An application of fractals to modeling premixed turbulent flames, *Combustion and Flame* **68**(3), 249–266.
- Goulier, J., Chaumeix, N., Halter, F., Meynet, N. and Bentaïb, A. (2017a), Experimental study of laminar and turbulent flame speed of a spherical flame in a fan-stirred closed vessel for hydrogen safety application, *Nuclear Engineering and Design* **312**, 214–227.
- Goulier, J., Comandini, A., Halter, F. and Chaumeix, N. (2017b), Experimental study on turbulent expanding flames of lean hydrogen/air mixtures, *Proceedings of the Combustion Institute* **36**(2), 2823–2832.
- Greenshields, C. J., Weller, H. G., Gasparini, L. and Reese, J. M. (2010), Implementation of semi-discrete, non-staggered central schemes in a colocated,

- polyhedral, finite volume framework, for high-speed viscous flows, *International Journal for Numerical Methods in Fluids* **63**(1), 1–21.
- Gu, G., Huang, J., Han, W. and Wang, C. (2021), Propagation of hydrogen-oxygen flames in Hele–Shaw cells, *International Journal of Hydrogen Energy* **46**(21), 12009–12015.
- Gupta, S. and Langer, G. (2019), Experimental research on hydrogen deflagration in multi-compartment geometry and application to nuclear reactor conditions, *Nuclear Engineering and Design* **343**, 103–137.
- Hasslberger, J. (2017), *Numerical simulation of deflagration-to-detonation transition on industry scale*, PhD thesis, Technical University of Munich (TUM).
- Hasslberger, J., Katzy, P., Boeck, L. R. and Sattelmayer, T. (2017a), Computational fluid dynamics simulation of deflagration-to-detonation transition in a full-scale Konvoi-type pressurized water reactor, *Journal of Nuclear Engineering and Radiation Science* **3**(4), 041014.
- Hasslberger, J., Kim, H. K., Kim, B. J., Ryu, I. C. and Sattelmayer, T. (2017b), Three-dimensional CFD analysis of hydrogen-air-steam explosions in APR1400 containment, *Nuclear Engineering and Design* **320**, 386–399.
- Hellsten, A. (1998), Some improvements in Menter’s k–omega SST turbulence model, *29th AIAA, Fluid Dynamics Conference*, American Institute of Aeronautics and Astronautics.
- Holler, T., Komen, E. M. J. and Kljenak, I. (2022), The role of CFD combustion modelling in hydrogen safety management – VIII: Use of Eddy Break-Up combustion models for simulation of large-scale hydrogen deflagration experiments, *Nuclear Engineering and Design* **388**, 111627.
- Hsu, W.-S., Chen, H.-P. and Lin, H. C. (2014), Hydrogen behavior in a large-dry pressurized water reactor containment building during a severe accident, *10th International Symposium on Hazards, Prevention and Mitigation of Industrial Explosions (ISHPMIE)*, Bergen, Norway.

- Jiang, Y.-H., Li, G.-X., Li, H.-M., Zhang, G.-P. and Lv, J.-C. (2020), Experimental study on the influence of hydrogen fraction on self-acceleration of H₂/CO/air laminar premixed flame, *International Journal of Hydrogen Energy* **45**(3), 2351–2359.
- Kampili, M., Vijaya Kumar, G., Kelm, S., Arul Prakash, K. and Allelein, H.-J. (2021), CFD simulations of stratified layer erosion in MiniPanda facility using the tailored CFD solver containmentFOAM, *International Journal of Heat and Mass Transfer* **178**, 121568.
- Kang, H.-S., Kim, J. and Hong, S.-W. (2022), Numerical analysis for hydrogen flame acceleration during a severe accident initiated by SB-LOCA in the APR1400 containment, *Hydrogen* **3**(1), 28–42.
- Kang, H. S., Kim, J., Hong, S. W. and Kim, S. B. (2020), Numerical analysis for hydrogen flame acceleration during a severe accident in the APR1400 containment using a multi-dimensional hydrogen analysis system, *Energies* **13**(22).
- Kapulla, R., Xionguo, L., Kelm, S., Doll, U., Paranjape, S. and Paladino, D. (2023), Importance, influence and limits of CFD radiation modeling for containment atmosphere simulations, *Nuclear Engineering and Design* **411**, 112408.
- Katzy, P. (2021), *Combustion model for the computation of flame propagation in lean hydrogen-air mixtures at low turbulence*, PhD thesis, Technical University of Munich (TUM).
- Katzy, P., Hasslberger, J., Boeck, L. R. and Sattelmayer, T. (2017b), The effect of intrinsic instabilities on effective flame speeds in under-resolved simulations of lean hydrogen-air flames, *Journal of Nuclear Engineering and Radiation Science* **3**(4).
- Katzy, P., Hasslberger, J. and Sattelmayer, T. (2017a), On the effect of pressure on intrinsic flame instabilities in lean hydrogen-air mixtures Part II: Experimental investigation based on OH-PLIF technique, *26th International Colloquium on the Dynamics of Explosions and Reactive Systems (ICDERS)*.

- Kelm, S., Baggemann, J., Reinecke, E. A., Verfondern, K. and Kamiya, S. (2021a), Simulation of hydrogen mixing and PAR operation during accidental release in an LH2 carrier engine room, *9th International Conference on Hydrogen Safety (ICHS)*, Health and Safety Executive, Edinburgh, Scotland.
- Kelm, S., Kampili, M., Liu, X., George, A., Schumacher, D., Druska, C., Struth, S., Kuhr, A., Ramacher, L., Allelein, H.-J., Prakash, K. A., Kumar, G. V., Cammiade, L. M. F. and Ji, R. (2021b), The tailored CFD package 'containment-FOAM' for analysis of containment atmosphere mixing, H₂/CO mitigation and aerosol transport, *Fluids* **6**(3), 100.
- Kelm, S., Klauck, M., Beck, S., Allelein, H. J., Preusser, G., Sangiorgi, M., Klein-Hessling, W., Bakalov, I., Bleyer, A., Bentaïb, A., Kljenak, I., Stempniewicz, M., Kostka, P., Morandi, S., Ada del Corno, B., Bratfisch, C., Risken, T., Denk, L., Parduba, Z., Paci, S., Manfredini, A., Silde, A., Juris, P., Jancovic, J., Lele, H. G. and Ganju, S. (2014), Generic Containment: Detailed comparison of containment simulations performed on plant scale, *Annals of Nuclear Energy* **74**, 165–172.
- Kelm, S., Lehmkuhl, J., Jahn, W. and Allelein, H. J. (2016), A comparative assessment of different experiments on buoyancy-driven mixing processes by means of CFD, *Annals of Nuclear Energy* **93**, 50–57.
- Kelm, S., Müller, H. and Allelein, H.-J. (2019), A review of the CFD modeling progress triggered by ISP-47 on containment thermal hydraulics, *Nuclear Science and Engineering* **193**(1-2), 63–80.
- Keppeler, R. and Pfitzner, M. (2015), Modelling of Landau–Darrieus and thermo-diffusive instability effects for CFD simulations of laminar and turbulent premixed combustion, *Combustion Theory and Modelling* **19**(1), 1–28.
- Ketcheson, D. I. (2010), Runge-Kutta methods with minimum storage implementations, *Journal of Computational Physics* **229**(5), 1763–1773.
- Kim, J. and Hong, S.-W. (2015), Analysis of hydrogen flame acceleration in APR1400 containment by coupling hydrogen distribution and combustion analysis codes, *Progress in Nuclear Energy* **78**, 101–109.

- Kim, W. K., Mogi, T. and Dobashi, R. (2013), Flame acceleration in unconfined hydrogen/air deflagrations using infrared photography, *Journal of Loss Prevention in the Process Industries* **26**(6), 1501–1505.
- Kim, W. K., Mogi, T., Kuwana, K. and Dobashi, R. (2015a), Prediction model for self-similar propagation and blast wave generation of premixed flames, *International Journal of Hydrogen Energy* **40**(34), 11087–11092.
- Kim, W. K., Mogi, T., Kuwana, K. and Dobashi, R. (2015b), Self-similar propagation of expanding spherical flames in large scale gas explosions, *Proceedings of the Combustion Institute* **35**(2), 2051–2058.
- Kim, W., Namba, T., Johzaki, T. and Endo, T. (2020), Self-similar propagation of spherically expanding flames in lean hydrogen-air mixtures, *International Journal of Hydrogen Energy* **45**(46), 25608–25614.
- Kim, W., Sato, Y., Johzaki, T., Endo, T., Shimokuri, D. and Miyoshi, A. (2018), Experimental study on self-acceleration in expanding spherical hydrogen-air flames, *International Journal of Hydrogen Energy* **43**(27), 12556–12564.
- Klauck, M., Reinecke, E.-A. and Allelein, H.-J. (2021), Effect of PAR deactivation by carbon monoxide in the late phase of a severe accident, *Annals of Nuclear Energy* **151**, 107887.
- Klein, M., Chakraborty, N. and Pfitzner, M. (2016), Analysis of the combined modelling of sub-grid transport and filtered flame propagation for premixed turbulent combustion, *Flow, Turbulence and Combustion* **96**(4), 921–938.
- Konnov, A. A. (2008), Remaining uncertainties in the kinetic mechanism of hydrogen combustion, *Combustion and Flame* **152**(4), 507–528.
- Kotchourko, A., Bentaïb, A., Fischer, K., Chaumeix, N., Yanez, J., Benz, S. and Kudryakov, S. (2012), ISP-49 on hydrogen combustion, *Technical report*, Nuclear Energy Agency Committee on the Safety of Nuclear Installations.
- Kudriakov, S., Dabbene, F., Studer, E., Beccantini, A., Magnaud, J. P., Paillere, H., Bentaïb, A., Bleyer, A., Malet, J. and Porcheron, E. (2008), The TONUS CFD code for hydrogen risk analysis: physical models, numerical schemes and validation matrix, *Nuclear Engineering and Design* **238**(3), 551–565.

- Lamoureux, N., Djebaili-Chaumeix, N. and Paillard, C. (2003), Laminar flame velocity determination for H₂-air-He-CO₂ mixtures using the spherical bomb method, *Experimental Thermal and Fluid Science* **27**(4), 385–393.
- Lapenna, P. E., Lamioni, R. and Creta, F. (2021), Subgrid modeling of intrinsic instabilities in premixed flame propagation, *Proceedings of the Combustion Institute* **38**(2), 2001–2011.
- Lapenna, P. E., Lamioni, R., Troiani, G. and Creta, F. (2019), Large scale effects in weakly turbulent premixed flames, *Proceedings of the Combustion Institute* **37**(2), 1945–1952.
- Lee, J. H. S. (2008), *The Detonation Phenomenon*, Cambridge University Press, Cambridge.
- Li, X., You, X., Wu, F. and Law, C. K. (2015), Uncertainty analysis of the kinetic model prediction for high-pressure H₂/CO combustion, *Proceedings of the Combustion Institute* **35**(1), 617–624.
- Liberman, M. A. (2021), *Combustion physics: flames, detonations, explosions, astrophysical combustion and inertial confinement fusion*, Springer Cham.
- Liberman, M. A., Ivanov, M. F., Peil, O. E., Valiev, D. M. and Eriksson, L.-E. (2004), Self-acceleration and fractal structure of outward freely propagating flames, *Physics of fluids* **16**(7), 2476–2482.
- Lind, C. (1974), Explosion hazards associated with spills of large quantities of hazardous materials: Phase I, *Technical report*, Naval Weapons Center China Lake CA.
- Liou, M.-S. (2006), A sequel to AUSM, Part II: AUSM+-up for all speeds, *Journal of Computational Physics* **214**(1), 137–170.
- Liou, M.-S. (2010), The Evolution of AUSM Schemes, *Defence Science Journal* **60**(6), 606–613.
- Lipatnikov, A. (2012), *Fundamentals of premixed turbulent combustion*, CRC Press.

- Lipatnikov, A. and Chomiak, J. (2002), Turbulent flame speed and thickness: phenomenology, evaluation, and application in multi-dimensional simulations, *Progress in energy and combustion science* **28**(1), 1–74.
- Lipatnikov, A. and Chomiak, J. (2005), Molecular transport effects on turbulent flame propagation and structure, *Progress in Energy and Combustion Science* **31**(1), 1–73.
- Lipatnikov, A. N., Sabelnikov, V. A., Nishiki, S. and Hasegawa, T. (2018), Letter: Does flame-generated vorticity increase turbulent burning velocity?, *Physics of Fluids* **30**(8), 081702.
- Lipatnikov, A. N., Sabelnikov, V. A., Nishiki, S. and Hasegawa, T. (2019), A direct numerical simulation study of the influence of flame-generated vorticity on reaction-zone-surface area in weakly turbulent premixed combustion, *Physics of Fluids* **31**(5), 055101.
- Liu, F., Bao, X., Gu, J. and Chen, R. (2012), Onset of cellular instabilities in spherically propagating hydrogen-air premixed laminar flames, *International Journal of Hydrogen Energy* **37**(15), 11458–11465.
- Liu, X., Kelm, S., Kampili, M., Kumar, G. V. and Allelein, H.-J. (2022), Monte Carlo method with SNBCK non-gray gas model for thermal radiation in containment flows, *Nuclear Engineering and Design* **390**, 111689.
- Liu, Z., Unni, V. R., Chaudhuri, S., Sui, R., Law, C. K. and Saha, A. (2021), Self-turbulization in cellularly unstable laminar flames, *Journal of Fluid Mechanics* **917**, A53.
- Mandelbrot, B. B. (1983), *The Fractal Geometry of Nature*, 3 edn, W. H. Freeman and Comp., New York.
- Manninen, M., Lindholm, I., Huhtanen, R. and Sjövall, H. (2000), Hydrogen in BWR reactor building, *8th International Conference on Nuclear Engineering, ICONE 8*, American Society of Mechanical Engineers (ASME), pp. 273–284.
- Manninen, M., Silde, A., Lindholm, I., Huhtanen, R. and Sjövall, H. (2002), Simulation of hydrogen deflagration and detonation in a BWR reactor building, *Nuclear Engineering and Design* **211**(1), 27–50.

- Marshall, B. W. (1986), Hydrogen-air-steam flammability limits and combustion characteristics in the FITS (Fully Instrumented Test Site) vessel, *Technical Report No. NUREG/CR-3468; SAND-84-0383*, Sandia National Labs., Albuquerque, NM (USA); Nuclear Regulatory Commission, Washington, DC (USA). Div. of Reactor Systems Safety.
- Matalon, M. (2018), The Darrieus–Landau instability of premixed flames, *Fluid Dynamics Research* **50**(5).
- Matalon, M. and Matkowsky, B. J. (1982), Flames as gasdynamic discontinuities, *Journal of Fluid Mechanics* **124**, 239–259.
- Menter, F. (1994), Two-equation eddy-viscosity turbulence models for engineering applications, *AIAA journal* **32**(8), 1598–1605.
- Menter, F. and Egorov, Y. (2005), A scale-adaptive simulation model using two-equation models, *43rd AIAA Aerospace Sciences Meeting and Exhibit*, Reno, Nevada.
- Menter, F. and Esch, T. (2001), Elements of industrial heat transfer predictions, *16th Brazilian Congress of Mechanical Engineering (COBEM)* **109**, 650.
- Menter, F., Kuntz, M. and Langtry, R. (2003), Ten years of industrial experience with the SST turbulence model, *Heat and Mass Transfer* **4**(1), 625–632.
- Menter, F. R. and Egorov, Y. (2010), The scale-adaptive simulation method for unsteady turbulent flow predictions. Part I: Theory and model description, *Flow Turbulence Combustion* **85**(1), 113–138.
- Middha, P. and Hansen, O. R. (2008), Predicting deflagration-to-detonation transition in hydrogen explosions, *Process Safety Progress* **27**(3), 192–204.
- Molkov, V., Makarov, D. and Grigorash, A. (2004), Cellular structure of explosion flames: Modeling and large-eddy simulation, *Combustion Science and Technology* **176**(5-6), 851–865.
- Molkov, V., Makarov, D. and Puttock, J. (2006a), The nature and large eddy simulation of coherent deflagrations in a vented enclosure-atmosphere system, *Journal of Loss Prevention in the Process Industries* **19**(2), 121–129.

- Molkov, V., Makarov, D. and Schneider, H. (2006b), LES modelling of an unconfined large-scale hydrogen-air deflagration, *J. Phys. D: Appl. Phys.* **39**(20), 4366–4376.
- Molkov, V., Makarov, D. and Schneider, H. (2007), Hydrogen-air deflagrations in open atmosphere: Large eddy simulation analysis of experimental data, *International Journal of Hydrogen Energy* **32**(13), 2198–2205.
- Molkov, V., Verbecke, F. and Makarov, D. (2008), LES of hydrogen-air deflagrations in a 78.5-m tunnel, *Combustion Science and Technology* **180**(5), 796–808.
- Mukaiyama, K., Shibayama, S. and Kuwana, K. (2013), Fractal structures of hydrodynamically unstable and diffusive-thermally unstable flames, *Combustion and Flame* **160**(11), 2471–2475.
- Muppala, S. R., Aluri, N. K., Dinkelacker, F. and Leipertz, A. (2005), Development of an algebraic reaction rate closure for the numerical calculation of turbulent premixed methane, ethylene, and propane/air flames for pressures up to 1.0 MPa, *Combustion and Flame* **140**(4), 257–266.
- Nwagwe, I. K., Weller, H. G., Tabor, G. R., Gosman, A. D., Lawes, M., Sheppard, C. G. W. and Wooley, R. (2000), Measurements and large eddy simulations of turbulent premixed flame kernel growth, *Proceedings of the Combustion Institute* **28**(1), 59–65.
- Ozel-Erol, G., Klein, M. and Chakraborty, N. (2021), Lewis number effects on flame speed statistics in spherical turbulent premixed flames, *Flow, Turbulence and Combustion* **106**(4), 1043–1063.
- Poinsot, T. and Veynante, D. (2005), *Theoretical and numerical combustion*, RT Edwards, Inc.
- Poruba, C. (2003), *Turbulente Flammenausbreitung in Wasserstoff-Luft-Gemischen*, PhD thesis, Technical University of Munich (TUM).
- Redlinger, R. (2008), DET3D—A CFD tool for simulating hydrogen combustion in nuclear reactor safety, *Nuclear Engineering and Design* **238**(3), 610–617.

- Reinecke, E.-A., Fontanet, J., Herranz, L. E., Liang, Z., Maas, L., Mazurok, O., Park, J.-S., Visser, D. C., Hupp, M. and Gupta, S. (2022), PAR model development exercise in the framework of SAMHYCO-NET, *Nuclear Engineering and Design* **399**, 112035.
- Reinke, N., Arndt, S., Bakalov, I., Band, S., Beck, S., Nowack, H., Iliev, D., Spengler, C., Klein-Hessling, W. and Sonnenkalb, M. (2019), Validation and application of the AC2 code COCOSYS, *Kerntechnik* **84**(5), 414–424.
- Sathiah, P., Holler, T., Kljenak, I. and Komen, E. (2016a), The role of CFD combustion modeling in hydrogen safety management – V: Validation for slow deflagrations in homogeneous hydrogen-air experiments, *Nuclear Engineering and Design* **310**, 520–531.
- Sathiah, P., Komen, E. and Roekaerts, D. (2012a), The role of CFD combustion modeling in hydrogen safety management–Part I: Validation based on small scale experiments, *Nuclear Engineering and Design* **248**, 93–107.
- Sathiah, P., Komen, E. and Roekaerts, D. (2015), The role of CFD combustion modeling in hydrogen safety management – III: Validation based on homogeneous hydrogen-air-diluent experiments, *Nuclear Engineering and Design* **289**, 296–310.
- Sathiah, P., Komen, E. and Roekaerts, D. (2016b), The role of CFD combustion modeling in hydrogen safety management – IV: Validation based on non-homogeneous hydrogen-air experiments, *Nuclear Engineering and Design* **310**, 507–519.
- Sathiah, P., van Haren, S., Komen, E. and Roekaerts, D. (2012b), The role of CFD combustion modeling in hydrogen safety management–II: Validation based on homogeneous hydrogen-air experiments, *Nuclear Engineering and Design* **252**, 289–302.
- Saurel, R. and Lemetayer, O. (2001), A multiphase model for compressible flows with interfaces, shocks, detonation waves and cavitation, *Journal of Fluid Mechanics* **431**, 239–271. Publisher: Cambridge University Press.
- Schneider, H. and Pfortner, H. (1983), Prozessgasfreisetzung – Explosion in der Gasfabrik und Auswirkungen von Druckwellen auf das

- Containment, *Technical report*, Fraunhofer-ICT Internal Report: PNP-Sicherheitssofortprogramm,.
- Shu, C.-W. and Osher, S. (1988), Efficient implementation of essentially non-oscillatory shock-capturing schemes, *Journal of computational physics* **77**(2), 439–471.
- Sivashinsky, G. I. (1977), Nonlinear analysis of hydrodynamic instability in laminar flames—I. Derivation of basic equations, *Acta astronautica* **4**(11), 1177–1206.
- Sod, G. A. (1978), A survey of several finite difference methods for systems of nonlinear hyperbolic conservation laws, *Journal of Computational Physics* **27**(1), 1–31.
- Sonnenkalb, M., Band, S., Nowack, H. and Schwarz, S. (2015), Re-evaluation of PAR concept in German PWR with revised PAR model, *NURETH 16*, Chicago, USA.
- Studer, E., Beccantini, A., Kudriakov, S. and Velikorodny, A. (2014), Hydrogen combustion modelling in large-scale geometries, *21st International Conference on Nuclear Engineering (ICONE)*, American Society of Mechanical Engineers Digital Collection.
- Sun, Z.-Y., Liu, F.-S., Bao, X.-C. and Liu, X.-H. (2012), Research on cellular instabilities in outwardly propagating spherical hydrogen-air flames, *International Journal of Hydrogen Energy* **37**(9), 7889–7899.
- Sutherland, W. (1893), LII. The viscosity of gases and molecular force, *The London, Edinburgh, and Dublin Philosophical Magazine and Journal of Science* **36**(223), 507–531. Publisher: Taylor & Francis.
- Tang, K., Beccantini, A. and Corre, C. (2014a), Combining discrete equations method and upwind downwind-controlled splitting for non-reacting and reacting two-fluid computations: One dimensional case, *Computers & Fluids* **93**, 74–90.

- Tang, K., Beccantini, A. and Corre, C. (2014b), Combining discrete equations method and upwind downwind-controlled splitting for non-reacting and reacting two-fluid computations: Two dimensional case, *Computers & Fluids* **103**, 132–155.
- Taylor, S. C. (1991), *Burning velocity and the influence of flame stretch*, PhD thesis, University of Leeds.
- Toro, E. F. (2009), *Riemann Solvers and Numerical Methods for Fluid Dynamics: A Practical Introduction*, Springer Science & Business Media.
- Travis, J., Spore, J., Royl, P., Lam, K., Wilson, T., Müller, C., Necker, G., Nichols, B. and Redlinger, R. (1998), GASFLOW: A computational fluid dynamics code for gases, aerosols, and combustion, *Vol. I, Theory and Computational Model, Reports FZKA-5994, LA-13357-M*.
- van Leer, B. (1979), Towards the ultimate conservative difference scheme. V. A second-order sequel to Godunov's method, *Journal of Computational Physics* **32**(1), 101–136.
- Veiga-López, F., Kuznetsov, M., Yanez, J., Grüne, J. and Sánchez-Sanz, M. (2019), Flame propagation near the limiting conditions in a thin layer geometry, *8th International Conference on Hydrogen Safety (ICHS)*.
- Velikorodny, A., Studer, E., Kudriakov, S. and Beccantini, A. (2015), Combustion modeling in large scale volumes using EUROPLEXUS code, *Journal of Loss Prevention in the Process Industries* **35**, 104–116.
- Vijaya Kumar, G., Cammiade, L. M. F., Kelm, S., Arul Prakash, K., Gross, E. M., Allelein, H.-J., Kneer, R. and Rohlf, W. (2021), Implementation of a CFD model for wall condensation in the presence of non-condensable gas mixtures, *Applied Thermal Engineering* **187**, 116546.
- Weiss, J. M. and Smith, W. A. (1995), Preconditioning applied to variable and constant density flows, *AIAA Journal* **33**(11), 2050–2057.
- Weller, H. (1993), The development of a new flame area combustion model using conditional averaging, *Thermo-fluids section report TF 9307*.

- Weller, H. G., Tabor, G., Jasak, H. and Fureby, C. (1998), A tensorial approach to computational continuum mechanics using object-oriented techniques, *Computers in physics* **12**(6), 620–631.
- Weller, H., Tabor, G., Gosman, A. and Fureby, C. (1998b), Application of a flame-wrinkling LES combustion model to a turbulent mixing layer, *Symposium (International) on Combustion* **27**(1), 899–907.
- Wenig, P., Ji, R., Kelm, S. and Klein, M. (2021), Towards uncertainty quantification of LES and URANS for the buoyancy-driven mixing process between two miscible fluids–differentially heated cavity of aspect ratio 4, *Fluids* **6**, 161.
- Wieland, C., Scharf, F., Schildberg, H. P., Hoferichter, V., Eble, J., Hirsch, C. and Sattelmayer, T. (2021), Efficient simulation of flame acceleration and deflagration-to-detonation transition in smooth pipes, *Journal of Loss Prevention in the Process Industries* **71**, 104504.
- Wilkening, H. and Huld, T. (1999), An adaptive 3-D CFD solver for modeling explosions on large industrial environmental scales, *Combustion Science and Technology* **149**(1-6), 361–387.
- Xiao, J., Breitung, W., Kuznetsov, M., Zhang, H., Travis, J. R., Redlinger, R. and Jordan, T. (2017a), GASFLOW-MPI: A new 3-D parallel all-speed CFD code for turbulent dispersion and combustion simulations: Part I: Models, verification and validation, *International Journal of Hydrogen Energy* **42**(12), 8346–8368.
- Xiao, J., Breitung, W., Kuznetsov, M., Zhang, H., Travis, J. R., Redlinger, R. and Jordan, T. (2017b), GASFLOW-MPI: A new 3-D parallel all-speed CFD code for turbulent dispersion and combustion simulations: Part II: First analysis of the hydrogen explosion in Fukushima Daiichi Unit 1, *International Journal of Hydrogen Energy* **42**(12), 8369–8381.
- Yabing, L., Xianghui, L., Peng, C. and Deyang, X. (2022), A conservative approach for the fast deflagration analysis in the containment with GASFLOW-MPI, *Frontiers in Energy Research* **10**.

- Yasari, E. (2013), *Extension of OpenFOAM library for RANS simulation of premixed turbulent combustion*, PhD thesis, Chalmers University of Technology.
- Yu, R., Bai, X.-S. and Bychkov, V. (2015), Fractal flame structure due to the hydrodynamic Darrieus–Landau instability, *Physical Review E* **92**(6), 063028.
- Zivkovic, D. and Sattelmayer, T. (2021), Towards efficient and time-accurate simulations of early stages of industrial scale explosions, *9th International Conference on Hydrogen Safety (ICHS)*, Health and Safety Executive, Edinburgh, Scotland.
- Zivkovic, D. and Sattelmayer, T. (2023), Fractal based, scale-adaptive closure model for Darrieus–Landau instability effects on large-scale hydrogen-air flames, *Combustion Science and Technology* **195**(7), 1573–1598.

A Publications

Parts of the present thesis have been published by the author in journals or as conference proceedings in the past. These publications are registered according to the valid doctoral regulations and listed below. Text sections and figures are reproduced with the permission of corresponding publishers.

Zivkovic, D., Sattelmayer, T., 2023. Fractal based, scale-adaptive closure model for Darrieus–Landau instability effects on large-scale hydrogen-air flames. *Combustion Science and Technology*, 195:7, 1573-1598, DOI: 10.1080/00102202.2023.2182201

Zivkovic, D., Sattelmayer, T., 2022. Fractal-based RANS modeling of Darrieus–Landau and thermal-diffusive instability effects on lean hydrogen flames. *Proceedings of the 28th International Colloquium on the Dynamics of Explosions and Reactive Systems (ICDERS 2022)*

Zivkovic, D., Sattelmayer, T., 2021. Towards efficient and time-accurate simulations of early stages of industrial scale explosions. *Proceedings of the 9th International Conference on Hydrogen Safety (ICHHS 2021)*